

IMPROVING THE DROP CONSISTENCY
OF AN INKJET PRINthead
BY ITERATIVE LEARNING CONTROL

P.M. NAGELMAEKER

DCT 2006.108

Supervisors: Prof. ir. O.H. Bosgra
Ir. M.B. Groot Wassink
Ir. R.J.A. van Loon

Eindhoven University of Technology
Delft University of Technology
Océ-Technologies B.V.

EINDHOVEN UNIVERSITY OF TECHNOLOGY
DEPARTMENT OF MECHANICAL ENGINEERING
CONTROL SYSTEMS TECHNOLOGY GROUP

Venlo, September 2006



Abstract

The drop consistency of inkjet printheads is limited by residual vibrations. Drop consistency can be improved by damping the residual vibrations first prior to jetting a next droplet. Iterative Learning Control (ILC) can be applied to design actuation signals that leave the droplet formation undisturbed while minimizing the residual vibrations. For this purpose, a model based on the piezo sensor is identified and an ILC controller is designed in the lifted setting using separate actuation and observation windows. It is illustrated by means of experimental results that ILC can effectively damp the residual vibrations and improve the drop consistency.

Preface

This report is written for the Master Thesis assignment 'Improving the drop consistency of an inkjet printhead by Iterative Learning Control' of the Eindhoven University of Technology, department of Mechanical Engineering, Control Systems Technology Group. The research is conducted at Océ-Technologies B.V. Venlo.

First of all, I would like to thank my supervisors Rob van Loon, professor Okko Bosgra and, especially, Matthijs Groot Wassink for their support and advise during my research. Furthermore, I would like to thank my colleagues at Océ for their help and the useful discussions. Special thanks goes to Jan Simons, Wim de Zeeuw and Rogier Jeurissen for their support.

'De schrijver werd door Océ-Technologies B.V. in staat gesteld onderzoek te verrichten, dat mede aan dit rapport ten grondslag ligt. Océ-Technologies B.V. aanvaardt geen verantwoordelijkheid voor de juistheid van de in dit rapport vermelde gegevens, beschouwingen en conclusies, die geheel voor rekening van de schrijver komen'.

Summary

Inkjet is an important technology in wide format (color) printing. In this study, an inkjet printhead is considered that comprises two arrays of channels with a high nozzle per inch ratio. The printhead works according to the drop on demand (DOD) principle. Each channel is equipped with a separate piezo actuator. When a droplet of ink is desired, a voltage pulse is sent to one of the piezo actuators causing acoustic pressure waves to arise in the ink channel. The acoustics waves result in an acceleration of the ink in the nozzle and subsequently a single droplet is emitted from the nozzle.

The drop consistency of an inkjet printhead is severely limited by residual vibrations. After the ejection of a droplet, the ink channel is not immediately in rest and one should wait until the residual vibrations are damped out before the channel is actuated again. Otherwise, consistency in droplet properties cannot be guaranteed.

A switch to active control of an inkjet printhead can improve drop consistency. This boils down to damping the residual vibrations before a new droplet is ejected. Given the highly repetitive character of the jetting process, Iterative Learning Control (ILC) seems a proper choice.

The implementation of ILC requires a proper sensor functionality and a model of the system dynamics. It is chosen to use the piezo as sensor which gives a measure for the pressure inside the ink channel. Two theoretical and one experimental model are studied. For the ILC synthesis, it is chosen to use the experimental model. The obtained model describes the ink channel dynamics which are crucial for the jetting process. Though the acoustic resonance frequencies are predicted accurately, it was demonstrated that the experimental model is only valid for non-jetting situations where the system behaves linearly. However, the ejection of a small volume of ink (the droplet) introduces nonlinear behavior. Consequently, inaccuracies are obtained for jetting situations. Nevertheless, it is demonstrated that ILC is robust against the occurring nonlinearities.

Based on physical insights, the defined control goal is translated to the design of a suited reference trajectory. ILC in the lifted setting is implemented on the printhead using separate actuation and observation windows. It is demonstrated on experimental level that with using ILC for optimally tracking the designed reference trajectory, actuation signals are designed that successfully damp the residual vibrations without disturbing the droplet formation process.

By means of drop property measurements the improvement in drop consistency is verified. It is demonstrated that with the designed actuation signals the drop-speed and -volume variations that occur during the operation of an inkjet printhead have been reduced by 66 % and 48 % respectively.

Nomenclature

General

L_{act}	length of piezo actuator	[m]
V	actuation voltage	[V]
λ	wavelength	[m]

Signals and Systems

e	tracking error
H_{P2P}	dynamics from the piezo actuator to the piezo sensor
H_{P2PI}	dynamics from the piezo actuator to the piezo sensor integrated in time
H_{P2MV}	dynamics from the piezo actuator to the meniscus velocity
J	impulse response matrix or Toeplitz matrix
k	iteration number
L	learning matrix
N	numbers of samples in a trial
u	system input
y	system output
y_r	reference trajectory
z^{-1}	trial delay operator
Δu	update system input

Abbreviations

ASIC	Application Specific Integrated Circuit
CCD	Charge-Couple Device camera
DC	Direct Current
DOD	Drop-On-Demand
FEM	Finite Element Method
IAE	Integrated Absolute Error
FFT	Fast Fourier Transformation
ILC	Iterative Learning Control
MV-ILC	Meniscus Velocity based Iterative Learning Control
MIMO	Multi-Input-Multi-Output

PID	Proportional Integral and Differentiation feedback controller
P-ILC	Piezo based Iterative Learning Control
SISO	Single-Input-Single-Output

Contents

1	Introduction	1
1.1	Introduction	1
1.2	Problem Definition and Objective	3
1.3	Outline	3
2	Experimental Setup	5
2.1	Introduction	5
2.2	Configuration used for Identification	6
2.3	Configuration used for Control	8
3	Modeling of an Inkjet Printhead	11
3.1	Introduction	11
3.2	The Narrow-Gap Model	12
3.2.1	Theory	12
3.2.2	Analyses	13
3.3	Wave Model	19
3.3.1	Theory	19
3.3.2	Analyses	20
3.4	Experimental Model	21
3.4.1	Frequency Response Measurements	22
3.4.2	Model Fitting	24
3.4.3	Model Validation	24
3.5	Discussion	27
3.6	Conclusions	30

4	Control of an Inkjet Printhead	33
4.1	Control Goal	33
4.2	Operational issues revisited	34
4.2.1	Residual Vibrations	34
4.2.2	Air Entrapment	35
4.2.3	Nozzle Refill	36
4.2.4	Nozzle-plate Wetting	37
4.3	ILC working principle	38
4.4	Reference Trajectory Design Criteria	38
4.5	Piezo based ILC versus Meniscus Velocity based ILC	41
4.6	Simulations	43
4.6.1	P-ILC versus MV-ILC using the Narrow-Gap model	43
4.6.2	P-ILC versus MV-ILC using the Wave model.	46
4.6.3	Discussion	47
4.7	Conclusions	47
5	Implementation of Iterative Learning Control	49
5.1	Practical Considerations	49
5.2	Controller Synthesis	50
5.3	Piezo Based ILC	50
5.4	Piezo Based ILC using Time Weights	53
5.5	Performance Evaluation	58
5.6	Conclusions	62
6	Conclusions and Recommendations	65
6.1	Conclusions	65
6.2	Recommendations	66
A	Narrow Gap Model	69
B	Dijksman Model	75
C	Wave Model	81
C.1	Channel Acoustics	81
C.2	Fluid Dynamics in the Nozzle	83
D	Destructive Interference	87

<i>CONTENTS</i>	xiii
E Simplification and Robustness of the ILC Actuation	91
E.1 Constraint ILC	91
E.2 Robustness for Production Tolerances	91
Bibliography	93

Chapter 1

Introduction

1.1 Introduction

Océ is specialized in the market of printing applications for professional users. One of these applications is that of wide format (color) printing, for which inkjet technology is applied. Inkjet can deposit droplets of ink in patterns on a substrate. With inkjet technology, main targets are a high resolution, a constant print quality and a high print speed. These demands can directly be translated into small droplets with constant properties and high jet frequencies of the printhead.



Figure 1.1: *Océ wide format color printer using inkjet technology.*

During the research presented here, the printhead under investigation is a piezoelectric inkjet printhead that comprises two arrays of ink channels with a high nozzle per inch ratio. Each channel is equipped with a piezo actuator and the printhead works according to the drop on demand (DOD) principle. When a droplet of ink is desired, a voltage pulse is sent to one of the piezo actuators causing acoustic pressure waves to arise in the ink channel. The acoustic waves result in an acceleration of the ink in the nozzle and subsequently a single droplet is emitted from the nozzle.

During operation, the functioning of the printhead is hampered by several operational issues. Firstly, print quality suffers from residual vibrations. After ejection of a droplet, the ink inside the channel is not immediately in rest and one should wait until the acoustic pressure waves are damped out before a new actuation pulse can be applied. Otherwise, consistency in droplet properties cannot be guaranteed. Another phenomenon which is encountered during jetting is interaction between different channels, called cross-talk. If a channel is actuated, neighboring channels are influenced by cross-talk. This results in deviations of the droplet properties if neighboring channels are actuated simultaneously. Thirdly, jet instability forms a significant problem in inkjet in general. Jet instability is the phenomenon where a nozzle stops jetting and causes severe defects in a print which are unacceptable. Nozzle failure occurs mostly when an air bubble is entrapped into the nozzle due to extreme movements of the meniscus (air-ink interface) inside the nozzle. Another negative result of extreme meniscus movements is that it can cause wetting of the nozzle plate. With wetting, the outside of the printhead, the nozzle plate, is covered by a thin layer of ink which originates from the actuated channels. The presence of an ink layer in front of the nozzle has a negative influence on the drop consistency and is often linked with nozzle failure.

In the current situation the piezo actuators are provided with pulses, whose shape has been the result of a design based on physical insight, such that the requested drop on demand (DOD) results. However, the current actuation pulse leaves the mentioned problems unsolved to some extent. A switch from passive to active control might cancel out the phenomena sketched above. With active control, no longer use is made of the standard actuation pulse. Given the highly repetitive character of the jetting process, feedforward control seems a proper choice and will generally yield much improved performance compared to pure feedback control. One way to achieve high-quality feedforward control is through the application of Iterative Learning Control (ILC), an iterative update scheme which improves the quality of the feedforward signal from trial to trial. Literature on ILC is already quite extensive [Moo99], [Lon00], [Bos03]. Besides, ILC is already widely applied on systems that perform repetitive tasks, e.g. see [Dij03], [RDS04].

The application of ILC in the field of inkjet technology is not novel. Earlier research performed at Océ showed that ILC can be used as active control strategy for an inkjet printhead, see [WBBK05], [WZBK06]. Both researches concern the implementation of ILC on an inkjet printhead, each using a different sensor functionality. By using the piezo unit also as sensor, the pressure in the channel can be measured. In [WBBK05] this sensor signal is used for the implementation of ILC in order to control the pressure inside the channel. Experimental results showed that with ILC, actuation signals are designed that bring the channel to a rest quickly after droplet ejection, resulting in a considerable improvement of the drop consistency. In [WZBK06] the velocity of the meniscus is obtained with laser-Doppler measurements. These measurements give details on ink flow inside and in front of the nozzle. Based on this sensor signal, the movements of the meniscus can be controlled with the implementation of ILC. Experimental results showed that with meniscus based ILC, actuation signals are designed that bring the meniscus to a rest quickly after droplet ejection. With meniscus based ILC a comparable improvement of the drop consistency is obtained as with piezo based ILC. ILC was also used in order to minimize the cross-talk of an inkjet printhead.

In [WBK06] an approach based on MIMO ILC is presented which minimize the interaction between neighboring channels.

1.2 Problem Definition and Objective

As already introduced in the previous section, the performance of an inkjet printhead is limited by residual vibrations, cross-talk and jet instability. Previous research demonstrated that both residual vibrations and cross-talk can be minimized by applying ILC on an inkjet printhead. However, a further refinement of the implementation of ILC on an actual inkjet printhead is required. It is expected that with improving the reference trajectory design, the attainable performance might be improved.

During this research, not all the mentioned operational issues will be investigated. It is chosen to focus on the residual vibrations which negatively affect the drop consistency. Besides, it is investigated how the design of a suited reference trajectory can help to improve jet stability. However, during this research, jet stability is not investigated on the actual printhead. Based on these considerations, the following problem statement is defined:

Improve the drop consistency of an inkjet printhead by the implementation of ILC using reference trajectory design based on physical insights.

The problem statement can be translated to the following objectives:

1. Explore the working principle of a piezoelectric printhead (see [Nag06]).
2. Investigate the operational issues by means of two theoretical models: the Narrow-Gap model and the wave model.
3. Identify and model the printhead dynamics by using the piezo sensor.
4. Design a suited reference trajectory based on physical insights.
5. Implement ILC based on the piezo sensor on a single channel in order to improve the performance of the printhead.

1.3 Outline

This thesis is organized as follows. First, the experimental setup and the different sensor functionalities are discussed in Chapter 2. Furthermore, the configuration setting used for system identification and the setting used for ILC experiments will be addressed. For modeling of the inkjet printhead both theoretical and experimental modeling is utilized. In Chapter 3, two existing theoretical printhead models will be discussed. Moreover, experimental modeling is performed. The results and the validation of the obtained experimental model will be addressed. Finally, the three obtained models will be compared to each other and their

usability for our control purposes will be assessed. Chapter 4 concerns the design of a suited reference trajectory. First, the ILC control goal will be further elaborated, i.e. improving the drop consistency. Next, the physical insights needed for the reference trajectory design are addressed. It is explained how several operational issues which are encountered during jetting are related to drop consistency and jet stability. Based on these insights, it is explained how the design of a suitable reference trajectory can overcome these issues. Next, ILC simulations are addressed. With the simulations two different sensor functionalities are investigated in order to damp the residual vibrations. Finally, at the end of Chapter 4 will be explained that it is chosen to use the piezo sensor for the implementation of ILC on the actual printhead. The results hereof are discussed in Chapter 5. The experimental model is used to implement ILC on the experimental setup. ILC is applied with and without using time weights and for both approaches the improvement of the drop consistency is evaluated. Finally, Chapter 6 handles the conclusions and the recommendations for future research.

Chapter 2

Experimental Setup

2.1 Introduction

In this chapter the experimental setup is briefly presented. This setup was used for the research presented in this report. With the setup it is possible to apply arbitrary input signals to the piezo actuator and monitor the droplet formation process and the functioning of the printhead itself. A schematic overview of the setup is given in Fig. 2.1.

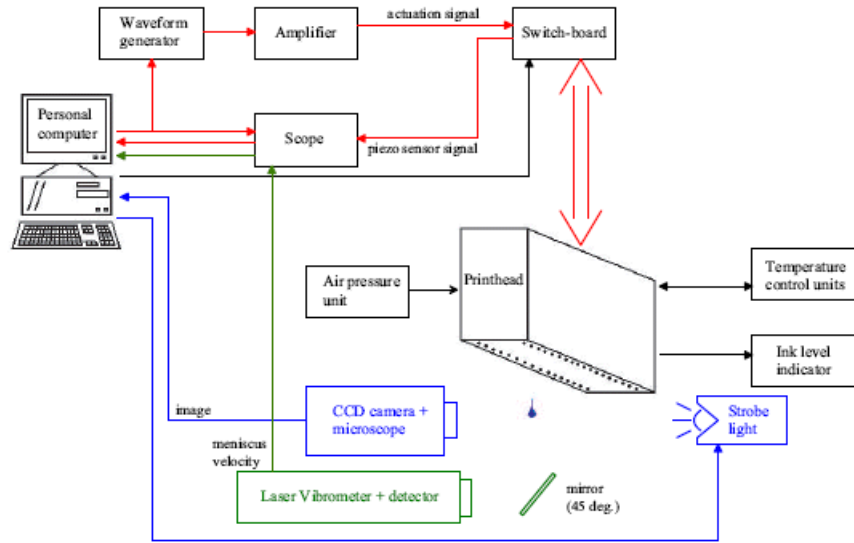


Figure 2.1: *Schematic overview of the experimental setup*

The printhead under investigation uses toner ink, which requires heating of the printhead. With a PID controller, the printhead temperature is kept at a certain constant reference value. With use of an air-pressure unit, the pressure inside the reservoir is kept under ambient pressure to avoid the ink flowing out through the nozzle under influence of gravity. With **Labview**, the desired actuation signal can be generated and is sent to a waveform generator. The signal is amplified and finally sent to the piezo actuator. Measurements can be performed

by a CCD camera and a laser-vibro meter. Moreover, the piezo unit can be used both as actuator and sensor. These sensor functionalities will be shortly discussed next:

CCD Camera

The ejected droplets can be observed by Charge-Couple Device (CCD) camera equipped with a microscope. Based on the images obtained with the camera it is possible to estimate the speed and the volume of the ejected droplets.

Laser-vibro meter

By means of laser-Doppler interferometry, the velocity of the ink surface inside the nozzle of an inkjet printhead can be measured. The output of the laser-vibro meter is in fact the velocity of the meniscus (ink-air interface) in the center of the nozzle. A major drawback of this measurement technique is that it cannot be applied in the jetting situation since only low ink velocities can be measured. More information can be found in [Zol05], where is explained how the laser-vibro meter is deployed for the implementation of the control strategy ILC on an inkjet printhead.

Piezo sensor

As explained in [Pat], the piezo unit is currently used as actuator and sensor. Physically, it senses the force that results from the pressure distribution in the channel acting on the piezo's surface that borders the channel. This force creates a charge on the piezo unit. Since only changes in charge are measured, in fact the time derivative of the instantaneous present force is sensed. Furthermore, since the resulting voltage drop of this current over a resistance is measured, we have that a voltage is the resulting sensor signal. At the setup, the sensed piezo signal is filtered for high frequent noise and for undesired high frequent piezo behavior. For tracing the piezo signal, an oscilloscope is available, which samples the data at 10 MHz. Finally, the sampled data can be downloaded on the computer.

For the implementation of ILC on the inkjet printhead, it is chosen to use the piezo unit as sensor. In Chapter 4 will be explained why this sensor functionality is chosen. Based on this sensor functionality, two different configuration settings were used during the research. The configuration setting used for identification experiments is explained in Section 2.2. The setting used for ILC experiments is discussed in Section 2.3.

2.2 Configuration used for Identification

For the implementation of ILC an experimental model of the system dynamics is used. The obtained model is fitted to frequency response data acquired with sine-sweep measurements. The configuration described in this section was used to identify the printhead dynamics between piezo actuation signal and piezo sensor signal and is depicted in Fig. 2.2.

A spectrum analyzer was used to perform frequency response measurements. The output of the analyzer is a logarithmic sine sweep with a user-defined frequency range and amplitude (max 1 Volt). This output signal is amplified and sent to the piezo actuator of the printhead.

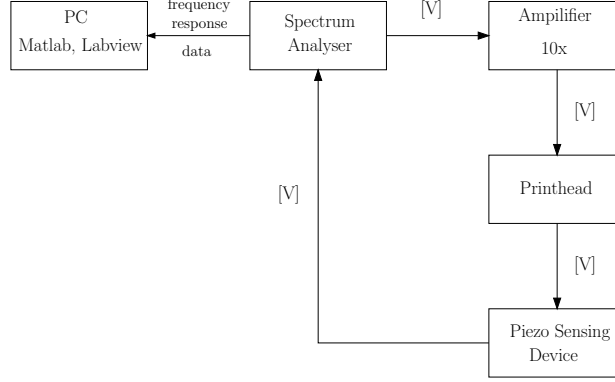


Figure 2.2: Configuration used for system identification.

With use of a piezo sensing device the corresponding piezo sensor signal is obtained. This unfiltered sensor signal is returned to the spectrum analyzer and this sequence is automatically repeated for the complete frequency range. Finally, the obtained frequency response data is captured by the PC.

In this configuration, the amplifier and the piezo sensing device are enclosed in the loop. When for example the measured frequency response is used to validate theoretical models, compensation for the enclosed hardware is needed. In Fig. 2.3, the measured frequency response is depicted for the amplifier and the piezo sensing device. Due to the limited bandwidth of

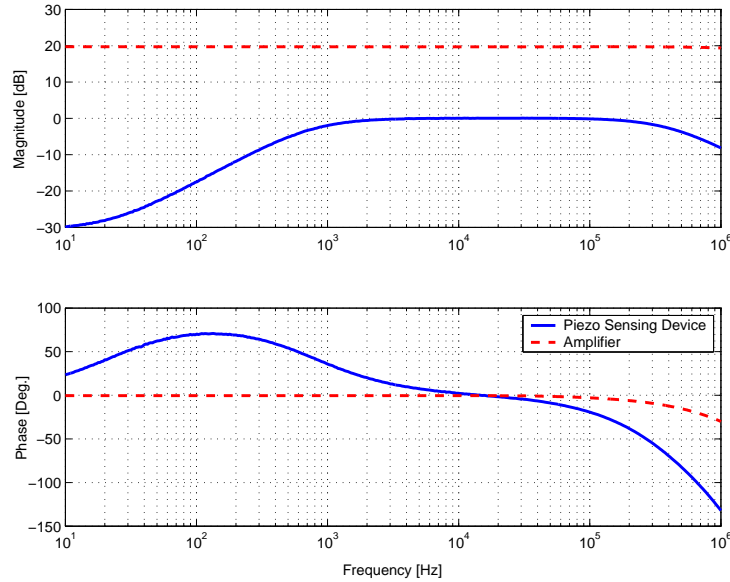


Figure 2.3: Measured frequency responses of the hardware used during identification measurements.

the amplifier some substantial phase loss is introduced for frequencies higher than 500 kHz. Besides, from the frequency response from the piezo sensing device can be concluded that it acts as a bandpass filter which is adjusted for the frequency range of interest (1 kHz upto 500

kHz). By doing so, the influence of measurement noise and offsets is decreased.

2.3 Configuration used for Control

The configuration setting used for ILC experiments is depicted in Fig. 2.4. Arbitrary wave forms can be designed in the **Matlab \ Labview** environment. The desired wave forms are generated by a waveform generator and are sent through an amplifier to the desired piezo actuator. Subsequently, the system's response (the piezo sensor signal) is sampled with a frequency of 10 MHz by the scope and is downloaded into the **Matlab \ Labview** environment on the PC. There, the measured data is filtered by a digital Butterworth low-pass filter with a cut-off frequency of 400 kHz.

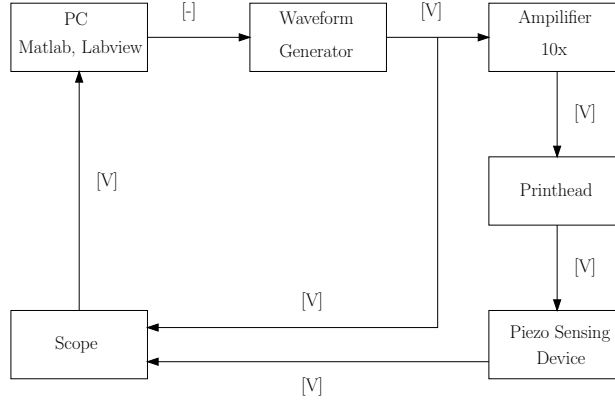


Figure 2.4: *Configuration used for ILC experiments.*

During the ILC experiments, additional hard- and software is enclosed in the loop. Since different configuration settings are used for control and identification, the obtained experimental model has to be compensated. With identification, no use is made of the waveform generator and the scope. Moreover, the measured data is not digitally filtered. The synchronization between the waveform generator and the scope causes an additional delay. Besides, the digital low-pass filter causes another additional delay and a reduced magnitude for frequencies higher than the cut-off frequency. In Fig. 2.5, the measured frequency response data is shown of the used hardware. Besides, the calculated frequency response data is depicted for a digital 4th order low-pass filter with a cut-off frequency of 400 kHz.

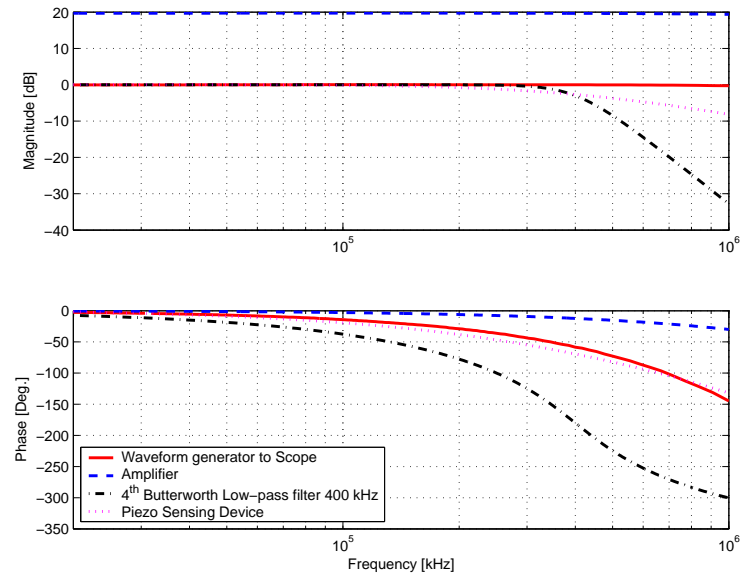


Figure 2.5: *Measured frequency responses of the hardware as used during ILC experiments.*

Chapter 3

Modeling of an Inkjet Printhead

In order to gain insight in the jetting process and in the operational issues encountered during jetting, two theoretical models of an inkjet printhead are studied. For modeling of the inkjet printhead also experimental modeling is utilized. With the obtained experimental model the theoretical models have been validated.

Modeling a printhead involves a combination of (nonlinear) piezo behavior, acoustics and fluid-mechanics including droplet formation. Usually, the resulting models are a trade-off between accuracy and complexity. For control, it is desirable to have both reasonable accuracy and small complexity. In this chapter, the three printhead models will also be assessed for the usability for control purposes.

This chapter is organized as follows. After a short introduction, the theoretical models are addressed. The theoretical models that are studied are the so-called Narrow-Gap and the wave model. First, the Narrow-Gap model is discussed in Section 3.2. Second, the wave model is discussed in Section 3.3. Next, the experimental modeling is addressed in Section 3.4. Section 3.5 concerns the validation of the theoretical models and the assessment of the usability of the three models for control purposes. Finally, in Section 3.6 the conclusions of this chapter are given.

3.1 Introduction

In Fig. 3.1 a schematic view of an inkjet channel is depicted. It consists of a channel plate, channel, connection, nozzle, nozzle-plate, a particle filter and a piezo actuator. The ink channel can be subdivided into a part that is actuated and a part that is not actuated. The piezo actuator creates acoustic pressure waves in the ink channel and the nozzle is used to concentrate velocity and pressure at the exit of the channel. The air-ink interface in the nozzle is called the meniscus. The connection is the part which connects the ink channel with the nozzle. The left side of the channel is connected to an ink reservoir. For a detailed description of the working principle of an inkjet printhead one is referred to [Nag06].

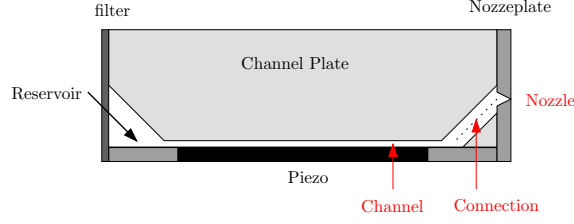


Figure 3.1: *Schematic view of an inkjet channel.*

3.2 The Narrow-Gap Model

3.2.1 Theory

The Narrow-Gap theory was originally derived in [Bel97] and describes the behavior of a thin layer of air between a fixed surface and an oscillating plate. In this configuration, the dimension of height is very small compared to the length. With this fact, the Navier-Stokes equations (which describe the acoustics) can be simplified such that an analytical solution is possible.

This Narrow-Gap theory was used to derive an analytical 1D model that describes the fluid mechanics inside the printhead channel and nozzle. The Narrow-Gap model couples the constructive properties of the printhead to the fluid mechanics of the ink for multiple channels. This boils down to calculating the channel acoustics as a result of the cross-sectional area change after piezo actuation. The cross-sectional area change of the channel due to piezo actuation and due to pressure waves (channel-wall flexibility) is calculated with the FEM package ANSYS.

The Narrow-Gap theory uses the equation of continuity, the equations of momentum, the energy equation and the ideal gas law in order to describe the acoustic behavior of the ink. First, the equations are linearized with mean values and small perturbations of pressure, density and temperature. The resulting linearized equations are simplified using a number of assumptions. The specific geometry of the channel is ideal to simplify the equations, as the length is many times larger than the channel's width and height according to the Narrow-Gap theory, i.e. the channel is a long square tube. The analytical solution of the obtained linearized and simplified equations is only known in the frequency-domain and not in the time domain. However, by coupling the obtained impulse response to an arbitrary actuation pulse, the progress of pressure and meniscus velocity can be calculated.

The advantages of the Narrow-Gap model are:

- Due to the analytical character of the Narrow-Gap model, its computational load is relatively low.
- For the same reason and due to its low computational load, the model is especially useful for redesign purposes.

For the Narrow-Gap model, the most important disadvantages are listed below:

- Since the analytical solution is only known in the frequency domain, time-dependent properties like variable filling of the nozzle and refill effects cannot be taken into account. As a result, the nozzle impedance which affects the reflection coefficient of the pressure waves at the connection-nozzle interface, does not vary under influence of the meniscus position. Consequently, the channel acoustics are not calculated correctly.
- The model assumes no mean ink flow inside the ink channel. Since the amount of ink flow inside the channel is relatively small, this assumption is acceptable for the channel (ejected droplet mass is relatively small compared to the mass of ink inside the channel). However, for the nozzle this assumption does not hold.
- The Narrow-Gap model only uses acoustics. Though this is a valid assumption for the channel, it certainly is not for the nozzle. There, fluid-mechanics govern.

3.2.2 Analyses

This section will discuss the simulation results obtained with the Narrow-Gap model. In the first place, the calculated frequency responses are discussed, namely the transfer between piezo actuation and piezo sensor signal and the transfer between piezo actuation and meniscus velocity. Next, the derived time responses will be addressed.

Frequency Response Function H_{P2P} (Piezo 2 Piezo)

In Fig. 3.2 the frequency response function from piezo actuation to piezo sensor signal (H_{P2P}) is shown. As explained in Chapter 2, the piezo sensor signal represents the time-derivative of the mean pressure under the effective piezo surface.

Based on Fig. 3.2, it is observed that for low frequencies the magnitude goes to minus infinity. This implies that there is no steady-state response and that is exactly what one would expect. If a step input is applied to the actuator, acoustic waves arise and, eventually, damp out. Furthermore, the channel resonance frequencies are clearly visible in Fig. 3.2 and can be interpreted as the occurring standing waves in the channel and its higher order modes. The explanation for the location of these resonance frequencies will be given later in this section. From the figure it also follows that these resonance modes are highly damped. Furthermore, after the first resonance frequency, the global slope of magnitude is approximately +1 (i.e. 20 dB / decade). This rather unusual slope for mechanical systems is caused by the time-differentiating action of the piezo sensor, since not the piezo charge but the piezo current is measured. As a result, the higher order modes have a larger gain than the lower frequency modes.

Frequency Response Function H_{P2PI} (Piezo 2 Piezo Integrated in Time)

As described above, the piezo sensor signal represents the time-derivative of the pressure. When this signal is integrated in time, the pressure itself is obtained. The bode plot of the transfer

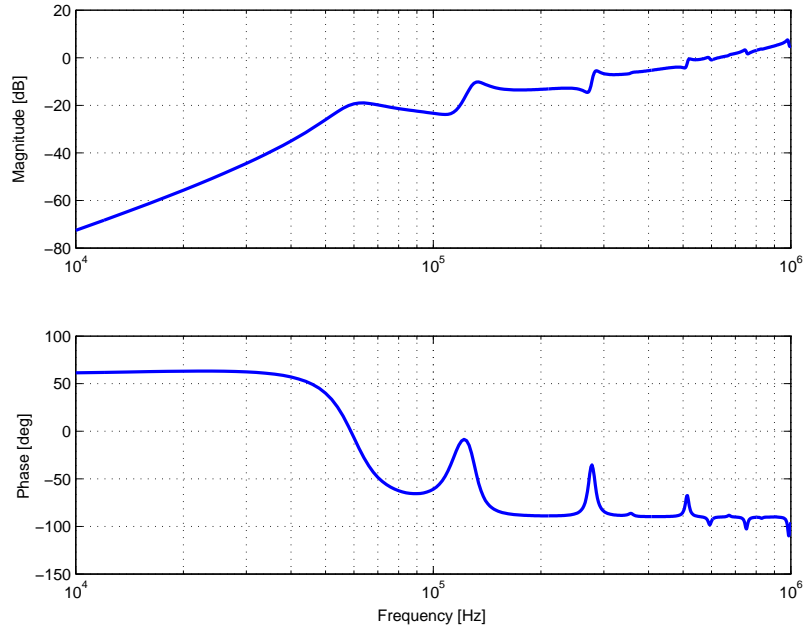


Figure 3.2: *Theoretical frequency response function from piezo actuation to piezo sensor.*

between piezo actuation and piezo sensor signal integrated in time is depicted in Fig. 3.3.

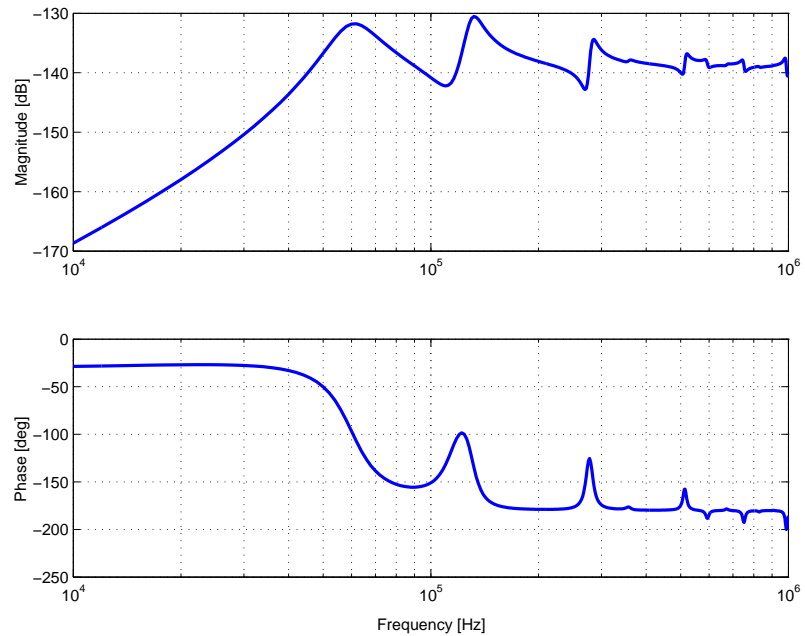


Figure 3.3: *Theoretical frequency response function from piezo actuation to piezo sensor signal integrated in time.*

Due to the time-integrating action, a change of slope in magnitude of -1 and a change in phase of -90 degrees can be seen with respect to the frequency response function H_{P2P} . Con-

sequently, the magnitude plot is rotated clockwise resulting in a lower gain for the higher frequency range.

When the piezo sensor is deployed for control purposes, it is chosen to work with the time-integrated piezo signal. This offers two advantages. First, instead of the derative of the pressure, the pressure itself is controlled. Second, for the design of the ILC controller, it is preferable to deal with the time-integrated piezo signal since the important dynamics (the lower resonance modes) are now represented by the largest singular values. For more information, one is referred to [Nag06].

Frequency Response Function H_{P2MV} (Piezo 2 Meniscus Velocity)

The frequency response of the meniscus velocity as function of piezo actuation (H_{P2MV}) is shown in Fig. 3.4. Since the pressure in front of the nozzle (and so the channel acoustics) is the driving force for meniscus movements, the frequency response functions of H_{P2PI} and H_{P2MV} have more or less similar properties. As expected, the same (channel) resonance frequencies can be seen and some additional delay is visible in the phase plot of H_{P2MV} with respect to H_{P2PI} . This additional delay is caused by the time needed for the pressure waves to reach the nozzle and to affect the meniscus.

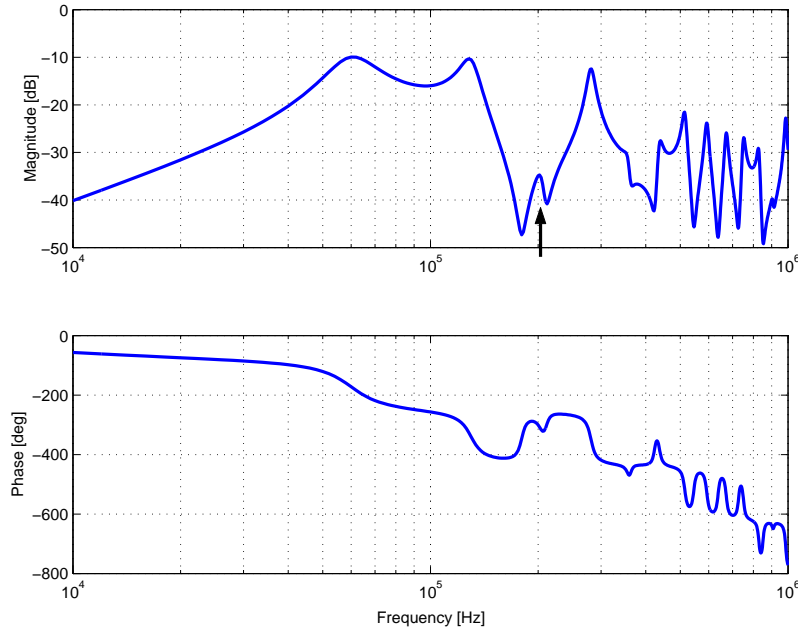


Figure 3.4: *Theoretical frequency response function from piezo actuation to meniscus velocity.*

The explanation of the location of the resonance frequencies is explained with use of Table 3.1. The calculated resonance frequencies can be found in the left column and corresponds with the resonance frequencies as depicted in Fig. 3.4. As explained in [Nag06], the basic vibration mode for a fluid line with one open end (reservoir) and one closed end (nozzle) is a $\frac{1}{4}\lambda$ resonator. In fact, for the higher frequency range, the channel, connection and nozzle can be seen as a fluid line with one closed and one open end and the higher order frequency modes

calculated resonance frequencies [kHz]	$\frac{1}{4}\lambda$	predicted [kHz]	Δ [%]	λ
62	$\frac{1}{4}$	43	-45%	0.362
130	$\frac{3}{4}$	128	-1%	0.253
214	$\frac{5}{4}$	214	0%	0.250
296	$\frac{7}{4}$	300	1%	0.247
380	$\frac{9}{4}$	385	1%	0.247

Table 3.1: *Calculated and predicted resonance frequencies.*

can be approximated based on the $\frac{1}{4}\lambda$ resonator. Consequently, pressure-waves are more reflected at the connection-nozzle interface and less transmitted into the nozzle. However, for the lower frequency range, the nozzle impedance decreases and the nozzle acts more as an open end. Thus with decreasing the frequency, the basic resonance mode is shifted from the $\frac{1}{4}\lambda$ resonator towards the $\frac{1}{2}\lambda$ resonator (based on a fluid line with two open ends). This is clarified in Table 3.1 by assuming that the third resonance mode is based on the $\frac{1}{4}\lambda$ resonator and therefore is equal to the third harmonic mode, i.e. $f_3 = \frac{5}{4}\lambda = 214$ kHz.

Based on this assumption, the basic vibration mode is calculated and equals 43 kHz ($= \frac{214}{5}$). In a similar way, the higher order modes are calculated and are addressed in the third column. The difference between the resonance frequencies obtained with the Narrow-Gap model and the predicted resonance frequencies are presented in the fourth column in percentage. Obviously, the difference for the third mode is zero since the prediction is based on this resonance frequency. One can see that for the first two modes the difference is negative and the predicted frequencies are too low. In the last column, this difference is used to calculate the approximated basic resonator. Indeed, for the higher frequency range, the basic resonator approximates the $\frac{1}{4}\lambda$ resonator and for the first two resonance modes the basic resonator is shifted towards the $\frac{1}{2}\lambda$ resonator. This validates the assumption that for higher frequencies the nozzle acts more and more as a closed end since viscous dissipation increases the nozzle impedance more at faster speed variations. The same line of reasoning can be used to explain the decreasing amplitude of the higher order resonance modes in the frequency response function H_{P2MV} of Fig. 3.4. At last, it can be concluded that for higher frequencies the damping of the resonance modes decreases.

Furthermore, in contrast to H_{P2P} and H_{P2PI} some anti-resonances can be seen in the frequency response of H_{P2MV} . Moreover, the anti-resonances occur in a repeating sequence in the frequency range, namely 190, 380, 570, 760 kHz, etc.... These anti-resonances can be explained by the phenomenon destructive interference. A well known example of destructive interference is anti-noise. In Appendix D is explained that with actuation of the printhead channel, the same phenomenon can occur. It says that if the length λ of the induced pressure waves exactly equals the length of the piezo actuator, the induced pressure waves are completely canceled out and no energy is coupled into the channel. In a similar way, this also hold for the higher order modes, i.e. 2λ , 3λ , 4λ , etc... So the condition for destructive interference yields:

$$n\lambda = L_{act} \quad (3.1)$$

with n denoting a positive integer. As a result, the frequencies of the anti-resonances are only determined by the length of the piezo actuator and by the effective speed of sound in ink.

So, the location of the resonance modes is determined by the channel's length and the location of the anti-resonance modes by the length of the piezo actuator. Given a certain geometry, the situation might exist that an anti-resonance mode is located near a resonance mode. This is exactly the case with the current geometry. The third resonance mode located at 214 kHz is barely excited since it is closely located to the frequency where the first destructive interference occur (190 kHz). This is clearly visible in the frequency response function H_{P2MV} depicted in Fig. 3.4, indicated by the arrow. Note that the same holds for the 5th resonance mode, which is exactly located at the location of the second destructive interference (380 kHz).

The same line of reasoning can be used to explain why not all the given resonance frequencies in the first column of Table 3.1 are visible in the frequency response functions H_{P2P} and H_{P2PI} . When for example the resonance modes are considered of H_{P2PI} depicted in Fig. 3.3, it can be observed that the 1st, 2nd and 4th resonance modes (62, 130 and 296 kHz respectively) are clearly visible. As expected, the 3rd and the 5th resonance mode (214 and 380 kHz respectively) are not presented since they are barely excited.

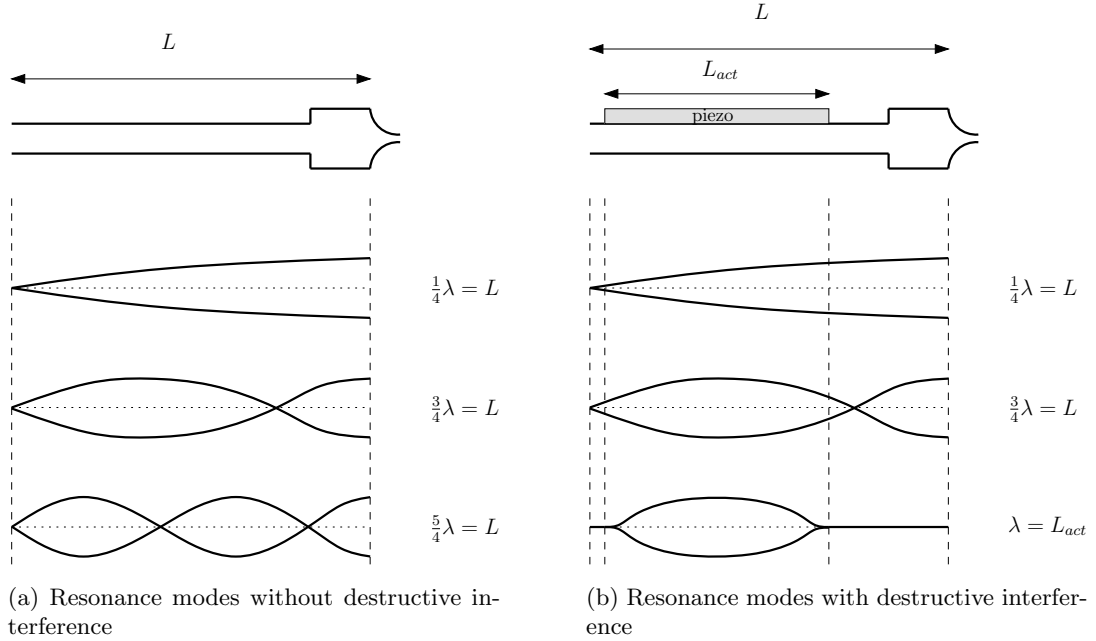


Figure 3.5: *Standing wave patterns representing the resonance modes for an inkjet channel. As a result of destructive interference, the third resonance mode is barely excited (plot b).*

To give a better understanding of the above mentioned, the standing wave patterns of an inkjet channel are depicted in Fig. 3.5. At the left side, three standing waves patterns are depicted ($\frac{1}{4}\lambda$, $\frac{3}{4}\lambda$ and the $\frac{5}{4}\lambda$ mode), representing the first three resonance modes of an inkjet channel (62, 130 and 214 kHz respectively). However, due to the presence of the piezo actuator, destructive interference occur. As a result of the given geometry, the third resonance mode is barely excited. This is clarified at the right side of Fig. 3.5, where now the channel is equipped with a piezo actuator. The depicted wave patterns are a result of a pure sinusoidal

actuation of the piezo with a certain frequency. When this actuation frequency equals the resonance frequency, the depicted standing wave patterns are obtained. As expected, the same standing wave patterns can be found for the first two resonance modes. However, due to the destructive interference (190 kHz) the third resonance mode (214 kHz) is less excited. The wave pattern resulting from a sinusoidal actuation of 190 kHz is depicted in the lower right corner. It can be seen that with destructive interference only pressure waves occur underneath the piezo actuator and that the rest of the channel is in rest. In Appendix D is explained why exactly this wave pattern occurs underneath the piezo actuator. Now, if the frequency of the sinusoidal actuation signal equals 214 kHz, it is that close located to 190 kHz that more or less the standing wave pattern as depicted at the lower right side occurs and not the wave pattern corresponding to the third resonance mode (lower left side).

Speaking in terms of controllability, given the current geometry, one can conclude that the system H_{P2MV} is not completely controllable since not all frequencies can be excited in the nozzle. Besides, the system H_{P2P} is not completely observable. When the length of the induced pressure waves equals the length of the piezo actuator, a netto pressure of zero is measured since the mean pressure over the piezo length is measured. However, this same condition was found for the origination of destructive interference (3.1). This means that for pressure waves for which (3.1) holds, they cannot be measured with the piezo, but also, they cannot be actuated with the piezo. For this reason, no anti-resonances are present in the frequency response function H_{P2P} . Note that during a normal jet cycle, frequencies can be present in the channel which cannot be measured with the piezo sensor. One might question how these frequencies can arise in the channel (since they cannot be excited by the actuator¹), but since the dynamics inside the nozzle are nonlinear, these specific frequencies can exist in the channel.

Time Responses

With making use of the Narrow-Gap model, the time responses for different variables resulting from a standard trapezoidal actuation pulse are shown in Fig. 3.6.

In the upper left-hand corner the piezo sensor signal is depicted and represents the time-derivative of the pressure under the piezo surface. In the lower left-hand corner the time-integrated piezo signal is depicted which represents the mean pressure under the piezo surface. FFT calculations revealed that the depicted responses are dominated by the first two resonance frequencies, i.e. 62 and 130 kHz. In the plots, the standard trapezoidal actuation signal is also depicted. On the positive flank, the piezo retracts and the volume of the channel increases and a negative pressure is induced which propagates in both directions. The negative pressure waves are reflected at the nozzle with the same sign and at the reservoir with reversed sign. Just when the positive pressure wave which was reflected at the reservoir is exactly located underneath the middle of the piezo actuator, the actuation voltage is released and the piezo returns to its original position. Consequently, the positive pressure wave traveling rightwards is amplified such that it is large enough to jet a droplet when it reaches the nozzle. For a more detailed description of the jet cycle, the reader is referred to [Nag06]. In the upper right-hand corner the pressure in front of the nozzle is depicted which

¹If a sinusoid of a certain frequency is the input of a linear system, only a sinusoid of that specific frequency must be observable in the output.

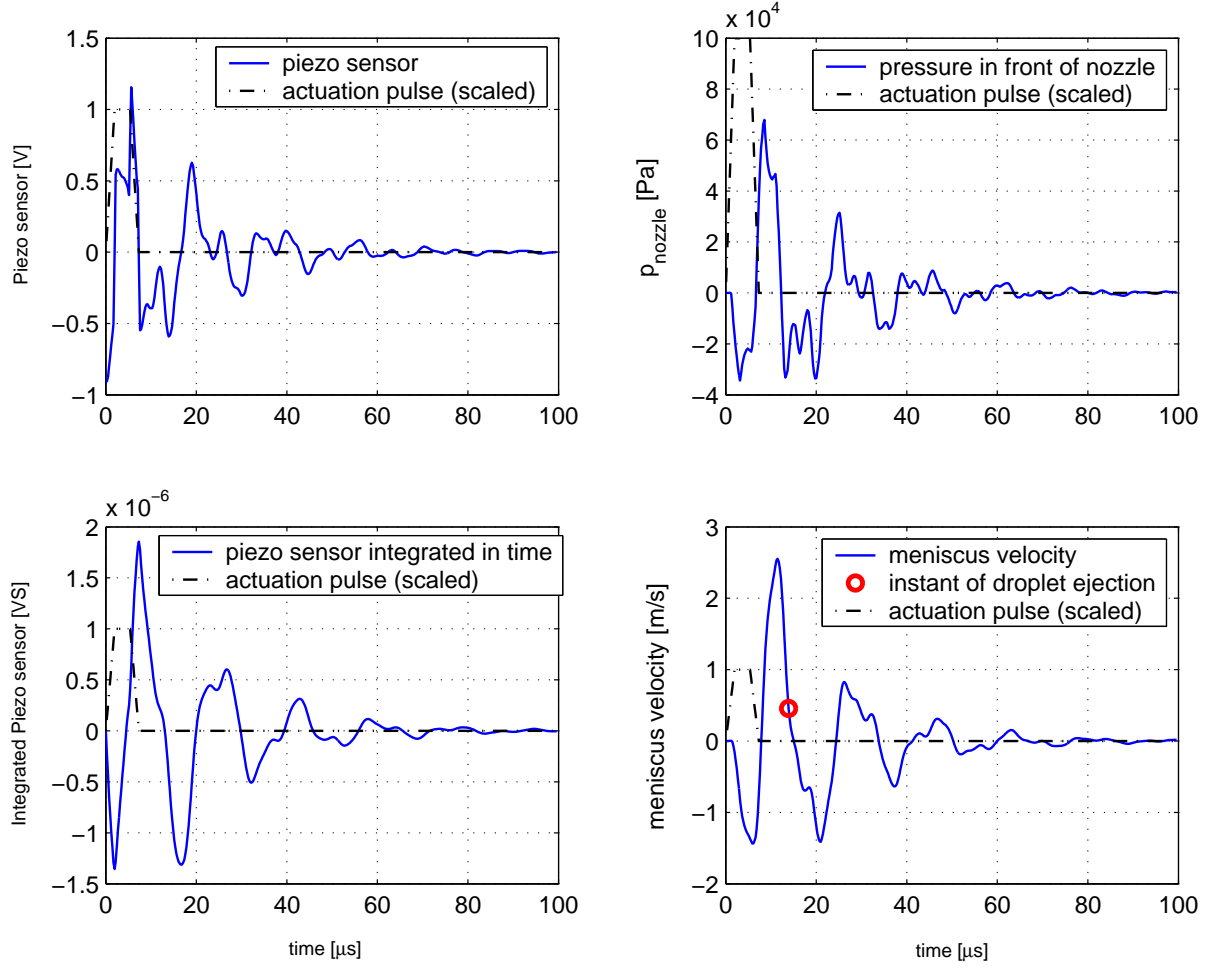


Figure 3.6: *Time responses calculated with the Narrow-Gap model.*

causes the ink in the nozzle to move. The velocity of the meniscus (interface ink-air in nozzle) is depicted in the lower right-hand corner. Due to the induced negative pressure, first the meniscus is retracted. Then, the positive pressure wave reaches the nozzle and the ink inside the nozzle is accelerated outwards resulting in the ejection of a droplet. Typically, after $15 \mu\text{s}$ a droplet is ejected. Note that it takes about $100 \mu\text{s}$ for the pressure waves to be completely damped.

3.3 Wave Model

3.3.1 Theory

The wave model is a 1D finite volume model that describes both the channel acoustics and the fluid-dynamics in the nozzle and is developed by de Zeeuw [dZ05]. With the above described Narrow-Gap model, the Navier-Stokes equations are strongly simplified using the Narrow-Gap theory such that an analytical solution of the governing equations is known. With the

wave model the governing equations are numerically solved using the finite volume method, see [TAP97]. This boils to solving the discretized Navier-Stokes equations on a meshed grid in a time-discrete matter. On each time step, the channel acoustics are calculated. Based on the pressure gradient over the nozzle, the flow in the nozzle is calculated. A modified form of the Dijkman model is used to predict whether a droplet is created and, if one is created, it provides an estimate of the ejected droplet speed and size.

The advantages of the wave model are listed below:

- By constructing the model from first principles whenever possible, a relative simple model is obtained providing good insights. Several modeled effects are compensated by empirical constants in order to predict the experimental results more accurately.
- Time-effects as variable mass inside the nozzle and refill are taken into account. Since the channel acoustics and the fluid-dynamics inside the nozzle are computed simultaneously, these effects will also influence the channel acoustics. As discussed in the sequel of this chapter, this will be the main advantage of the wave model with respect to the Narrow-Gap model.
- Since refill effects of the nozzle are accounted for, the wave model is exceptional suited for the simulation of jetting a sequence of droplets whereas with the Narrow-Gap model only the jetting of single droplet can be considered.
- The computational time is low.

The main disadvantage of the wave model is the following. By fitting the empirical constants on the experimental results, a good fit is obtained. Consequently, the model's utility for redesign purposes is questionable. Note that not only printhead redesign is mentioned. Also redesign of the printhead actuation signal is mentioned, which is exactly the subject of this thesis. Therefore, it remains to be seen to what extent the model is useful for this purpose.

3.3.2 Analyses

This section will address the simulation results obtained with the wave model. In Fig. 3.7 the meniscus velocity and position resulting from a standard trapezoidal actuation are depicted. The shown meniscus position is the mean value over the cross-sectional area in the nozzle.

As expected, on the positive actuation flank a negative channel pressure is induced and the meniscus retracts. Subsequently, on the decreasing actuation flank, a positive pressure is induced and the meniscus moves out. In the wave model it is assumed that the droplet formation process starts when the meniscus moves outside the nozzle-plate (meniscus position $> 0 \mu\text{m}$) and, if several conditions are met, a droplet is ejected when the meniscus velocity turns negative again. The time instant that the droplet is ejected is also depicted in the figure. On that time instant, a discontinuity in meniscus position can be seen. Since a certain amount of ink is ejected from the nozzle, this is modeled as a discontinuity in the meniscus position (and consequently in mass). This is done by assuming that the meniscus position decreases with 80% at the moment of droplet ejection. After droplet ejection, one can see that it takes around $100 \mu\text{s}$ for the meniscus to become in rest. During the time in

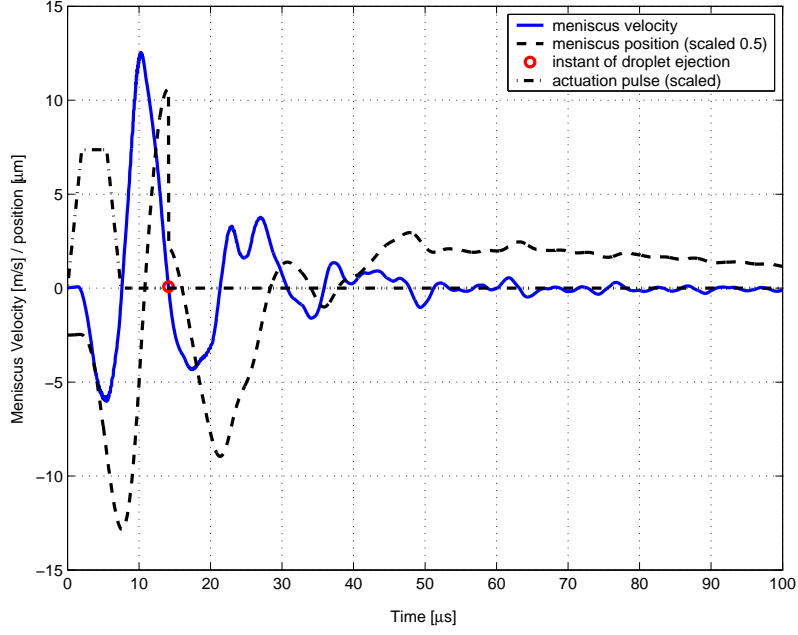


Figure 3.7: *Time responses calculated with the wave model.*

which the channel acoustics damp out (and so the meniscus), the nozzle is filled with new ink. This is called the nozzle refill and is clearly visible in Fig. 3.7. In fact, nozzle overflow occurs since the meniscus position is larger than $0 \mu\text{m}$ during the refill. This means that the nozzle is completely refilled with ink and that the ink is even pushed out of the nozzle. As a result, wetting of the nozzle-plate might occur. The phenomenon refill and its possible result, wetting, are further addressed in Chapter 4. Fig. 3.7 underlines that the meniscus is not at rest after droplet emission. If the channel is actuated again before these residual vibrations are damped, the properties of the resulting droplet changes. This is demonstrated in Fig. 3.8, where the so-called drop-on-demand (DOD) curve calculated with the wave model is shown. The figure displays the droplet speed as function of the jet-frequency and clearly shows the variations when the jet frequency is varied. In Chapter 4, more attention will be paid to the DOD-curve based on physical grounds. Furthermore, it will be explained why it is highly undesirable that the droplet properties (same variations can be found in droplet volume) vary as function of jet frequency.

3.4 Experimental Model

For modeling of the ink channel dynamics also experimental modeling is utilized. With experimental modeling, the theoretical models described in the previous sections can be validated. The ink channel dynamics are identified by measuring the frequency response from piezo actuator to piezo sensor and a linear empirical model is obtained by fitting the measured frequency response data. In order to apply the identification procedure used during this research, the following assumption is required:

- The to be identified dynamics, i.e. the dynamics between piezo actuator and piezo

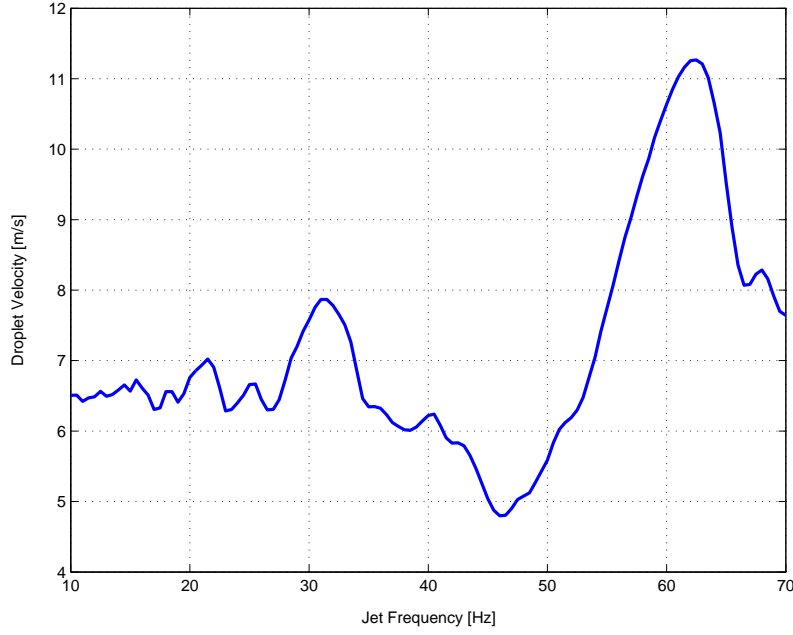


Figure 3.8: *Calculated drop speed as function of the jet frequency using the wave model.*

sensor signal behave linear as long as no droplet is being jetted.

In the jetting situation, at some point during the actuation cycle a small amount of ink is ejected. This sudden jump in mass introduces nonlinear behavior. Till this point it is questionable to what extent this will influence the channel acoustics. The used identification technique however, is only valid for linear systems. To avoid possible inaccuracies, the identification is performed using small actuation signals that guarantee a non-jetting situation. In this way, an experimental model is derived that, theoretically, is only valid for non-jetting situations. Consequently, the validity of the obtained experimental model should be investigated, especially for the jetting situation.

The next section will discuss the identification experiments in terms of frequency response measurements using the sine-sweep technique. Subsequently, a linear model is obtained by fitting the measured frequency response data. The model fitting and the validation of the obtained experimental model are addressed in Section 3.4.2 and 3.4.3 respectively.

3.4.1 Frequency Response Measurements

The frequency response from piezo actuation to piezo sensor signal is measured with use of a spectrum analyzer by applying the sine-sweep technique. The configuration used for the identification measurements is described in Chapter 2. The spectrum analyzer outputs a sine-sweep for a frequency range with N points. For each frequency point, the average of 128 piezo responses is determined in order to decrease the effect of noise and subsequently, the FFT is calculated. During the experiments, the frequency response is measured within the range from 20 kHz upto 1 MHz using 400 logarithmical equally spaced points. The frequency

response data is measured with a sweep-voltage of 2.5V. Typically, actuation voltages for jetting droplets are around 20V. By doing so, the sine-sweep voltage is chosen sufficiently low in order to avoid droplet ejection.

As explained in Chapter 2, during identification measurements the amplifier and the piezo sensing device are enclosed in the loop. Consequently, the measured frequency response suffers from additional gain and phase loss due to the limited bandwidth of the amplifier and due to the bandpass filtering of the piezo sensing device (see Fig. 2.3). For this reason, the frequency response data is compensated in order to obtain the frequency response of the dynamics between piezo input and piezo sensor signal alone. Then, validation of theoretical models is justified. The resulting frequency response data is depicted in Fig. 3.9.

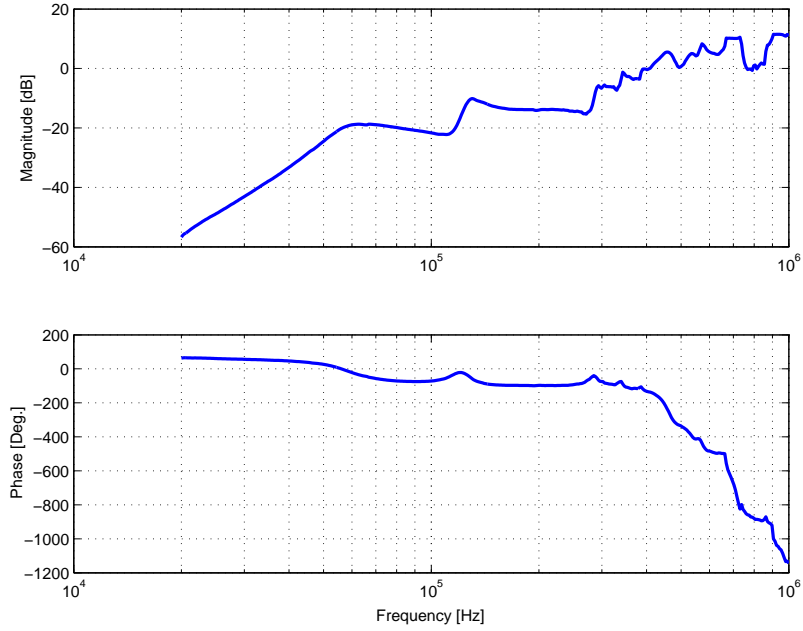


Figure 3.9: *Measured frequency response data from piezo input to piezo output compensated for additional hardware used during identification.*

In the figure, the resonance frequencies are clearly visible. As discussed in Section 3.2.2, these resonance frequencies can be related to the occurring standing waves in the ink channel.

In Fig. 3.10 is shown that there exist a rather large measurement uncertainty in the higher frequency range. In the figure, four frequency response measurements are depicted for the same ink channel using the same sweep-voltage of 2.5V. It can be seen that above the 400 kHz, the mismatch between the measurements significantly increases. But fortunately, the measurement uncertainty within the range of interest (i.e. the lower order resonance modes) is small.

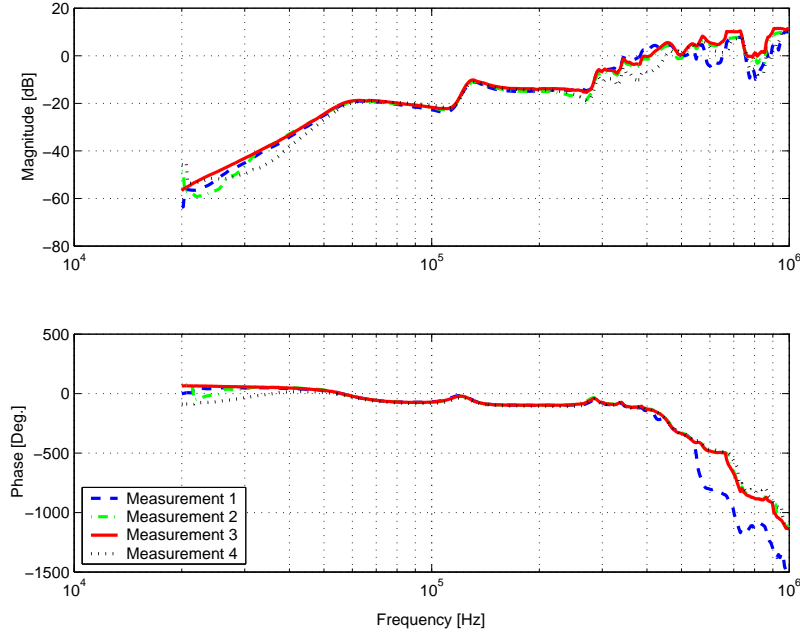


Figure 3.10: *Measured frequency response data from piezo input to piezo output for the same ink channel; Illustration of the measurement uncertainty.*

3.4.2 Model Fitting

In order to obtain an experimental model, a linear continuous-time state-space model is fitted to the measured frequency response data using the `Matlab` command `frsfit`, which is a least-square fit routine that guarantees a stable fit. Before applying the fit-routine, first the frequency response data is compensated. The reason for doing that is as follows. The experimental model is needed for the design of the ILC controller and describes the dynamics between the piezo actuator and the piezo sensor. The frequency response data depicted in Fig. 3.9 represents these dynamics. However, during ILC experiments performed on the experimental setup (see Section 2.3), additional hardware is enclosed in the loop, namely a waveform generator, amplifier, piezo sensing device and a scope. As explained in Section 2.3, this hardware introduces additional dynamics. For this reason, the experimental model needed for ILC synthesis must comprise all these dynamics enclosed in the loop. By doing so, the compensated measured frequency response data (and so the fitted model) represents the printhead dynamics with additional hardware used during control experiments. In Fig. 3.11, the resulting frequency response data and the 16th order model fit are depicted.

By choosing an order of 16, a good fit is obtained upto 350 kHz and the most important dynamics are captured in the experimental model.

3.4.3 Model Validation

For validation of the experimental model, the piezo sensor signal is measured for a standard trapezoidal actuation pulse using different voltages (5V, 11V, 12V and 20V). With 5V and 11V actuation, no droplet emission occurs and for the 12V and 20V actuation a droplet is

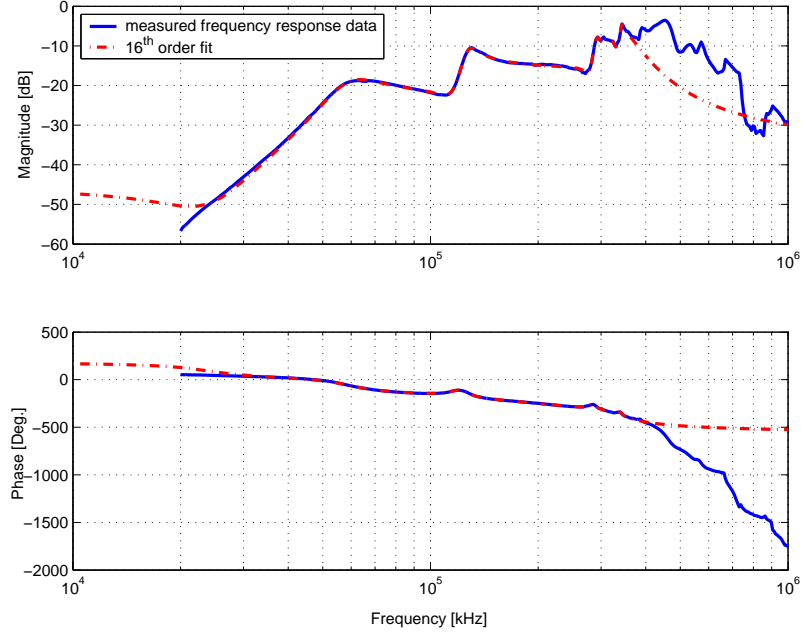


Figure 3.11: *Measured frequency response data compensated for the hardware during control experiments and the 16th order fit.*

ejected. Note that the transition from a non-jetting to jetting situation occurs between 11V and 12V. In Fig. 3.12, the measured responses are depicted. In the same figure, the simulated piezo sensor signals are depicted, using the experimental model. Based on a comparison of the modeled and the measured signals in a non-jetting situation (plot *a* and *b*), it is clear that the model is accurate since the responses match reasonably good. When the responses for the jetting situation (plot *d* and *c*) are evaluated, it can be seen that the modeled responses are less accurate. For the first 15 μs the general response is predicted quite well (with exception of the magnitude of the second negative peak). After that time instant, a significant mismatch can be found between the modeled and the measured responses. Typically, around this specific time instant, a droplet is ejected. So after droplet ejection ($\pm 15 \mu\text{s}$), the modeled responses differ due to the introduced nonlinearity as a result of the droplet ejection. In general, linearity can be assessed by checking the superposition principle. It simply states that if an input $u_1(t)$ produces output $y_1(t)$ and input $u_2(t)$ produces $y_2(t)$, the linearly combined input $u(t) = au_1(t) + bu_2(t)$ must produce the linearly combined output $y(t) = ay_1(t) + by_2(t)$ for arbitrary scaling factors a and b . In Fig. 3.13 this is done for a non-jetting situation.

It shows the measured piezo response on a 11V pulse (solid line). Besides, the measured response on a 5V actuation is upscaled with factor $\frac{11}{5}$ and is also depicted in the figure (dashed line). It can be concluded that both responses matches reasonable good and the superposition principle holds for the non-jetting situation. In Fig. 3.14, the superposition principle is checked for the jetting situation. Now, the measured responses on a actuation pulse with a just-non-jetting voltage (11V) and a just-jetting voltage (12V) are upscaled to a 20V actuation response. In both plots, the measured response on this 20V actuation is also depicted. In the left plot, where in fact a non-jetting situation is upscaled to a jetting situation, it can be seen that the superposition principle does not hold. Note that the major

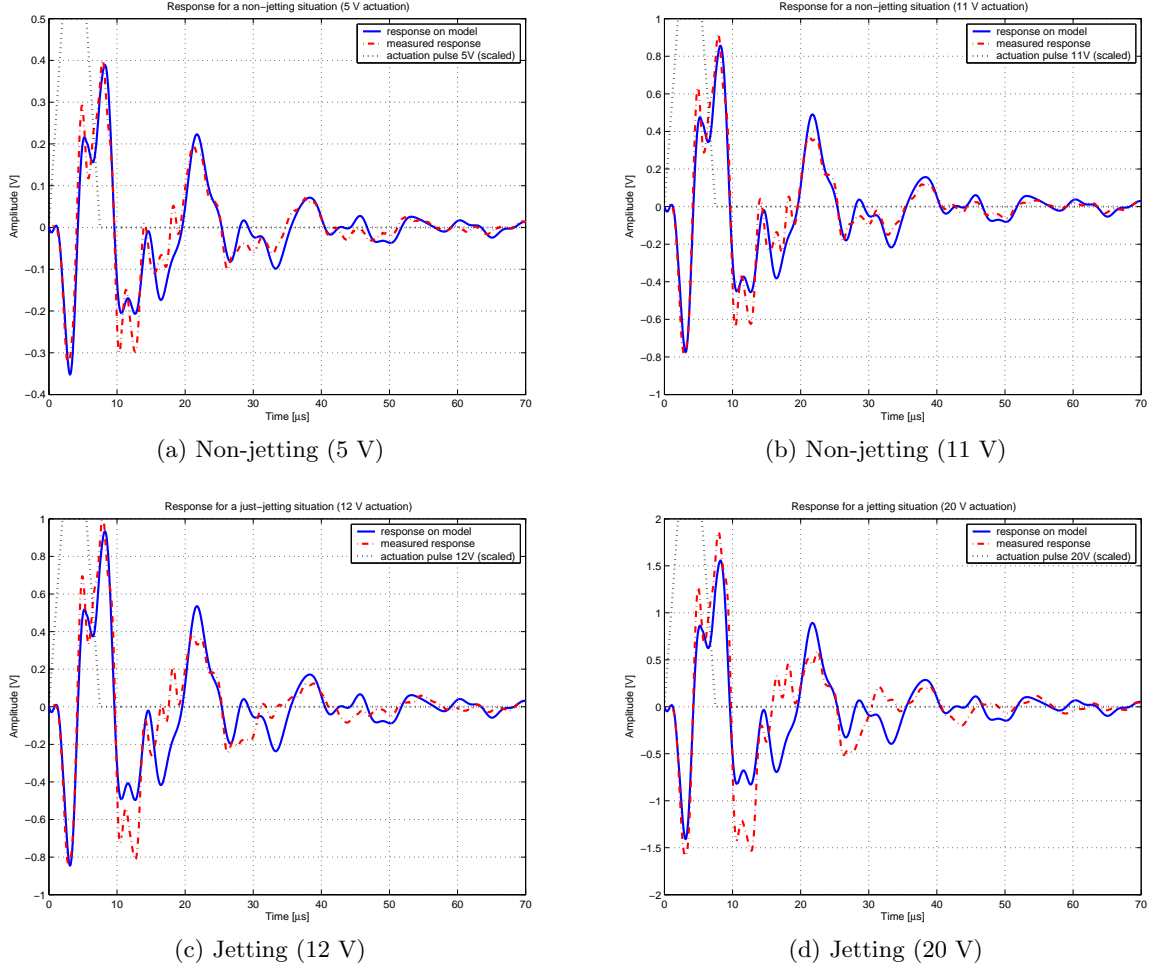


Figure 3.12: Measured and modeled piezo sensor signals for jetting and non-jetting situations resulting from a standard trapezoidal pulse.

error is introduced around the time instant that the droplet is ejected. In the right plot, where a jetting situation is upscaled to another jetting situation, it can be seen that the superposition principle does hold since both responses match reasonable good. Based on these findings can be concluded that:

- The identified dynamics, i.e. the dynamics between piezo actuator and piezo sensor signal behave linear as long as no droplet is being jetted.
- When a droplet is being jetted, a certain nonlinearity is introduced in the identified dynamics. The major cause of this nonlinearity is expected to be the discontinuity in mass inside the nozzle when a droplet is ejected. Apparently, this nonlinear effect is large enough to significantly affect the nozzle impedance such that the channel acoustics are influenced.
- The obtained experimental model is accurate for non-jetting situations, but some inaccuracies are obtained for jetting situations.

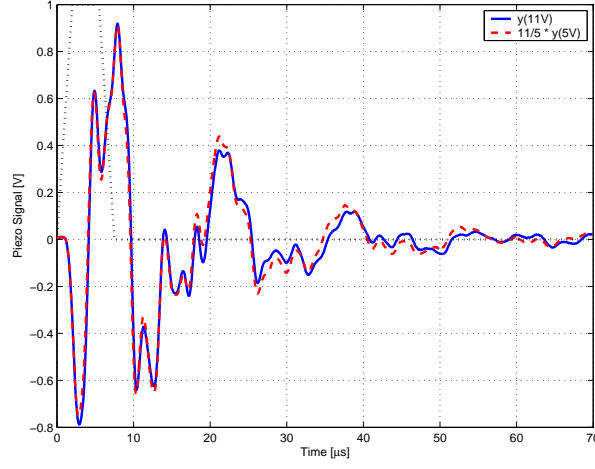


Figure 3.13: *Superposition test for a non-jetting situation using the measured piezo signals (11V and $\frac{11}{5} \times 5V$ response).*

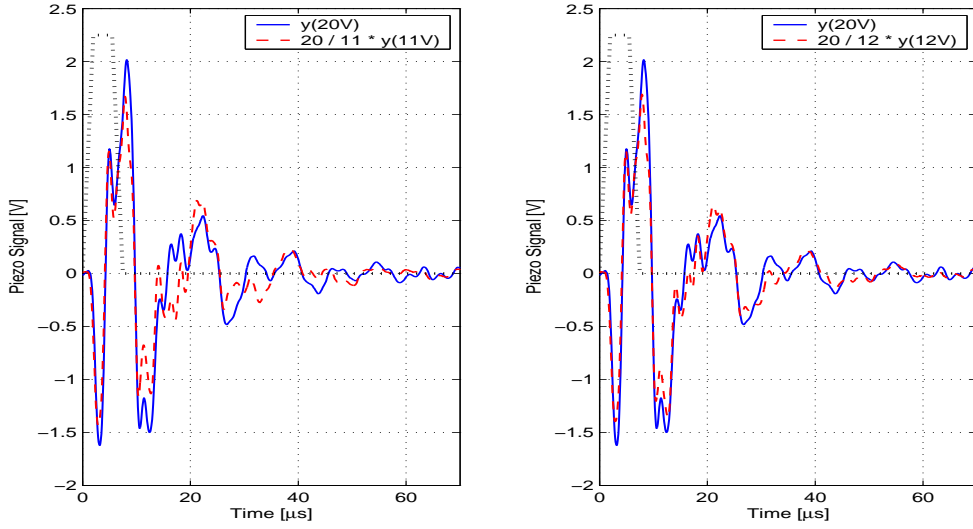


Figure 3.14: *(left) Superposition test for a just-non-jetting situation (20V and $\frac{20}{11} \times 11V$) and (right) for a just-jetting situation (20V and $\frac{20}{12} \times 12V$).*

- The inaccuracies obtained with the modeled time responses concern mainly gain related differences whereas the overall oscillatory behavior is matched quite well. Based on this finding, one can conclude that the resonance frequencies as depicted in Fig. 3.9 are measured accurately.

3.5 Discussion

In the previous sections the Narrow-Gap model, the wave model and the experimental model were addressed. In this section, both the theoretical models will be validated and the fundamental difference between the models will be discussed. Moreover, the practicability of the

three discussed models for control purposes will be assessed.

First, the measured frequency response is compared with the frequency response obtained with the Narrow-Gap model. Although the geometry used in the Narrow-Gap model corresponds with that of the printhead under investigation, the calculated resonance frequencies did not match the measured ones exactly. However, by adapting the parameter concerning the stiffness of the ink channel (β , see Appendix A) a good fit is obtained. Both the measured and the modeled frequency response data are depicted in Fig. 3.15.

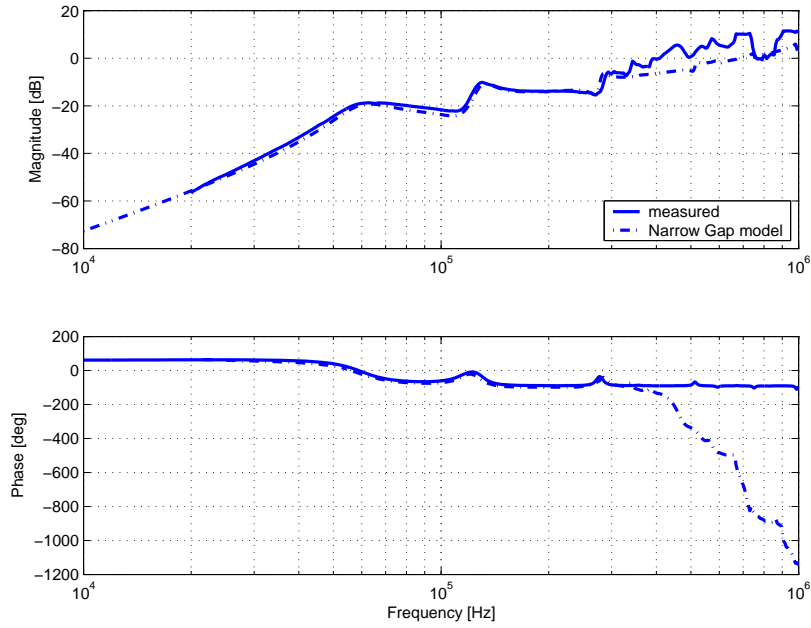


Figure 3.15: *Measured frequency response from piezo input to piezo output compared with the frequency response obtained with the Narrow-Gap model.*

It can be seen that after the parameter adaptation a good match is obtained for both the gain and the phase plot. Only for the higher frequencies (> 350 kHz) a mismatch occurs. However, it was already demonstrated that for the higher frequencies a large measurement uncertainty exist.

Next, the wave model is validated. Since frequency response data is not directly available with the wave model, it is chosen to validate the wave model by means of the DOD-speed curve. Such a curve displays the drop speed as function of the jet frequency and is already discussed in Section 3.3. By adaptation of several empirical model constants and the earlier mentioned β parameter, a good fit is obtained. Both the measured and the modeled DOD-speed curves resulting from a standard trapezoidal actuation are depicted in Fig. 3.16. Note that by means of this curve the frequency of the first channel resonance mode can be derived. When the jet frequency equals the frequency of the first resonance mode, a maximum in droplet speed can be found, i.e. 62 kHz. Besides, when the depicted curves are observed more closely it can be seen that for the lower jet frequencies the measured drop speeds are lower than the calculated drop speeds. In Chapter 5 will be demonstrated that this mismatch is caused by wetting of

the nozzle-plate, a phenomenon that is not accounted for with both the theoretical models.

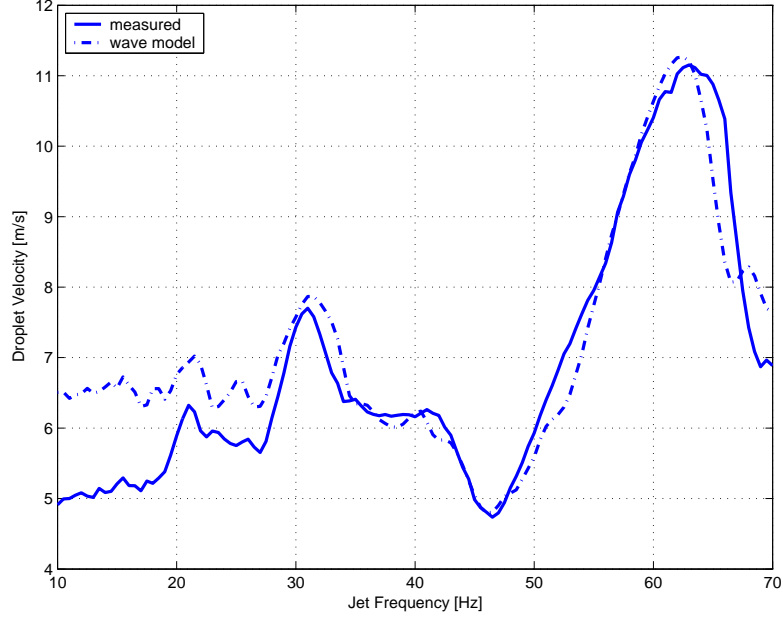


Figure 3.16: *Measured and calculated drop speed as function of the jet frequency using the wave model.*

So the parameters of both theoretical models are adapted such that, among other things, the frequency of the first resonance mode is predicted well. This first resonance frequency is dominating the piezo response resulting from a standard trapezoidal pulse. Now, the modeled piezo sensor signals are compared to the measured piezo sensor signal. In both plots of Fig. 3.17, the measured piezo sensor signal resulting from a standard trapezoidal pulse is depicted. Besides, in the upper plot the modeled sensor signals using the Narrow-Gap and the experimental model are shown. In the lower plot, the sensor signal calculated with the wave model is depicted. Note that the depicted signals corresponds to the jetting situation. In the previous section already was addressed that the obtained experimental model is inaccurate for jetting situations. In Fig. 3.17 it can be seen that the same inaccuracies are obtained with the Narrow-Gap model, indicated by the arrow in the upper plot and is typically the moment of droplet ejection. In the lower plot, the piezo sensor signal derived from the wave model is shown. Now, despite the droplet ejection no significant mismatch can be found.

So with the wave model, the piezo sensor signal is modeled accurately and with the Narrow-Gap model the same inaccuracies are obtained as with the experimental model. This can be explained as follows. The Narrow-Gap model calculates the channel acoustics using a fixed nozzle impedance. Contrarily, the wave model calculates the channel acoustics using a variable nozzle impedance. This nozzle impedance varies as a result of the moving meniscus inside the nozzle and determines the reflection condition at the connection-nozzle interface. In other words, the Narrow-Gap model assumes that the meniscus position is fixed, whereas the wave model calculates the movement of the meniscus under influence of a pressure drop over the nozzle. Based on Fig. 3.17, it can be concluded that modeling the nozzle impedance as a variable is necessary in order to calculate the channel acoustics accurately. The same line

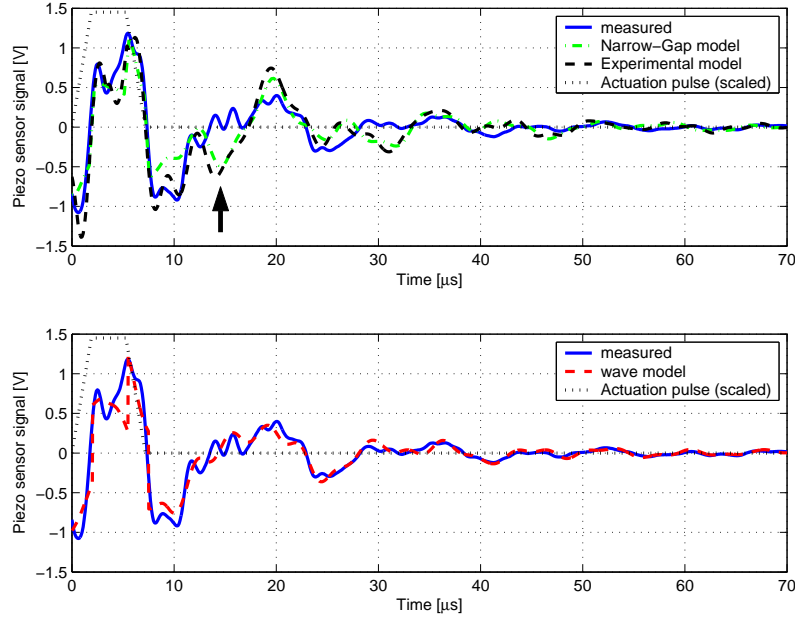


Figure 3.17: *Measured and modeled piezo sensor signal using the wave model and the Narrow-Gap model.*

of reasoning can be used in order to explain the model inaccuracies obtained with the experimental model for jetting situations: the discontinuity in mass as a result of the droplet ejection significantly affects the nozzle impedance such that the channel acoustics are influenced.

Finally, for the design of the ILC controller it is chosen to work with the experimental model. The reason for doing this is that with the experimental model the location of the resonance frequencies are predicted very good, especially the first two. Since the time responses are mainly dominated by these first two resonance frequencies, it is crucial for the ILC controller design that these frequencies are predicted accurately. Despite the modeled inaccuracies for jetting situations, the obtained experimental model forms a suitable starting point for the implementation of ILC on an inkjet printhead. In Chapter 5 is demonstrated that ILC implemented on the actual system can handle these gain-related model inaccuracies.

3.6 Conclusions

Based on the results presented in this chapter, the following conclusions are drawn:

- The ink channel dynamics are modeled accurately for all the three models for non-jetting situations.
- For jetting situations, the ink channel dynamics are only accurately modeled with the wave model.
 - For jetting situations, inaccuracies are obtained with the Narrow-Gap model. For accurate modeling of the ink channel dynamics, the varying nozzle impedance has to be taken into account.

- For jetting situations, the same inaccuracies are obtained with the linear experimental model. The inaccuracies are caused by the ejection of a small volume of ink, introducing nonlinear behavior.
- The obtained inaccuracies with the experimental model concern mainly gain-related inaccuracies in the modeled time responses. The resonance frequencies are predicted accurately with the experimental model. Therefore, the overall oscillatory behavior is predicted very well.
- The first two resonance frequencies are dominating the ink channel dynamics. For ILC, it is crucial that both frequencies are predicted accurately, rather than the gain-related accuracy for jetting situations. For this reason it is chosen to use the experimental model for ILC synthesis. In Chapter 5 it will be demonstrated that ILC implemented on the actual system can handle the mentioned gain-related model inaccuracies.

Chapter 4

Control of an Inkjet Printhead

The main focuss of this chapter is on the design of a suitable reference trajectory. With using ILC for optimally tracking the designed reference trajectory, the defined control goal can be aimed for. According to the problem statement of Chapter 1, this control goal is defined as improving the drop consistency of an inkjet printhead. Although the main focuss of this research is on improving drop consistency, also attention is paid to jet stability and how reference trajectory design might improve jet stability.

This chapter is organized as follows. First, drop consistency and jet stability are further explained in Section 4.1. Next, the physical insights needed for the reference trajectory design are addressed in Section 4.2. It is explained how several operational issues which are encountered during jetting are related to drop consistency and jet stability. Before the reference trajectory design is addressed, first a short intermezzo is given in Section 4.3. This intermezzo concerns the working principle of ILC and it explains how ILC optimally tracks a defined reference trajectory. Based on the insights given in Section 4.2, the design of a reference trajectory is addressed in Section 4.4. For the implementation of ILC on the actual printhead, two different sensor functionalities are available. In combination with ILC, the channel pressure or the meniscus velocity can be controlled. Section 4.5 will discuss the advantages and disadvantages of using the mentioned sensor functionalities. In Section 4.6, both possibilities will be investigated on simulation level. Finally, the conclusions of this chapter are presented in the last section.

4.1 Control Goal

As explained, the control goal is defined as improving the drop consistency of an inkjet printhead. Drop consistency implies that each time a channel is actuated, the same drop properties are obtained. At present, the speed and volume of the ejected droplets varies as function of the jet frequency. This is shown in Fig. 4.1 where the measured droplet's speed and volume are depicted as function of the jet frequency for a standard actuation. In the figure, these variations are clearly visible. By varying the jet frequency from 10 up to 70 kHz, the droplet speed varies approximately between 5 and 11 m/s. The measured droplet volume is normalized between 0 and 1 and it can be seen that the same order in variations is obtained. Besides, the variations in speed and volume approximately acts in phase. These variations

as function of the jet frequency are highly undesirable since during a print job the jetting frequency continuously changes.

Though improving jet stability is not our primary control goal, it is considered in this chapter on theoretical level. Jet instability forms a significant problem in inkjet. Jet instability is the phenomenon where a nozzle stops jetting and causes unacceptable defects in a print, namely directly visible absence of lines. Previous research [Spr01] already showed that nozzle failure occurs mostly when an air bubble is entrapped into the nozzle. As a result, the channel acoustics are seriously disturbed and the channel stops jetting.

4.2 Operational issues revisited

For the design of a suited reference trajectory, physical insights are needed. In this section it is explained how several operational issues which are encountered during jetting are directly related to drop consistency and jet stability. Based on these insights, a suited reference trajectory can be designed. The issues that are revisited in this section are:

- Residual vibrations
- Air entrapment
- Nozzle refill
- Nozzle-plate wetting

The next subsections will discuss these issues and their relation to drop consistency and jet stability.

4.2.1 Residual Vibrations

After droplet ejection, the ink in a channel is not at rest immediately but it takes a certain time before the pressure waves are damped. This is known as the residual channel vibrations. Also the meniscus is vibrating after droplet ejection, i.e. the residual meniscus vibrations. Since the residual vibrations of the channel and meniscus are closely related to each other, this phenomenon is called residual vibrations in general. In Chapter 3 (e.g. Fig. 3.6) already simulation results were depicted, clearly showing the residual vibrations in the channel and meniscus. Based on this figure, it can be noted that when the residual channel vibrations come to a rest, eventually, also the meniscus comes to a rest.

As already mentioned, the residual vibrations typically are damped after 100 μ s. Consequently, for jet frequencies lower than ± 10 kHz sufficient time is available for the residual vibrations to damp out. However, higher jet frequencies are desired in order to increase the printhead productivity. As a result, the channel is actuated before these residual vibrations are damped out. Consequently, droplet formation starts from a disturbed situation and droplet consistency is not guaranteed. Note that both the situations in the channel and in the nozzle are disturbed compared to the nominal situation.

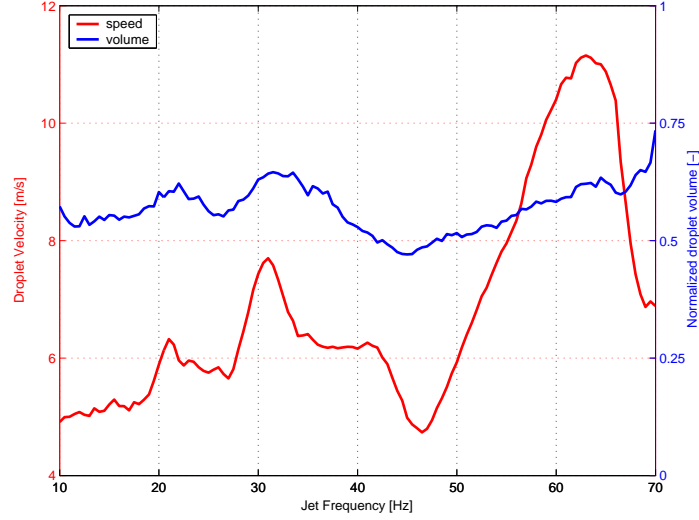


Figure 4.1: *Measured droplet speed and volume as function of the jet frequency for a standard trapezoidal pulse.*

As already addressed in Section 4.1, Fig. 4.1 shows that as a result of the residual vibrations, large variations in droplet properties (speed and volume) are obtained as function of the jet frequency. Such a figure is also called the DOD-curve (Drop-On-Demand). The location of the maxima of the DOD-speed curve can be explained by the fact that the residual vibrations are mainly dominated by the first acoustic mode (62 kHz according to the Narrow-Gap model). Consequently, the distance between two maxima in the residual vibrations is $\frac{1}{f_1} = 15.4 \mu\text{s}$. The maxima in the DOD-curves are thus located at 62, $\frac{62}{2}$, $\frac{62}{3}$ kHz etcetera.

The residual vibrations also have a disadvantageous effect on the jet stability. Due to the residual vibrations, large meniscus retractions can occur. In the next section will be explained in detail that with increasing meniscus retractions the chance on air entrapment also increases. Ultimately, this might result in nozzle failure.

4.2.2 Air Entrapment

Entrapment of air bubbles in the nozzle during jetting is the major cause of nozzle failure. Initially, these bubbles are not big enough to impair jetting. From this point, there exist two possible situations. (A), the bubble disappears after jetting one or a few droplets because the air bubble is dragged outside the nozzle with the ejected droplet. (B), if an air bubble is present in an acoustic field, it tends to grow due to the phenomenon rectified diffusion [Lei94]. When it is big enough it will prevent pressure to build up by the actuation and the channel stops jetting.

The movement of the meniscus is of crucial importance for air entrapment into the nozzle. More specifically: with large meniscus retractions, the chance on air entrapment into the nozzle is increased.

4.2.3 Nozzle Refill

After droplet ejection the nozzle has to be refilled with ink. This process is called nozzle refill. At short time scales ($< 50 \mu\text{s}$) this refill effect is mainly caused by the residual vibrations in the channel according to the nonlinear mass effect: the second positive pressure wave (the first one after droplet ejection) that hits the nozzle acts only on a small mass since the nozzle is nearly empty and the meniscus is accelerated outwards. Subsequently, the next negative pressure wave that hits the nozzle acts on a larger mass and the meniscus is less decelerated than accelerated. A sequence of positive and negative pressure waves (i.e. residual vibrations) will refill the nozzle. This is clarified in Fig. 4.2 where by making use of the wave model, the channel pressure and the meniscus position are depicted for one jet cycle. Note that in the figure meniscus positions larger than $0 \mu\text{m}$ mean that the meniscus is pushed outside the nozzle.

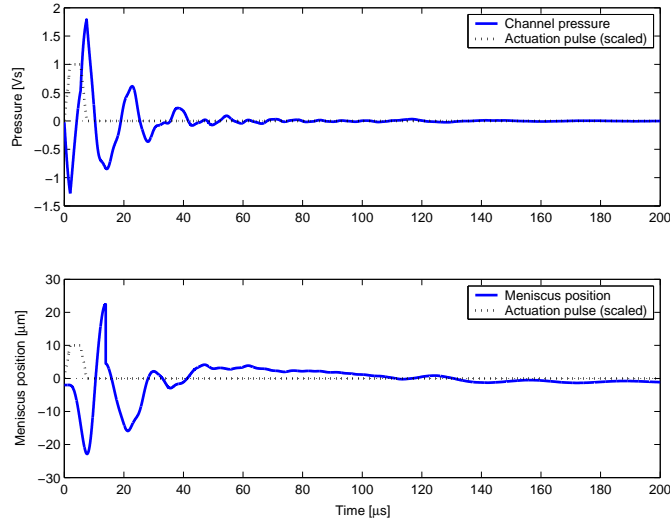


Figure 4.2: *Simulation with the wave model showing the nozzle refill after droplet ejection.*

When this meniscus position is evaluated it can be seen that after droplet ejection (modeled as a sudden jump in meniscus position) the meniscus is retracted in the nozzle. Next, the nozzle is refilled with ink as long as the acoustic pressure waves are present. When most of the pressure waves are damped out ($\pm 50 \mu\text{s}$) it can be seen that the refill mechanism resulted in an overfilled situation of the nozzle, i.e. due to excessive refill the ink is pushed out of the nozzle. This overfill situation might result in wetting of the nozzle plate. The phenomenon of wetting and its disadvantageous effect on drop formation and jet stability will be further explained in Section 4.2.4.

When the depicted meniscus position is evaluated for a larger time scale, it can be seen that the meniscus is slowly retracted again for $t > 50 \mu\text{s}$. Eventually, a certain equilibrium point slightly inside the nozzle is reached. The driving forces causing this retraction are on the one side the static negative pressure in the channel¹ and on the other side the capillaire forces.

¹As explained in Chapter 2, the static pressure inside the reservoir is negative in order to avoid the ink flowing out through the nozzle under influence of gravity.

The first always tries to retract the meniscus inwards the nozzle whereas the latter tries to move the meniscus surface to its equilibrium point inside the nozzle. Note that in the overfill situation as sketched in Fig. 4.2, both forces act in the same direction during the retraction. A simplified illustration of the meniscus in its equilibrium point and in an overfilled situation is given in Fig. 4.3 (a) and (b).

The overfill situation as sketched in Fig. 4.2 does affect the drop consistency negatively. Due to the slow transition from overfill ($t = 50 \mu s$) to an equilibrium ($t = \pm 200 \mu s$), the mass of ink inside the nozzle decreases. This means that if the jet frequency is increased from 5 kHz to 20 kHz, the mass of ink inside the nozzle before each actuation increases. With a larger mass of ink inside the nozzle, the resulting droplet speed and volume increases. Consequently, with increasing the jet frequency from 5 kHz to 20 kHz, the drop-speed and volume will also increase.

Refill does not influence the jet stability directly. However, indirectly it can influence the jet stability negatively. This is explained in the next section where as a result of excessive refill the phenomenon of wetting is discussed.

4.2.4 Nozzle-plate Wetting

As explained in the previous section, excessive refill of the nozzle will result in overfill. In an overfilled situation, the meniscus is pushed outside the nozzle as depicted in Fig. 4.3. Here, a simplified illustration is given of the shape of the meniscus for an overfilled situation and in its equilibrium point (plot (b) and (a) respectively).

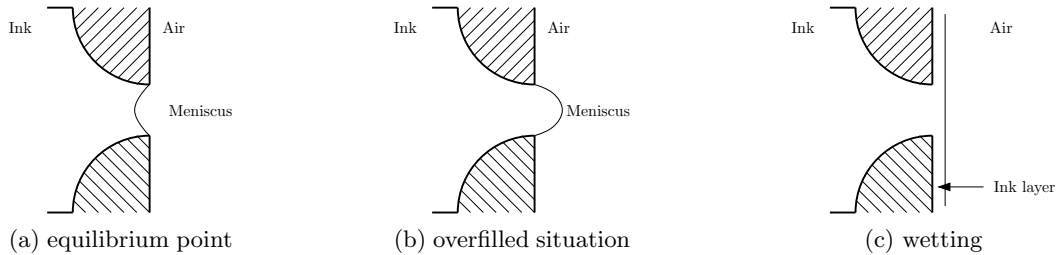


Figure 4.3: *Simplified illustration of the shape of the meniscus surface for its equilibrium point, an overfilled situation and for nozzle-plate wetting.*

Depending on various external circumstances, the overfill situation as depicted in (b) might result in wetting of the nozzle plate. With wetting, the lavishing ink of each actuation is caused to flow away and forms a thin layer of ink on the nozzle plate (c). In the beginning stadium of wetting, droplet properties are influenced by interference between the ink layer outside the nozzle plate and the meniscus. Moreover, when the ink layer has reached a critical thickness, air entrapment during a jet cycle might easily occur. Another disadvantage of wetting is that dirt particles captured in the ink layer can also disturb the jetting process, eventually resulting in air entrapment.

4.3 ILC working principle

In the previous section, several phenomena were addressed which are closely related to drop consistency and jet stability. Based on the physical insights given in that section one can argue that by choosing the right reference trajectory, e.g. a specific meniscus movement or a specific channel pressure, the control goal can be aimed for. Next, ILC can be used to optimize the actuation signal such that the desired reference trajectory is optimally tracked. Before the reference trajectory design is addressed, first the working principle of ILC is shortly discussed.

In this thesis, use is made of ILC in the lifted setting, see e.g. [Bos03]. In this 'lifted system' approach, the system behavior is described over a finite horizon by a static mapping from an input sequence to an output sequence, i.e the impulse response matrix J of the plant. The accompanying control structure is depicted in Fig. 4.4.

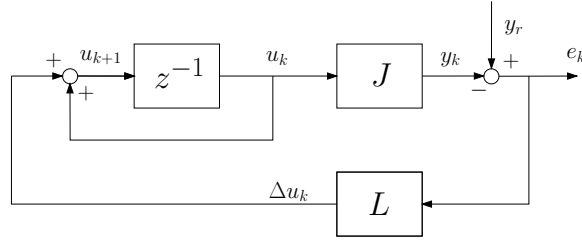


Figure 4.4: *Lifted ILC control structure in the trial domain.*

Let the input to the actuator be defined as u , the output y e.g. the meniscus velocity. The reference trajectory is defined as y_r and e is the error output. In the lifted setting, these signals are represented as vectors with length N for the k^{th} trial. This trial length N equals 1000 corresponding with a sample rate of 10 MHz and a time window of 100 μ s. The ILC learning matrix is represented by L . The one trial delay z^{-1} operator can be seen as a memory block. During the first trial k , the feedforward input u_k is applied to the plant J , resulting in output y , e.g. meniscus velocity. This first input u_1 can be e.g. the standard trapezoidal pulse. The error signal $e_k = y_r - y_k$, which equals the difference between the reference trajectory and the actual output of the plant, is determined. Based on this error, the learning controller L calculates an update Δu_k for the feedforward signal. This update is added to the previous input and forms the input u_{k+1} for the new trial $k + 1$. So the feedforward signal is iteratively adjusted such that the given reference trajectory is optimally tracked. For a detailed description of working principle of ILC and the controller synthesis, one is referred to e.g. [Nag06] or to the literature as described in Chapter 1.

4.4 Reference Trajectory Design Criteria

This section will discuss the design of the reference trajectory. The question arises how to choose a suitable reference trajectory to accomplish the defined control goal. The phenomena described in Section 4.2 form the key to a proper choice. The design of such a reference trajectory is explained with making use of the meniscus velocity. The movement of the meniscus can be directly related to the droplet formation process, according to [Dij84]. Therefore, instead

of focussing on the droplet properties, it is allowed to direct our attention to the meniscus velocity as reference trajectory. Besides, it is chosen to work with this meniscus velocity instead of the meniscus position, because the latter is discontinuous in time when a droplet is fired. It is assumed that the time-derivative of the position, the velocity, is a continuous signal, also during jetting. Continuity is a great advantage for identification and control, because a discontinuity implies a hard nonlinearity. For systems with hard nonlinearities, linear identification techniques such as a sine-sweep cannot be applied. Besides, control techniques for nonlinear systems exist, but are outside the scope of this research.

In Fig. 4.5, an example of a reference trajectory for the meniscus velocity is shown. This depicted reference trajectory is based on a standard trapezoidal actuation of the printhead. Note that it is chosen to use this standard actuation signal as starting-point to explain the design of the reference trajectory, so this choice is not unique.

By means of a parametrization of the depicted reference trajectory, it is explained how the droplet formation and the mentioned operational issues are related to the reference trajectory. In the figure, the parameters are denoted by numbers and will be explained next:

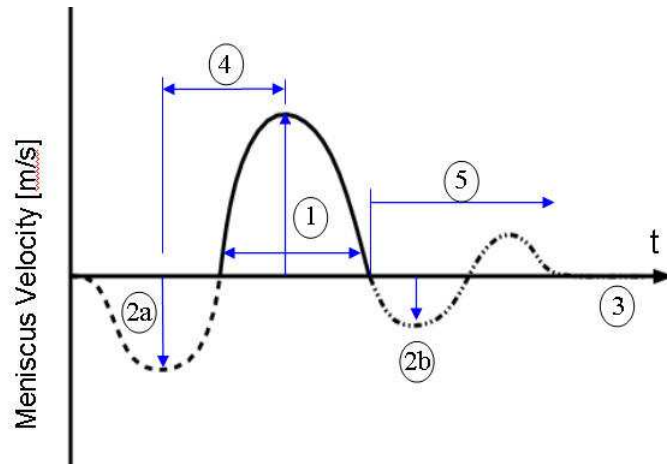


Figure 4.5: *Parametrization of the reference trajectory based on the meniscus velocity.*

1. Droplet formation

In Appendix B the Dijkman model is addressed. This mathematical model gives an approximation of the drop properties (speed and volume) based on the movements of the meniscus. By means of this model, the following statements can be made:

- It is assumed that only that part of the meniscus response where the velocity is positive (and large enough to result in a droplet) determines the properties of the resulting droplet. This positive velocity peak is denoted in the figure with 1. More specifically:
- The droplet's volume is determined both by the amplitude and the period of the positive meniscus velocity peak as depicted in Fig. 4.5 (also see (B.9), where the droplet's volume is calculated as the time-integrated meniscus velocity times the nozzle area).

- The droplet's speed is mainly determined by the amplitude of the positive meniscus velocity peak. Examination of the equation for the droplet's speed (B.13) namely shows that the expression is dominated by the square of the meniscus velocity.

So by varying the width and height of the peak, the droplet's speed and volume can be influenced. As explained, the depicted reference trajectory is based on a standard actuation signal. By leaving this peak unchanged, it is expected that the same droplet properties are obtained as with the standard actuation.

2. Meniscus retraction

As explained in Section 4.2, large meniscus retractions should be avoided in order to decrease the chance on air entrapment into the nozzle. In the figure it can be seen that the meniscus moves inwards twice. First as a result of the piezo actuation (2a), second directly after droplet ejection (2b).

- (a) The first meniscus retraction results from the fact that the printhead design is based on the so-called catapult effect for the ejection of droplets, i.e. traveling pressure waves. The amplitude of this retraction should be as small as possible, but unfortunately, it is strongly related to the amplitude of the succeeding positive peak. This is exactly what one should expect since further retracting "the catapult" gives an increase in positive velocity whereas the movement of the ink inside the nozzle can be seen as the movement of "the catapult" itself. Conversely, less retracting "the catapult" gives a decreased velocity. As a result, the amplitude of the first negative peak is a direct result of the chosen amplitude of the first positive peak as discussed under 1 where this should be taken into account.
- (b) Direct after droplet ejection, the outwards accelerated meniscus is retracting again due to the negative channel pressure after droplet ejection. This implies that by influencing the channel pressure at this point, the meniscus retraction can be decreased in order to avoid possible air entrapment. To what extent the meniscus retraction can be decreased with keeping the drop formation (1) undisturbed remains to be seen.

3. Damping the residual vibrations

In order to attenuate the variations in drop properties, the residual vibrations should be damped as quickly as possible after droplet ejection. Besides, by damping the residual vibrations extreme movements of the meniscus can be avoided so the chance on air entrapment can be decreased. Nevertheless, the following should be complied with:

- (a) The droplet formation should be left undisturbed.
- (b) Before the residual vibrations are damped, the nozzle should be refilled with ink since the residual vibrations are the main driving force for refill.

4. Time determined by channel geometry

The time between the first negative peak and the first positive peak is determined by the channel's geometry. More specifically, it represents the time needed for the negative pressure wave induced by the actuator to propagate towards the reservoir and back to underneath the middle of the piezo actuator. When exactly at this time instant the actuator is released to its initial position, the most efficient actuation is achieved. Consequently, given a certain geometry this time is fixed.

5. Nozzle refill

In the period that the residual vibrations are damped out, the nozzle should be refilled with ink and is therefore closely related to (3).

4.5 Piezo based ILC versus Meniscus Velocity based ILC

With using ILC, the designed reference trajectories can be optimally tracked. Since our aim is improving the drop consistency of an actual printhead, we are dependent on the available sensor functionalities. The different sensor functionalities were already explained in Chapter 2. Nevertheless, for control purposes the following information is available with the experimental setup:

- The droplet's speed and volume by a CCD camera.
- The meniscus velocity with a laser-vibro meter.
- The channel pressure by using the time-integrated piezo sensor signal.

With the implementation of ILC, continuous-time information is needed. Since the measurement of the droplet properties with the CCD camera is a discrete event, it cannot be deployed for this purpose.² However, both the piezo sensor and the laser-vibro meter are available for the implementation of ILC on an inkjet printhead. This is schematically represented in Fig. 4.6.

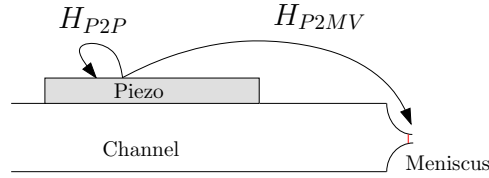


Figure 4.6: Available measurement utilities for the implementation of ILC on an inkjet printhead and their relevant dynamics.

As discussed in Chapter 2, the piezo sensor signal is in fact a measure of the derivative of the pressure in the channel. If the measured output is numerically integrated, the mean pressure below the piezo surface facing the channel is obtained. When this time-integrated piezo sensor signal is used as control variable for ILC, it will be denoted as Piezo based ILC (P-ILC). In case the laser-vibro meter is used as sensor utility, the meniscus velocity is obtained. Applying ILC in this setting is denoted as Meniscus Velocity based ILC (MV-ILC). Both MV-ILC and P-ILC will be addressed hereinafter:

Meniscus Velocity based ILC (MV-ILC)

As already stated in Section 4.4, the meniscus velocity is directly related to the droplet formation. Furthermore, when the meniscus velocity is controlled, one should be able to directly eliminate residual vibrations of the meniscus such that variations in droplet

²With hybrid control, a dynamic system can be controlled that exhibits both continuous and discrete dynamic behavior. However, this is outside the scope of this thesis.

properties can be attenuated. Moreover, large inwards movements of the meniscus can be measured (i.e. negative meniscus velocity) and can be taken into account by means of a suited reference trajectory design. A drawback is that based on the measured meniscus velocity no conclusions can be drawn about the corresponding meniscus position. Numerically integrating the velocity does not result in the correct meniscus position for the complete jet cycle due to the discontinuity in the position when a droplet is ejected. Therefore, with MV-ILC it is hard to control the refill of the nozzle. But altogether, using the meniscus velocity as control variable offers great opportunities to surmount most of the boundaries as addressed in Section 4.2.

Unfortunately, one big disadvantage of using the meniscus velocity as control output is encountered when MV-ILC has to be applied on the printhead in the experimental setup. In [WZBK06] it is explained that with using the laser-vibro meter only measurements can be performed for non-jetting situations. Consequently, ILC experiments can only be performed for non-jetting situations whereas we are interested in the jetting situation. However, in [WZBK06] the following approach was proposed in order to circumvent this problem. First, actuation pulses are designed that actively damp the residual meniscus vibrations for non-jetting situations. Next, the learned pulses are scaled to the jetting situation. Experiments showed that the scaled ILC pulse actively damped the residual vibrations after droplet ejection. Note, that this approach is preceded by assuming that the dynamics, i.e. H_{P2MV} behave linearly. However, in [WZBK06] also was illustrated that the nozzle dynamics behave nonlinear. Apparently, despite the fact that nonlinearities are present and the fact that ILC only can be performed for non-jetting situations, the drop consistency can be improved considerably by the application of MV-ILC. Nevertheless, it is expected that the limitation of the laser-vibro meter also limits the performance of MV-ILC, i.e. if the meniscus velocity could be measured accurately for jetting situations, it is expected that the performance can be even further improved.

Piezo based ILC (P-ILC)

With P-ILC the channel pressure is the controlled variable. However, the droplet formation and most of the mentioned operational issues takes place in the nozzle and the question might arise how suitable the piezo sensor is for controlling the drop formation process. Nevertheless, the channel acoustics are the driving force for movements of the meniscus. So by controlling the channel pressure, more or less the meniscus can be controlled indirectly. Unfortunately, certain dynamics are present between the channel pressure and the meniscus velocity so it remains to be seen to what extent this is correct. Despite this fact, it is assumed that the piezo sensor signal is representative for the jetting process and it forms a basis for the deployment of P-ILC in order to strive for the defined control goal.

Discussion

Based on this information, it can be concluded that both MV-ILC and P-ILC offers opportunities in order to improve drop consistency. However, choosing the meniscus velocity instead of the channel pressure as sensor signal seems a logical choice since the performance of an

inkjet printhead is mostly determined by the nozzle dynamics. Unfortunately, the suitability of MV-ILC for an inkjet printhead is surely limited since the laser-vibro meter can only be deployed for non-jetting situations. For this reason it is necessary to further investigate the possibilities of P-ILC. One should question if the piezo sensor is sufficient representative for the jetting process. Therefore, the following issue is investigated on simulation level. In order to improve drop consistency, both P-ILC and MV-ILC will be used in order to damp the residual vibrations after the ejection of a droplet. With the first strategy, the residual vibrations in the channel will be damped whereas with the latter the residual vibrations of the meniscus will be damped. For the simulations both the theoretical models are used, i.e. the Narrow-Gap and the wave model. Based on the simulation results it will be investigated what the fundamental differences are between the two approaches for damping the residual vibrations.

The results will be addressed in Section 4.6.1 and 4.6.2 respectively. The simulations are also used to explain the working principle of ILC using time weights. The introduction of time weights is necessary to make the reference trajectory design method as described in Section 4.4 possible. This is further elaborated in the next section.

4.6 Simulations

4.6.1 P-ILC versus MV-ILC using the Narrow-Gap model

In this section P-ILC will be compared to MV-ILC. The ILC simulations that are discussed in this section are performed on the Narrow-Gap model. Based on the frequency responses depicted in Fig. 3.3 and 3.4, two different ILC controllers are designed. Note that, in accordance with Chapter 3, for the implementation of ILC on the experimental setup, the measured frequency response is used for controller synthesis.

In Fig. 4.7, the simulated sensor signals resulting from a standard trapezoidal actuation at a jet frequency of 10 kHz are shown. The middle plot shows the time-integrated piezo sensor signal and the lower plot shows the meniscus velocity. In both signals, the residual vibrations after droplet ejection (around 15 μs) are clearly visible.

Now, these residual vibrations will be damped by using P-ILC and MV-ILC. As explained, the first will damp the residual channel vibrations and the latter the residual meniscus vibrations. Both strategies require a suitable reference trajectory. Since we are interested in damping the residual vibrations without disturbing the droplet formation, the approach as proposed in Section 4.4 is used. The resulting reference trajectories are also depicted in the figure (red dotted lines). Note that two different reference trajectories are depicted: one for P-ILC and one for MV-ILC. Besides, each reference trajectory consists of 2 parts. The first part equals the first positive peak of the regarding sensor signal and captures the droplet formation. The second part of the reference trajectory is the same for both sensor signals: for $t > 25 \mu\text{s}$ the residual vibrations have to be damped so there the reference trajectory equals zero. It can be observed that not for the complete trial length ($t = 0 \dots 100 \mu\text{s}$) the reference trajectory is defined. As explained, the goal is to damp the vibrations without disturbing the drop formation so we are not interested in prescribing the reference trajectory for the complete trial length. By doing so, the possibility is exploited that with the lifted ILC framework

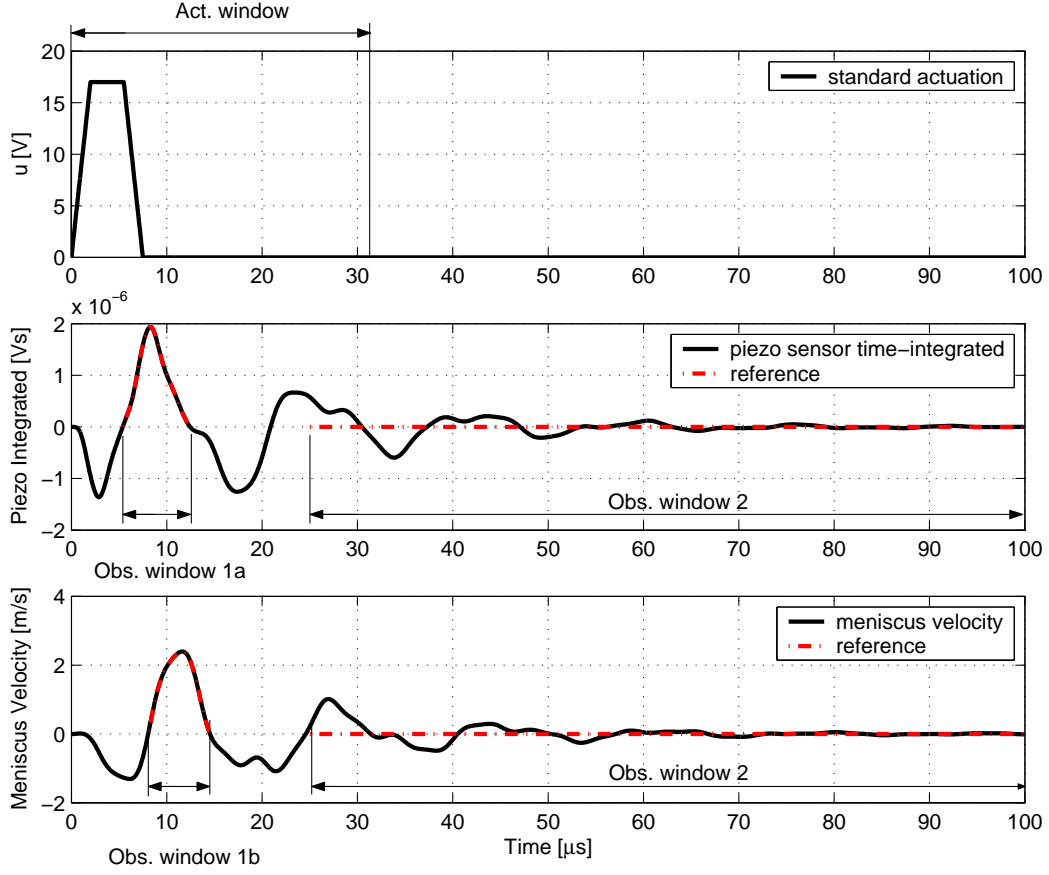


Figure 4.7: *Sensor signals resulting from a standard actuation using the Narrow-Gap model.*

the actuation and the observation windows can be selected individually [Dij03]. The chosen actuation and observation windows are also depicted in the figure. The observation windows are located where the reference trajectory is defined. Consequently, only the sensor signals within these observation windows are taken into account and as a result, only the defined reference trajectory within these observation windows is tracked by ILC. With applying these specific observation windows, ILC is allowed to act free in the time span where the actuator has to damp the residual vibrations, i.e. $t = 12 \dots 25 \mu\text{s}$ for P-ILC (middle plot) and $t = 15 \dots 25 \mu\text{s}$ for MV-ILC (lower plot). It must be noted that the observation windows are realized with the introduction of a weighting matrix. By doing so, each time point within the trial is weighted. During the simulations, the part of the trial which is observed is weighted with 1 and the part of the trial which is not observed with 0. More information about using time weights in ILC can be found in [vdWB06].

Also an actuation window is applied. It is chosen to have ILC act only on the first part of the trial ($t = 0 \dots 32 \mu\text{s}$). The P-ILC and MV-ILC simulation results are shown in Fig. 4.8. The results of MV-ILC are represented by the blue solid lines. The upper plot shows the learned ILC pulse which indeed only acts for the first $32 \mu\text{s}$. The pulse is optimized such that the reference for the meniscus velocity is tracked within the observation windows. The result-

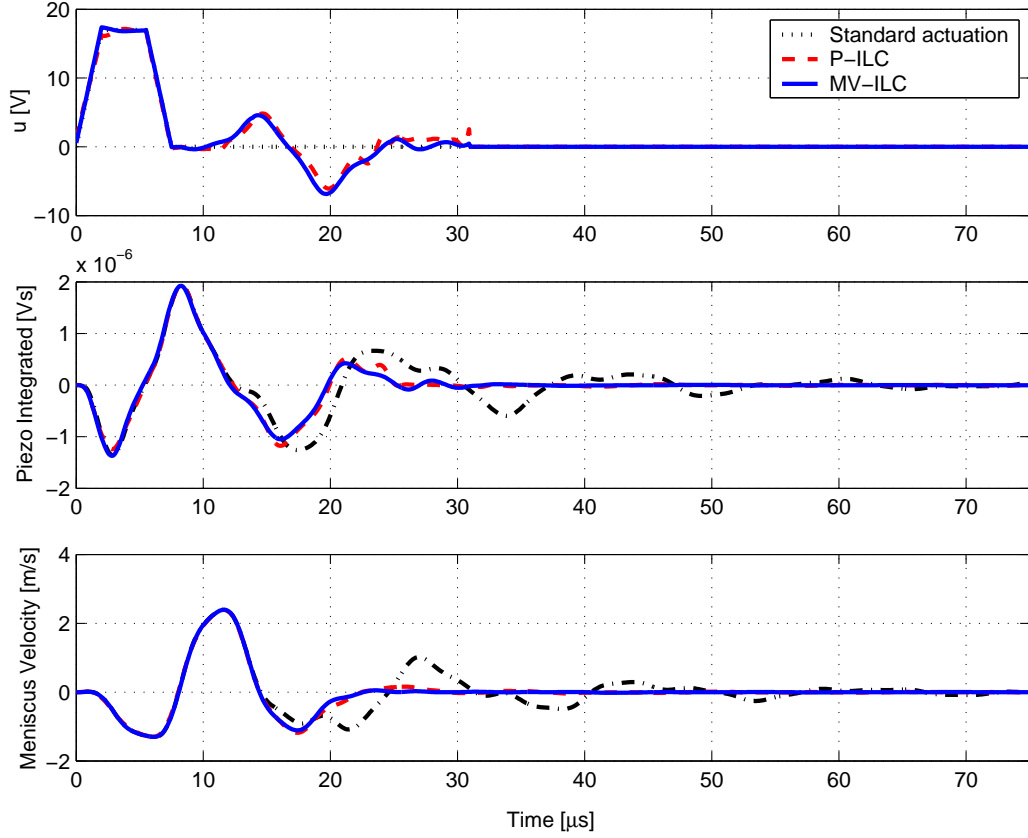


Figure 4.8: *Piezo based versus meniscus based ILC for the Narrow-Gap model.*

ing meniscus velocity upto the droplet ejection (around $15 \mu\text{s}$) is left unchanged, whereas for $t > 25 \mu\text{s}$ the residual meniscus vibrations are completely damped (lower plot). It can be noted that with damping the meniscus vibrations also the channel pressure is damped (middle plot).

The result of P-ILC are presented by the red dashed lines. Instead of the residual meniscus vibrations now the residual channel vibrations are damped. It can be seen that these results show strong similarities with the results of MV-ILC. More or less the same ILC pulse is obtained and in both situations the residual channel and meniscus vibrations are damped after approximately $t = 25 \mu\text{s}$. Based on these simulations performed on the Narrow-Gap model it can be concluded that:

- Approximately the same ILC pulses are obtained with using P-ILC and MV-ILC.
- That with active damping of the residual meniscus vibrations also the channel vibrations are damped.
- That with active damping of the residual channel vibrations also a considerably good damping of the meniscus is obtained.

However, according to Chapter 3, the Narrow-Gap model comprises a relative simple model of the nozzle. Therefore, one should be careful with drawing decisive conclusions from these

simulations about the MV-ILC versus P-ILC assessment. Therefore, the same simulations will be executed, but now performed on the wave model comprising a more accurate model of the nozzle dynamics.

4.6.2 P-ILC versus MV-ILC using the Wave model.

Just as in the previous section, P-ILC will be compared to MV-ILC but now the simulations are performed on the wave model, see Section 3.3. For the simulations, the same ILC controllers are used as discussed in the previous section. The results are shown in Fig. 4.9. Note that exactly the same actuation and observation windows are used.

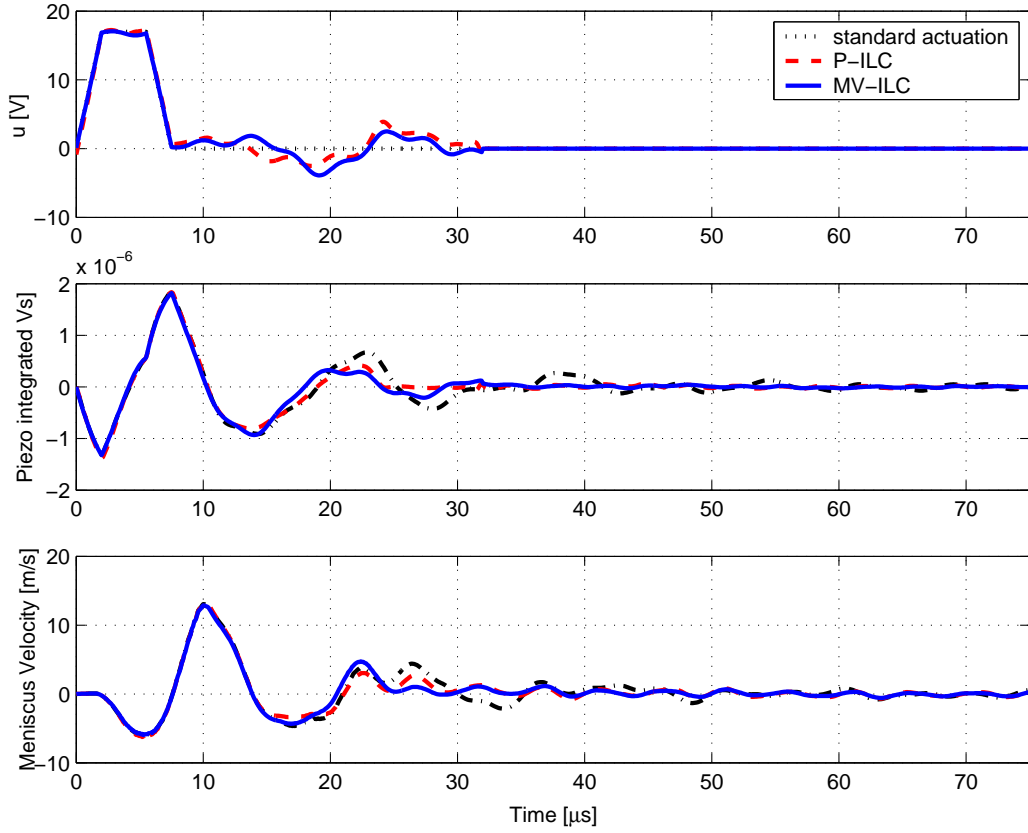


Figure 4.9: *Piezo based versus meniscus based ILC for the wave model.*

When the results of MV-ILC are evaluated (presented with blue solid lines) it can be seen that the actuation signal (upper plot) is adapted such that the residual meniscus vibrations are damped (lower plot). However, it can be noticed that the residual meniscus vibrations are not completely damped for $t > 25 \mu\text{s}$. It can be seen that still a small oscillation is present in this signal. Apparently, ILC is not capable of suppressing this remaining oscillation. When the FFT is calculated from the meniscus velocity signal for $t > 25 \mu\text{s}$, it can be seen that the remaining oscillations have a frequency around the frequency where the first destructive interference occur, i.e. 190 kHz. Apparently, oscillations of this frequency are present in the meniscus velocity signal, which can not be damped with the current piezo actuator. Simulations also showed that with decreasing the actuator length, this remaining oscillation can be

damped since the destructive interference is shifted towards a higher frequency.

The results of P-ILC are presented by the red dashed lines. The resulting ILC pulse which is optimized in order to damp the residual channel vibrations is somewhat different to the ILC pulse learned for damping the meniscus vibrations. The resulting piezo sensor signal is approximately zero for $t > 25 \mu s$ (middle plot). In contrast with the simulations performed on the Narrow-Gap model, now the residual meniscus vibrations are not completely damped with P-ILC. Based on the simulation results depicted in this figure the following conclusions are drawn:

- With deploying MV-ILC for active damping of the meniscus velocity, not all frequencies in this signal can be attenuated due to the phenomenon destructive interference.
- With damping the residual channel vibrations using P-ILC, the residual meniscus vibrations are this time not completely eliminated. This remaining oscillation is most likely the result of the following. With P-ILC the piezo sensor signal is forced to zero when damping of the residual vibrations is required. However, since the piezo sensor measures an average of the pressure underneath the piezo actuator, not necessarily the pressure in front of the nozzle equals zero. And in fact, the pressure in front of the nozzle is the driving force for movements of the meniscus.

4.6.3 Discussion

The following discussion will shortly revise the simulation results. The simulations were performed to investigate the usability of P-ILC for improving the drop consistency. It illustrated that with using P-ILC for damping the residual vibrations in the channel, also the residual meniscus vibrations were considerably good damped. Therefore, it is to be expected that with P-ILC a considerable increase in drop consistency can be achieved. Based on this finding, and according to Section 4.5, it is chosen to use the piezo sensor for the implementation of ILC on the actual printhead. The results hereof will be addressed in the next chapter.

4.7 Conclusions

Based on the results presented in this chapter, the following conclusions are drawn:

- The operation of the printhead is hampered by several operational issues. One of them, the residual vibrations, has a major contribution in limiting the drop consistency.
- Based on physical insights a reference trajectory is designed. In line with the defined problem statement of Chapter 1, it is illustrated that the defined control goal, improving drop consistency, can be translated into a suitable reference trajectory. Furthermore, for other issues such as jet stability, it is indicated how suitable reference trajectory design might help.
- Both the piezo sensor and the laser-vibro meter are available for the implementation of ILC on the actual printhead. Due to the limitations of the latter it was chosen to

further investigate the possibilities of using piezo based ILC for improving the drop consistency. Therefore, P-ILC and MV-ILC are compared on simulations level using both the theoretical models.

- The simulations illustrated that with damping the residual vibrations in the channel, also the residual vibrations of the meniscus are considerably damped. The fact that the meniscus is not completely damped with P-ILC is most likely the result of the following. Since with P-ILC in fact the average of the pressure underneath the piezo is controlled to zero, not necessarily the pressure in front of the nozzle equals zero. Consequently, the driving force for meniscus movements is not completely eliminated.
- Based on these conclusions, it is chosen to use the piezo sensor for implementation of ILC on the actual printhead. Nevertheless, it remains to be seen to what extent the variations in drop properties can be suppressed by means of piezo based ILC implemented on the actual printhead.

Chapter 5

Implementation of Iterative Learning Control

In this chapter, the implementation of ILC on an actual inkjet printhead is considered. The piezo sensor is used as control output. The control goal in this chapter is improving the drop consistency. To achieve this goal, two different approaches for the trajectory design are used. First, in Section 5.1 some practical considerations are addressed. Second, in Section 5.2 the ILC synthesis is discussed in short. Next, the experimental ILC results are addressed. Section 5.3 uses the reference trajectory design approach as used during earlier research. In Section 5.4 the approach as presented in Chapter 4 will be used for the reference trajectory design. In Section 5.5 the performance achieved with both approaches will be evaluated. Finally, in Section 5.6 the conclusions of this chapter are addressed.

5.1 Practical Considerations

In order to implement ILC successfully on the inkjet printhead, several practical issues have to be considered and are summarized below:

Signal Averaging

The measurement of the piezo signal is sensitive for disturbances and high-frequency noise. Therefore, for all experiments the piezo signal is averaged 128 times before it is used for processing.

Offset Correction

The measured piezo signal comprises a certain DC-offset which is introduced by several electrical components. Because the exact value of the offset is unknown and not constant, it is chosen to subtract the mean from the measured piezo signal.

Low-pass Filtering

In order to suppress high-frequency piezo behavior and measurement noise, the measured piezo signal is filtered by a low-pass filter. It concerns a digital 4th order Butterworth filter with a cut-off frequency of 400 kHz.

ILC Initial Conditions

According to [Bos03], ILC requires that each trial starts with the same zero initial conditions. Therefore, during learning experiments the jet frequency equals 1 kHz. By doing so, it is ensured that enough time is available for the system to become in rest.

5.2 Controller Synthesis

The controller synthesis is based on the experimental model obtained with the system identification as explained in Chapter 3. The resulting model represents the dynamics between the piezo actuator and the time-integrated piezo signal. In [Nag06] the ILC synthesis is addressed where ILC is applied on the theoretical Narrow-Gap model. For a detailed description of the ILC synthesis, one is referred to [Dij03] or [TvdMB01]. For this reason, the ILC synthesis will not be further addressed in this thesis. However, the following remark is noteworthy. According to Chapter 3, the experimental model is only accurate for non-jetting situations. For the jetting situation some inaccuracies are obtained since a certain nonlinearity is introduced due to the ejection of a droplet. Since ILC is deployed in the jetting situation, the question emerges if this model uncertainty hampers the convergence of ILC during the experiments. In the next section the experimental ILC results will be addressed. Also this convergence issue will be revised.

5.3 Piezo Based ILC

This section discusses the results of the implementation of ILC on the experimental setup with using the piezo as sensor. Two different approaches for the design of the reference trajectory will be discussed. First, the approach as used during previous research is applied, see [WBBK05]. This approach boils down to defining a reference trajectory for the complete trial length. Another possibility is to follow the approach as proposed in Section 4.4. By doing so, the reference trajectory is not defined for the complete trial length, but only for the relevant parts, i.e. the droplet formation and for the part where the ink channel has to be in rest. Then, by a suited choice of the observation intervals, only the reference trajectory within these intervals is tracked by ILC. This will be denoted as ILC using time weights. In this section, the first approach is followed for the reference trajectory design. In Section 5.4 the approach with using time weights is used.

In Fig. 5.1 the measured time-integrated piezo signal is shown resulting from a standard trapezoidal pulse. For the reference trajectory design, the approach as used in [WBBK05] is followed. The measured time-integrated sensor signal is taken as starting point for the construction of the reference trajectory. The first part upto the firing of a droplet is left unchanged (to 13 μ s). For the remainder in time, the pressure is forced to a rest by speeding up the damping. The pressure is not forced to a rest immediately but somehow gradually. This is done to avoid too high actuation voltages. The resulting reference trajectory is depicted in Fig. 5.1.

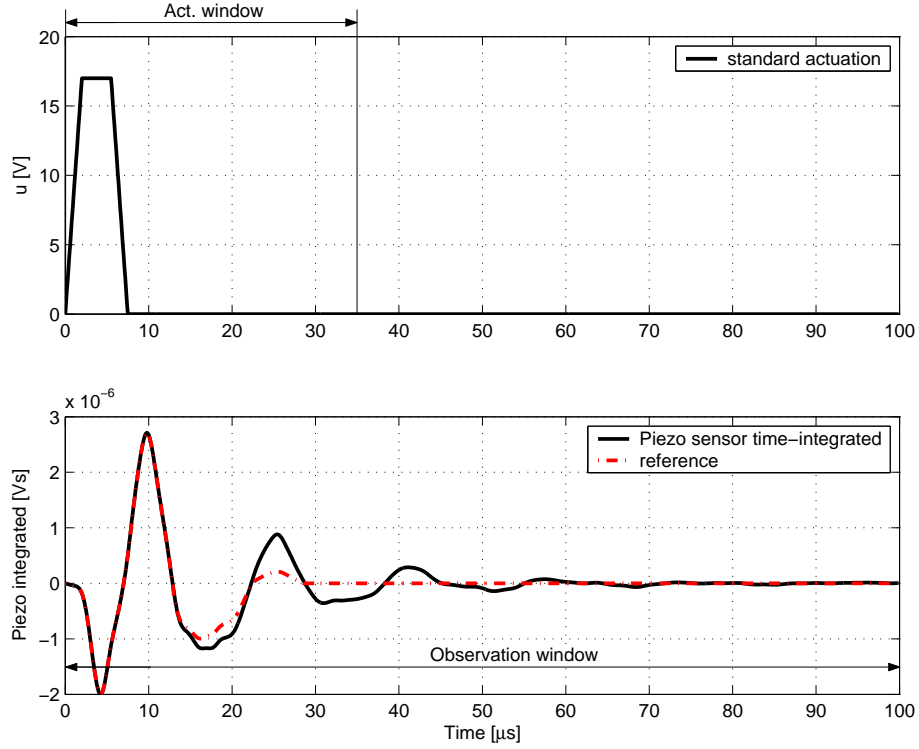


Figure 5.1: Measured time-integrated piezo sensor signal resulting from a standard actuation. The chosen actuation and observation windows and the reference trajectory are also depicted.

As explained in Section 4.6.1, the actuation and observation windows can be chosen individually. Since the reference trajectory is defined over the complete trial, the length of the observation window equals $100 \mu\text{s}$, i.e. the complete trial length. The length of the actuation window equals $35 \mu\text{s}$ so it is chosen to have ILC act only for the first part of the trial. Both windows are also depicted in Fig. 5.1.

The ILC results for trial 19 are depicted in Fig. 5.2. It can be seen that the learned ILC pulse successfully tracks the reference trajectory. The first part of the ILC pulse approximately resembles the standard trapezoidal pulse. This is not surprisingly since the first part of the reference trajectory is based on the response resulting from the trapezoidal pulse. After that, ILC adjusted the actuation signal such that the desired reference is tracked.

As error criterium, the integrated absolute error (IAE) is chosen:

$$IAE_k = \sum_{i=1}^N |e_k(i)| \quad (5.1)$$

The convergence based on the IAE is depicted in Fig. 5.3. It shows that ILC converged in approximately 20 iterations and that the error criterium is decreased by a factor 4. Based on Fig. 5.3 one more conclusion can be drawn. Despite the fact that the model used for ILC synthesis, as stated in Section 5.2, is only valid for non-jetting situations, no convergence problems occur. Apparently, ILC is robust against the occurring nonlinearities introduced by the ejection of a droplet (also see Section 3.4.3).

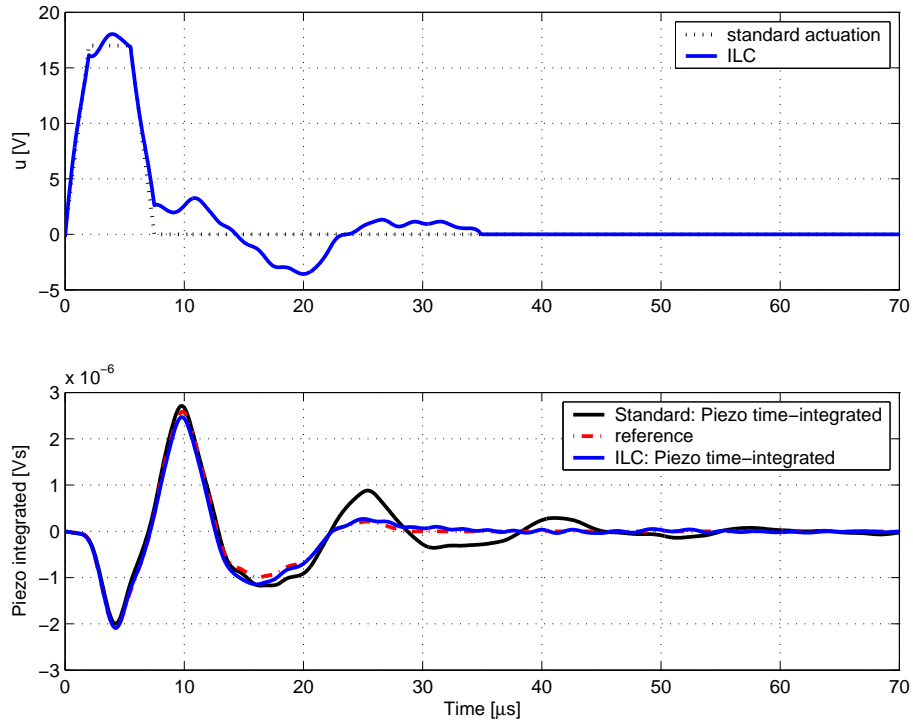


Figure 5.2: *ILC experimental results for trial 19 together with the response on a standard actuation signal.*

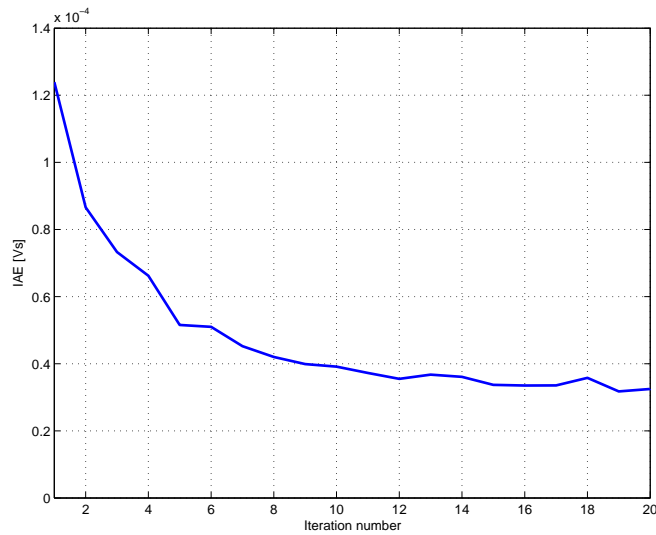


Figure 5.3: *Integrated absolute error of the error signal against the trial number.*

5.4 Piezo Based ILC using Time Weights

In the previous section the reference trajectory was defined for the complete trial length. In this section the approach as proposed in Section 4.4 is used for the reference trajectory design. The time-integrated sensor signal resulting from a trapezoidal pulse is again taken as starting point for the construction of the reference trajectory. First, it is chosen to leave the droplet formation undisturbed. Consequently, the first part upto the firing of a droplet is left unchanged (to $13 \mu\text{s}$). Second, in order to damp the residual vibrations, the second part of the reference trajectory is defined as zero for $t > 20 \mu\text{s}$. The resulting reference trajectory is depicted in Fig. 5.4. Note that for the remainder in time no reference trajectory is defined.

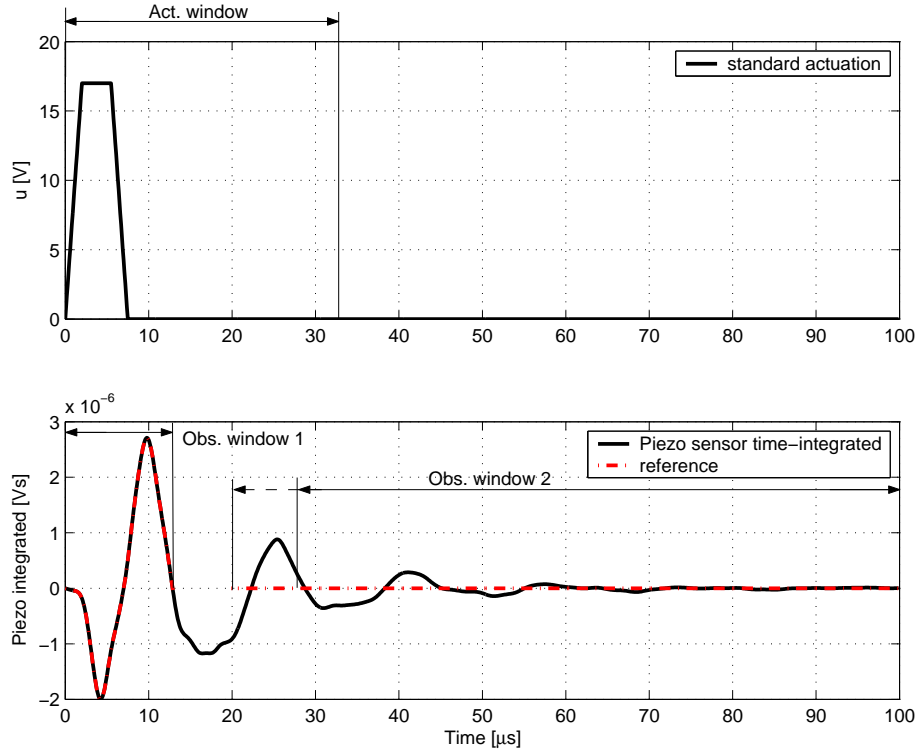


Figure 5.4: Measured time-integrated piezo sensor signal resulting from a standard actuation. The chosen actuation and observation windows and the reference trajectory are also depicted.

First will be investigated how quickly ILC can damp the residual vibrations after droplet ejection. Therefore, several experiments are performed. During the experiments, a fixed value for the actuation window is used, namely $30 \mu\text{s}$. However, the length of the observation windows will be varied such that the time available for damping the residual vibrations will be decreased from $27 \mu\text{s}$ to $20 \mu\text{s}$. The resulting actuation and observation windows are also depicted in Fig. 5.4. The first observation window is fixed and is located where the first part of the reference trajectory is defined. The starting point of the second observation window will be varied during different experiments from $t = 27 \mu\text{s}$ to $20 \mu\text{s}$. Note that the reference trajectory equals zero in the concerning time-span. Besides, as already introduced in Section 4.6, the observation windows are realized with weighting matrices. For the experiment presented in this section, both parts of the reference trajectory captured by the observation

windows are equally weighted. In other words, that part of the reference trajectory that is observed is weighted with 1, the remaining part of the trial is weighted with 0.

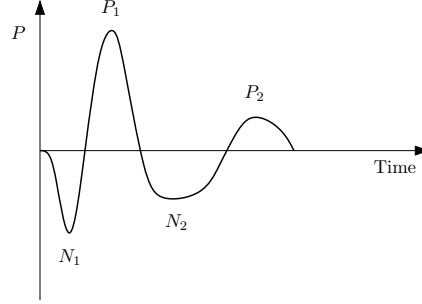
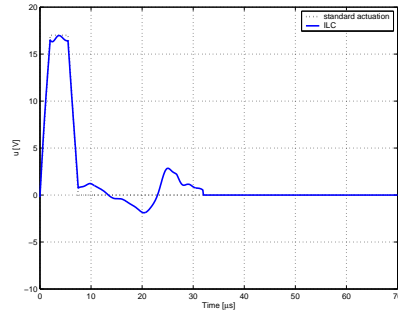


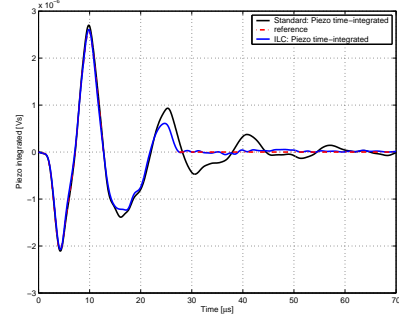
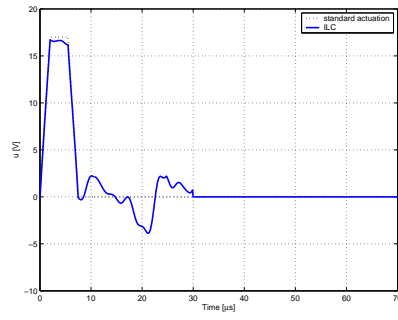
Figure 5.5: Schematic representation of the progress of the channel pressure together with the used denominations for the pressure peaks, i.e. P_1 , P_2 , N_1 and N_2 .

For explanation of the results, the denominations for the pressure peaks as depicted in Fig. 5.5 will be used. The experimental results are shown in Fig. 5.6. At the left side the learned ILC pulses are depicted and at the right side the corresponding sensor signals integrated in time. Based on this figure, the following can be noted:

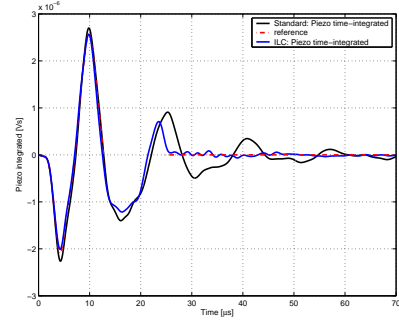
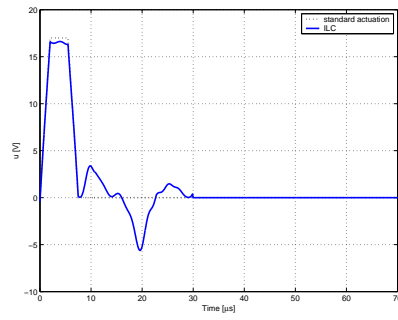
- It appears that with an available damping time of $27 \mu s$ the chosen actuation window is too short in order to damp the vibrations sufficiently. Therefore, for the first experiment the actuation window is increased from $30 \mu s$ to $32 \mu s$ (plot *a* and *b*).
- By decreasing the time available for damping the residual vibrations, the second positive pressure peak, i.e. P_2 is more and more suppressed. When the corresponding ILC actuations are observed more closely, it can be noticed that the negative actuation peak located at $t = 20 \mu s$ increases from approximately $-2V$ to $-6V$ to accomplish this.
- If the available damping time is shorter than $25 \mu s$, the residual vibrations cannot completely be eliminated anymore. These remaining oscillations in the piezo signal are clearly visible in plot *f* and *h*. Based on these findings, damping the residual vibrations for $t > 25 \mu s$ seems a proper choice.
- FFT calculations demonstrated that with decreasing the time available for damping, more high frequent information can be found in the remaining oscillations of the piezo sensor signal. These remaining high frequent oscillations are clearly visible in plot *f* and *h*. The results of the FFT calculations are presented in Fig. 5.7. In this plot, the frequency spectra of these remaining oscillations are depicted. All the FFT calculations are performed for $t > 30 \mu s$. In the left plot, the frequency spectra of the signals resulting from a standard actuation and from the four discussed ILC actuations are depicted. It can be noted that for the standard actuation, the remaining oscillations are dominated by the first two resonance modes, i.e. 62 and 130 kHz. Moreover, with the ILC actuations these frequencies are strongly suppressed. In the right plot is zoomed into the frequency spectra of the signals depicted in the left plot, resulting from the four ILC actuations. It can be observed that with decreasing the time available for damping, the first two resonance frequencies are less suppressed. Moreover, with speeding up the



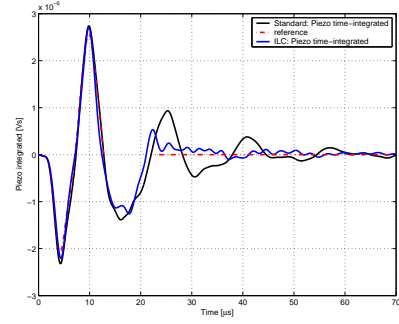
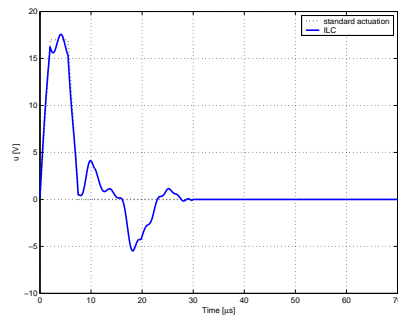
(a) ILC pulse

(b) damping for $t > 27 \mu s$ 

(c) ILC pulse

(d) damping for $t > 25 \mu s$ 

(e) ILC pulse

(f) damping for $t > 23 \mu s$ 

(g) ILC pulse

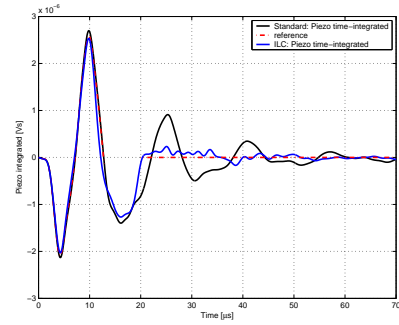
(h) damping for $t > 20 \mu s$

Figure 5.6: Varying the time instant for damping of the residual vibrations.

damping, frequencies around 300 a 350 kHz can be found in the figure. Apparently, these higher order channel dynamics are more excited due to the higher control activity needed for the faster damping of the residual vibrations.

- By decreasing the available damping time, the second positive pressure peak P_2 is more and more damped. However, the second negative pressure peak N_2 is almost left unchanged by ILC despite the fact that this part is not captured by an observation window. This seems rather striking because with speeding up the damping it is expected that this goes together with damping N_2 also. Apparently, it is conflicting with the response captured by the first observation window and it is for the system not realizable to damp N_2 without disturbing P_1 . This is clarified by Fig. 5.8 where is zoomed into the first 30 μs of plot h. It shows that, given the used time weights, too fast damping of the residual vibrations is affecting the first positive peak, i.e. the droplet formation will be disturbed.

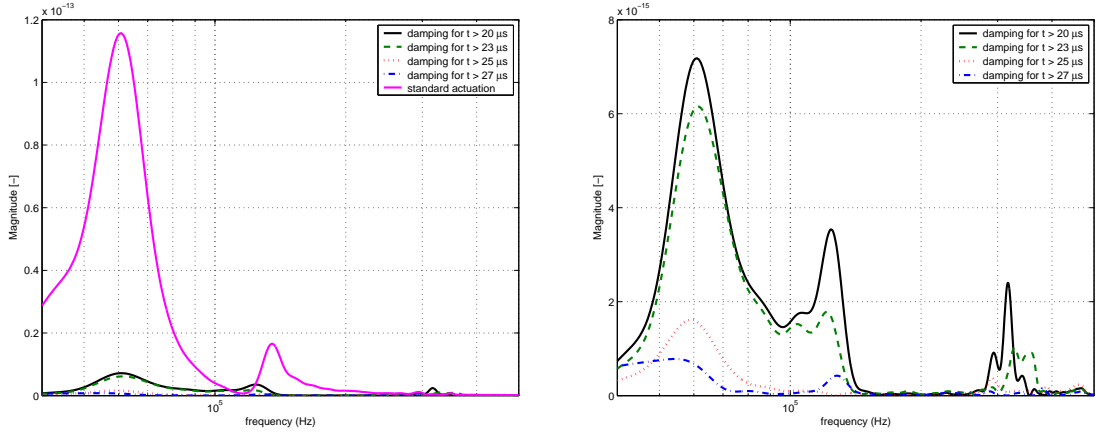


Figure 5.7: Frequency spectrum of the remaining oscillations resulting from a standard actuation and for the four different ILC actuations presented in Fig. 5.6. In the right plot is zoomed into the signals corresponding to the ILC actuations.

Based on these findings, the following ILC experiment is performed with using an actuation window of 32 μs and with damping the vibrations for $t > 25 \mu\text{s}$. The results are shown in Fig. 5.9 and it can be seen that the residual vibrations are considerably good damped while leaving the first part (upto 13 μs) undisturbed. It must be noted that the first trial was started with zero input whereas during the previous experiments was started with the trapezoidal pulse. Since the first part of the reference signal is based on the trapezoidal pulse, it is not surprising that ILC approximately resembles this pulse. However, the sharp edges of the trapezoidal pulse are rounded since was started with zero input.

The learned ILC pulses from this section and Section 5.3 and the resulting responses are depicted once more in Fig. 5.10. Based on this figure it can be concluded that with using time weights a faster damping of the residual vibrations is achieved: with using time weights the vibrations are approximately damped in 25 μs and without using time weights in approximately 29 μs . Moreover, since the residual vibrations are earlier in a rest, the length of the actuation could be decreased from 35 μs to 32 μs .

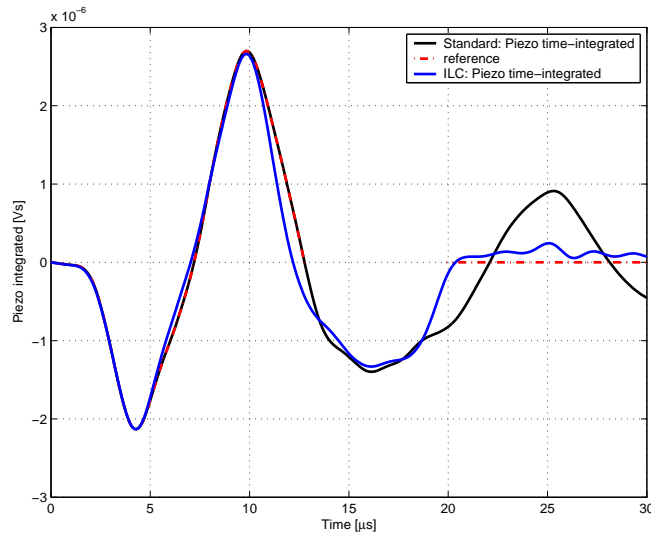


Figure 5.8: *ILC experimental results illustrating that too fast damping the residual vibrations disturbs the drop formation.*

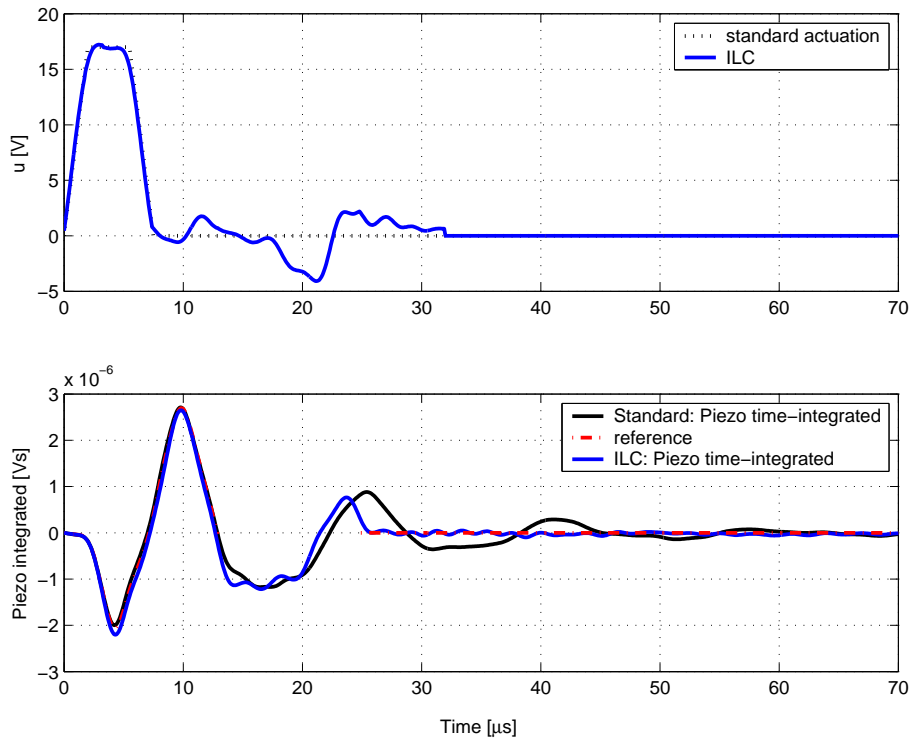


Figure 5.9: *ILC experimental results without ILC and with ILC using time weights for trial 15.*

Finally, it can be noted that the resulting ILC pulses are too complex to implement on the Application Specific Integrated Circuit (ASIC) of a printhead. In order to circumvent this practical implementation issue, in [WBSK06] a modified ILC algorithm is presented that

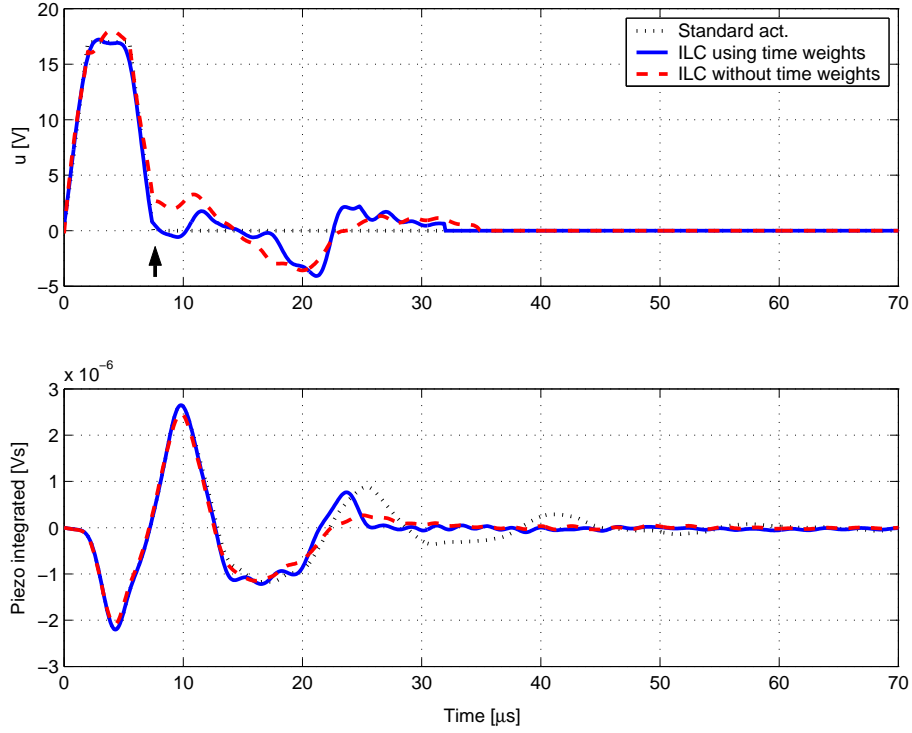


Figure 5.10: Comparison of the ILC experimental results with and without using time weights.

allows for the design of pulses with predefined complexity. The implementation of such an algorithm on an inkjet printhead will be addressed in Appendix E. Furthermore, the robustness of the learned ILC pulse against production tolerances will be investigated.

5.5 Performance Evaluation

In this section, the influence of the learned actuation signals on drop consistency will be evaluated. To illustrate the positive effect of damping the residual vibrations on the drop consistency, the measured DOD-speed and DOD-volume curves using the learned ILC pulses are depicted in Fig. 5.11 and 5.12. For this experiment, the jet frequency is varied in a range from 10 kHz upto 70 kHz. This means that the time-period available for the higher jet frequencies is smaller than the length of the ILC actuation ($32 \mu\text{s}$ and $35 \mu\text{s}$). Consequently, jet frequencies can be applied upto 31.3 kHz and 28.6 kHz respectively. However, these jet frequencies are too low in order to meet the demands in terms of print productivity. To circumvent this problem, use is made of the assumption that the concerning dynamics (from piezo input to piezo sensor signal) behave linear. According to the superposition principle, it is allowed to sum the overlapping ILC pulses for jet frequencies higher than 31.3 kHz and 28.6 kHz respectively.

Evaluating the results depicted in Fig. 5.11 and 5.12, it can be seen that with both ILC pulses the variations in droplet speed and volume are strongly reduced. When the speed and volume

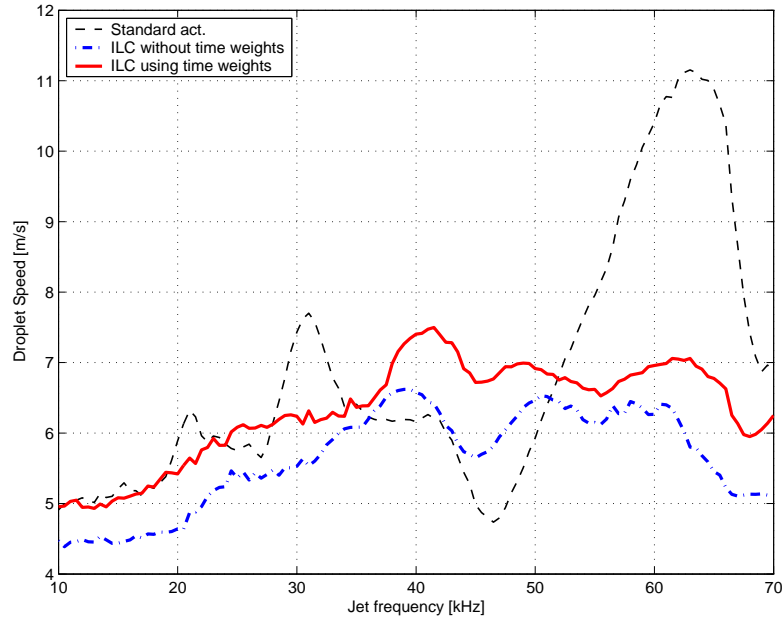


Figure 5.11: Measured DOD-speed for a standard actuation, ILC without using time weights and ILC with using time weights.

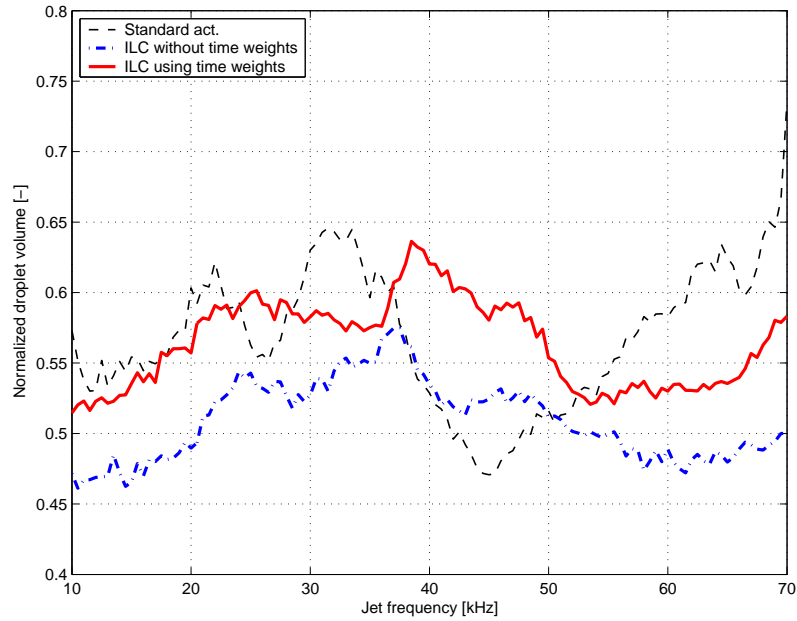


Figure 5.12: Measured DOD-volume for a standard actuation, ILC without using time weights and ILC with using time weights.

curves resulting from the ILC actuation using time weights are looked more closely (red solid lines), the following can be noted. In the first place, approximately the same drop properties are obtained as with the standard actuation (for low jet frequencies), i.e. the droplet formation is not disturbed. In the second place, the residual channel vibrations are damped in

approximately $25 \mu\text{s}$ (see Fig. 5.4). This means that, even with active control, the channel is not in a rest for jet frequencies higher than 40 kHz. Not surprisingly, the variations for jet frequencies higher than 40 kHz are not completely eliminated according to Fig. 5.11 and 5.12. However, for jet frequencies lower than 40 kHz it can be seen that the variations in speed and volume are eliminated to a large extent. Unfortunately, both the speed- and volume-curve show a strong positive trend for the frequency range from 10 to 25 kHz. Note that with use of the other two actuations the same positive trend can be found for this frequency range. So for jet frequencies upto 40 kHz, it can be concluded that the drop variations are strongly suppressed by damping the residual vibrations in the channel, but the consistency in drop properties still suffers from this positive trend.

Before explaining the cause of this positive trend, first it is demonstrated to what extent the drop variations are attenuated with leaving this positive trend out of consideration. This is done by expressing the variations in drop-speed and -volume in terms of the standard deviation. However, first the linear positive trend is removed from the measured data. Subsequently, the standard deviation is calculated. It can be concluded that for the jet frequency range from 10 upto 40 kHz the variations in drop-speed and -volume have been reduced by 66% and 48%, respectively. Apparently, by damping the residual vibrations in the channel, also the residual vibrations of the meniscus are mostly damped. Note that this is in accordance with the predictions based on the simulation results presented in Chapter 4.

When the speed and volume curves resulting from the ILC actuation learned without time weights are looked more closely (blue dashed lines), it can be noted that lower drop speed and smaller drop volumes are obtained. This can be explained by taking a closer look to the learned pulse as depicted in Fig. 5.10 (red dashed line). The important difference with the ILC actuation using time weights can be found at $t = 8 \mu\text{s}$, indicated with the arrow. It can be seen that the actuation voltage is not completely returned to zero. As a result, the retracted piezo (due to the positive flank) is not completely returned to its initial position. Consequently, the positive pressure wave traveling towards the nozzle is less amplified. The slightly reduced amplitude of the first positive pressure peak is also visible in the piezo signal depicted in Fig. 5.10. The reason for ILC to adapt the concerning part of the actuation is a result of the designed reference trajectory as depicted in Fig. 5.1. It shows that the reference trajectory already imposes damping of the second negative pressure peak. Apparently, by requiring damping of the residual vibrations too close to the droplet formation, it cannot be realized without leaving the first positive peak, i.e. the drop formation, undisturbed. Note that this can be resolved by leaving the second negative pressure peak undisturbed with the reference trajectory design.

As explained, the drop consistency still suffers from the positive trend for the lower jet frequencies. In Chapter 4 already was addressed that nozzle overfill, and its possible result wetting, can influence the drop properties negatively. Based on simulations performed with the wave model, it was demonstrated that as a result of the overfilled nozzle, both the drop speed and volume increases when the jet frequency increases from 5 to 20 kHz. Besides, it was explained that it was expected that wetting of the nozzle-plate decreases the droplet speed but leaves the droplet volume more or less undisturbed. Since the time available for forming an ink layer on the nozzle-plate is larger for low jet frequencies, it is expected that

with increasing the jet frequency, the influence of wetting decreases. Based on this knowledge, both lines of reasoning (overflow and wetting) can be used to explain the positive trend in drop speed and volume.

Unfortunately, the meniscus position cannot be measured during a jet cycle. Consequently, it is not possible to assess whether this overflow situation indeed occurs. However, the possibility exists to get a measure for the wetting of the nozzle-plate. For this reason, another experiment is performed in order to investigate whether the operation of the printhead indeed is hampered by wetting of the nozzle-plate.

During the following experiment, the nozzle-plate is treated such that poor wetting conditions are achieved. As a result, it is avoided that the ink of the (possible) overflowed nozzle will flow out over the nozzle-plate. Before and after the anti-wetting treatment, the drop properties are once more measured as function of the jet frequency. The results are shown in Fig. 5.13 for using the standard trapezoidal pulse and the ILC actuation as discussed in Section 5.4.

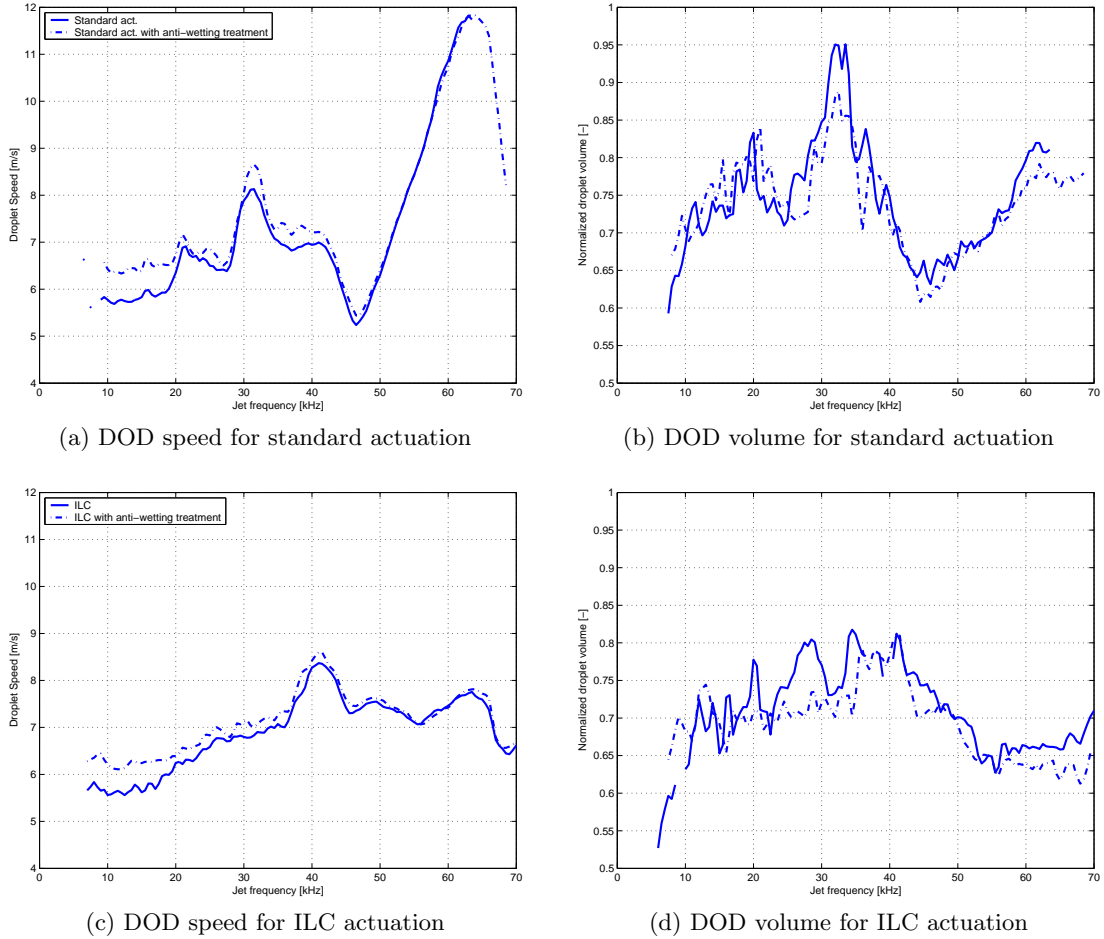


Figure 5.13: *Influence of an anti-wetting treatment of the nozzle-plate on the DOD performance.*

At the left side of Fig. 5.13, the measured drop speed is depicted and at the right side the drop volume. The measurements clearly demonstrate that before the anti-wetting treatment, wetting of the nozzle-plate occurs. After the treatment, when wetting of the nozzle-plate is avoided, the drop speed is indeed considerably increased for the lower jet frequencies. As expected, for higher jet frequencies the drop speed is barely influenced. Moreover, it can be seen that the drop volume is hardly influenced by wetting of the nozzle-plate.

Based on the results presented in Fig. 5.13, the following conclusions can be drawn:

- Both actuations (standard and ILC) results in wetting of the nozzle-plate. Therefore, with both actuations excessive nozzle refill occurs.
- The remaining (small) positive trend for the lower jet frequencies in drop properties after the anti-wetting treatment (dashed lines in Fig. 5.13) can be explained by the overfilled nozzle in accordance with Section 4.2.3.
- In order to improve the consistency in drop properties it is necessary to further investigate the refill of the nozzle.

In order to evaluate the influence of ILC on the drop consistency it was possible to simply measure the drop properties. Unfortunately, it is difficult to pronounce judgment about jet stability. Jet stability tests comprises experiments where billions of droplets are ejected under different conditions, like e.g. varying jet frequencies and actuation voltages. For this reason, the influence of the learned ILC actuation on the jet stability is not investigated during this research.

5.6 Conclusions

Based on the results presented in this chapter, the following conclusions are drawn:

- It was demonstrated that the experimental model is accurate enough for ILC. Furthermore, ILC appears to be robust against (small) nonlinearities introduced with the ejection of a droplet.
- With the introduction of time weights, only the relevant part of the sensor signal is observed. Experiments showed that the residual vibrations could be damped in a shorter time-span than in the case without using time weights.
- With too fast damping of the residual channel vibrations, the droplet formation process is disturbed and the residual vibrations are not completely eliminated anymore. Moreover, as a result of the higher control activity needed to accomplish this, higher order channel dynamics are excited.
- Eventually, it was chosen to damp the residual channel vibrations within $25 \mu\text{s}$ using an actuation window of $32 \mu\text{s}$.
- Drop-speed and -volume variations as function of the jet frequency expressed in terms of the standard deviation have been reduced by 66% and 48% respectively for jet frequencies upto 40 kHz. Consequently, the drop consistency is considerably improved.

- Based on the fact that the variations in drop properties are largely attenuated, it can be concluded that with damping the residual vibrations in the channel, also the residual vibrations of the meniscus are mostly damped for jet frequencies lower than 40 kHz.
- Despite the fact that the variations in drop-speed and -volume are largely attenuated, the drop consistency still suffers from a positive trend both in speed and volume for the lower jet frequency range. Experiments demonstrated that this trend was caused by nozzle overfill and its result, wetting of the nozzle-plate.
- The designed reference trajectory, and consequently the learned ILC actuation, does not take the nozzle overfill situation sufficiently into account. If this excessive refill can be prevented for, nozzle overfill and wetting of the nozzle-plate can be avoided and drop consistency and jet stability can be (further) improved.
- The influence of the learned ILC actuation on the jet stability is not investigated on the experimental setup.

Chapter 6

Conclusions and Recommendations

In this chapter, conclusions of this research are summarized. Moreover, several recommendations for future research are given.

6.1 Conclusions

In this thesis two existing theoretical models and one experimental model are addressed. The ink channel dynamics are modeled accurately for all the three models for non-jetting situations. For the jetting situation, the following conclusions are drawn:

- The ink channel dynamics are accurately modeled with the wave model for jetting situations.
- For jetting situations, inaccuracies are obtained with the Narrow-Gap model. For accurate modeling of the ink channel dynamics, the varying nozzle impedance has to be taken into account.
- For jetting situations, the same inaccuracies are obtained with the linear experimental model. The inaccuracies are caused by the ejection of a small volume of ink, introducing nonlinear behavior. This nonlinear effect is large enough to significantly affect the nozzle impedance such that the ink channel dynamics are influenced.

The obtained inaccuracies with the experimental model concern mainly gain-related inaccuracies in the modeled time responses. The resonance frequencies are predicted accurately with the experimental model. For ILC, it is crucial that these frequencies are predicted accurately, rather than the gain-related accuracy for jetting situations. For this reason it is chosen to use the experimental model for ILC synthesis.

The control goal is defined as improving the drop consistency of an inkjet printhead. Based on physical insights, it is demonstrated that this goal can be translated into the design of a suitable reference trajectory. Besides, on theoretical level it is explained how the design of a suitable reference trajectory might improve other operational issues such as jet stability.

For the implementation of ILC on the actual printhead two different sensor functionalities are available, i.e. the piezo sensor and the laser-vibro meter. Due to the measurements limitation of the latter it is chosen to use the piezo sensor. Simulations demonstrated that with damping the residual vibrations in the channel using piezo based ILC, also the residual vibrations of the meniscus are considerably damped. The fact that the meniscus is not completely damped is most likely the result of the following. Since with piezo based ILC in fact the average of the pressure underneath the piezo is controlled to zero, not necessarily the pressure in front of the nozzle equals zero. Consequently, the driving force for meniscus movements is not completely eliminated.

With using ILC without time weights, the reference trajectory is defined for the complete trial length. With using time weights, the reference trajectory is only defined for the relevant parts. It was demonstrated that with both strategies the residual vibrations in the channel are damped considerably good. However, with the introduction of time weights, a faster damping of the residual vibrations is obtained.

Drop-speed and -volume variations expressed in terms of the standard deviation that occur during the operation of an inkjet printhead have been reduced by 66% and 48% respectively for jet frequencies upto 40 kHz. Consequently, the drop consistency is considerably improved. Based on this finding it can be concluded that with damping the residual vibrations in the channel, the residual vibrations of the meniscus are mostly damped.

Despite the fact that variations in drop-speed and volume are largely eliminated, drop consistency still suffers from a positive trend in both speed and volume for the lower jet frequency range. Experiments demonstrated that this trend is caused by overfill of the nozzle and its result, wetting of the nozzle-plate. Apparently, the learned ILC actuation does not take this excessive nozzle refill sufficiently into account.

6.2 Recommendations

First of all, additional tuning of the several ILC parameters like time windows and time weights might further improve performance. Besides, it is desirable to investigate the influence of the ILC actuation on jet stability. Moreover, for experiments at high jet frequencies it may be desirable to learn the input signal for a sequence of droplets instead of applying summations of overlapping input signals.

Although the variations in drop properties are strongly suppressed, drop consistency still suffers from the positive trend. Therefore, further investigation of the excessive refill of the nozzle is desired. It should be investigated whether the refill can be influenced by means of piezo based ILC. Moreover, usage of nozzle-plates with poor wetting conditions improves drop consistency and might also improve jet stability since wetting of the nozzle-plate is avoided.

Finally, it may be desirable to further investigate the possibilities for different sensor functionalities which give a better measure for the droplet formation process. For example, a sensor integrated in the nozzle might offer great opportunities to improve drop consistency and jet stability. By means of dual objective ILC, the piezo can still be used as sensor in such a case. Moreover, another possibility is splitting the piezo unit in two or more pieces. Consequently, the number of actuators and sensors per ink channel can be increased. By doing so, a better

measure of the ink channel dynamics is possible. Besides, it offers new opportunities for actuation of the channel on the one hand and to damp the residual vibrations on the other hand.

Appendix A

Narrow Gap Model

Narrow-Gap theory

The channel and the nozzle are divided in several segments. Each segment can have different properties like cross-sectional area and flexibility of the channel wall. The acoustic model is based on the narrow-gap equation (A.1) which describes the pressure inside the channel and is expressed in frequency domain:

$$B_k \frac{\partial^2}{\partial x^2} p + \frac{\omega^2}{c_0^2} = -\rho_0 \omega^2 \frac{\Delta A_k}{A_{0k}} \quad (\text{A.1})$$

Here, B_k is a function describing the effect of viscosity on the channel geometry. p denotes the channel pressure, x indicates the coordinate along the channel length. Furthermore, c_0 denotes the speed of sound for ink, ω the angular frequency, ρ_0 the average density of ink and ΔA the area change of the nominal cross-section area A_0 . The narrow-gap equation describes the pressure waves in a channel with flexible walls traveling with the speed of sound in the frequency domain. These pressure waves are induced by the piezo actuator. The actuation term ΔA on the right side (A.1) can be written as:

$$\frac{\Delta A_k}{A_{0k}} = \alpha V + \beta p \quad (\text{A.2})$$

The cross-sectional area change is caused by elastic forces deforming the channel. This deformation is caused by:

- Deformation by piezo voltage
- Deformation by pressure inside the channel

The parameters α and β are determined with use of the FEM package ANSYS. By modeling an array of channels in ANSYS, the influence of pressure waves in neighboring channels and the influence of actuation for neighboring channels can be computed and crosstalk effects can be taken into account:

$$\frac{\Delta A_k}{A_{0k}} = [\alpha] \underline{V} + [\beta] \underline{p} \quad (\text{A.3})$$

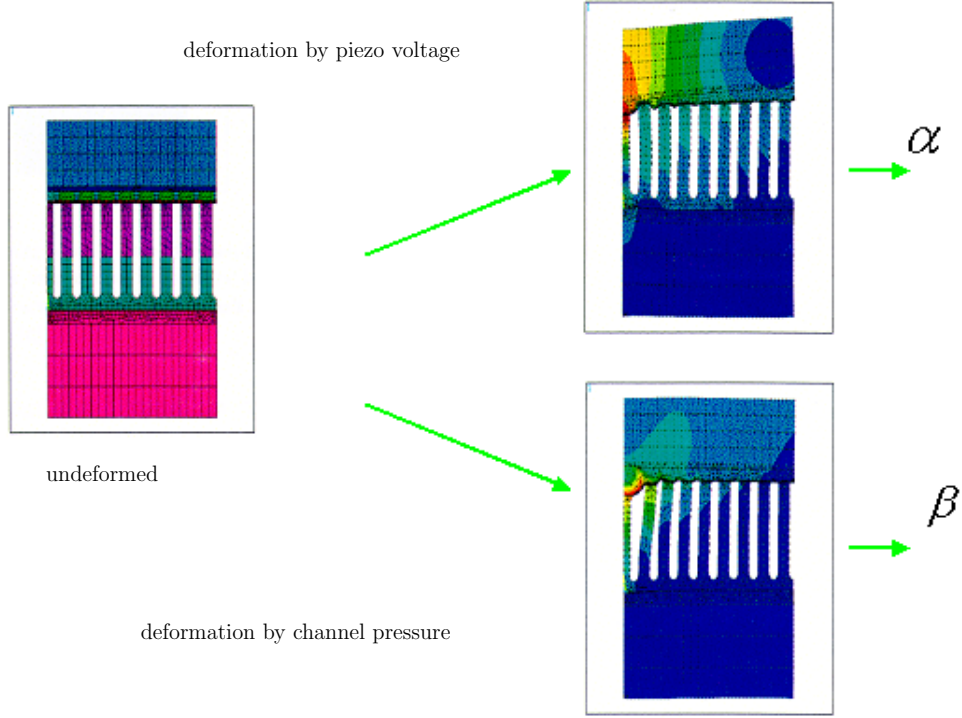


Figure A.1: *Structural deformation of the printhead calculated with ANSYS*

An example of structural deformation due to actuation and channel pressure is given in Fig. A.1 where a cross-section of an array of channels is depicted. From these deformations, the α and β parameters can be computed.

Substitution of (A.3) in (A.1) results in a set of equations which describe the pressure in a array of channels for the k^{th} element:

$$\frac{\partial^2}{\partial x^2} \underline{p} + \underbrace{\left(\frac{\omega^2}{B_k c_0^2} [I + \rho_0 c_0^2 [\beta]] \right)}_{bns} \underline{p} = - \underbrace{\frac{\rho_0 \omega^2 [\alpha] V}{B_k}}_{uns} \quad (\text{A.4})$$

For each element of each channel for different frequencies, the narrow-gap equation needs to be solved.

Solving the narrow-channel equation

The solution of the second order non-homogeneous differential equation (A.4) is given by the sum of the particular and the homogeneous solution, i.e. $\underline{p}(x) = \underline{p}_p(x) + \underline{p}_h(x)$.

Homogeneous solution

The homogeneous solution is the solution of the homogeneous second order DE:

$$\frac{\partial^2}{\partial x^2} \underline{p} + bsn \cdot \underline{p} = 0 \quad (\text{A.5})$$

First of all the solution is calculated for one channel, i.e.:

$$\frac{\partial^2}{\partial x^2} p + bsn \cdot p = 0 \quad (\text{A.6})$$

Assume a solution of the form $p(x) = e^{\lambda x}$. Substitution of this expression in (A.6) gives the characteristic equation:

$$\lambda^2 + bns = 0 \implies \lambda = \pm \sqrt{-bns} = \pm A \quad (\text{A.7})$$

The roots of the characteristic polynomial represents values of λ that satisfy the assumed form of $p(x)$. For n distinct solutions (the n solutions must be linearly independent), the homogeneous solution can be written as:

$$p_h(x) = \sum_{i=1}^n c_i e^{\lambda_i x} = c_1 e^{\sqrt{(-bns)} \cdot x} + c_2 e^{-\sqrt{(-bns)} \cdot x} \quad (\text{A.8})$$

In order to calculate the homogeneous solution for the multi-channel case, we make use of the fact that matrix bns is diagonalizable. A matrix is diagonalizable if the set of eigenvectors is linearly independent. If so, the following relations holds:

$$A = U \Lambda U^{-1} \implies e^{A \cdot t} = U e^{\Lambda \cdot x} U^{-1} \quad (\text{A.9})$$

with $A = \sqrt{-bns}$ and Λ denoting the eigenvalue diagonal matrix:

$$\Lambda = \begin{bmatrix} \lambda_1 & & 0 \\ & \lambda_2 & \\ & & \ddots \\ 0 & & & \lambda_n \end{bmatrix} \quad (\text{A.10})$$

with λ_i the i^{th} eigenvalue of $\sqrt{(-bns)}$ and U denoting the set of eigenvectors:

$$U = \begin{bmatrix} u_1 & u_2 & \dots & u_n \end{bmatrix} \quad (\text{A.11})$$

The individual solutions then becomes:

$$p_i = (e^{A \cdot x} U) \cdot \hat{e}_i = (U e^{\Lambda \cdot x}) \cdot \hat{e}_i = u_i e^{\lambda_i \cdot x} \quad (\text{A.12})$$

so the homogeneous solution is:

$$\underline{p_h}(x) = \sum_{i=1}^n c_i u_i e^{\lambda_i \cdot x} = U [P_L(x) \quad P_R(x)] \begin{bmatrix} \underline{c}_1 \\ \underline{c}_2 \end{bmatrix} \quad (\text{A.13})$$

with:

$$P_L(x) = \begin{bmatrix} e^{\lambda_1 x} & & 0 \\ & e^{\lambda_2 x} & \\ & & \ddots \\ 0 & & & e^{\lambda_i x} \end{bmatrix} \quad (\text{A.14})$$

$$P_R(x) = \begin{bmatrix} e^{-\lambda_1 x} & & & 0 \\ & e^{-\lambda_2 x} & & \\ & & \ddots & \\ 0 & & & e^{-\lambda_i x} \end{bmatrix} \quad (\text{A.15})$$

with $P_L(x)$ representing the positive pressure waves and $P_R(x)$ representing the negative pressure waves.

Particular solution

Finding a solution for:

$$\frac{\partial^2}{\partial x^2} p + bsn \cdot p = -uns \quad (\text{A.16})$$

gives the particular solution. One could suggest:

$$p_p = ap + b \quad (\text{A.17})$$

as particular solution. Substitution in (A.16) gives:

$$p_p = -\frac{uns}{bns} = -Buright \quad (\text{A.18})$$

The general solution becomes:

$$\underline{p}(x) = U[P_L(x) \quad P_R(x)] \begin{bmatrix} c_1 \\ c_2 \end{bmatrix} - Buright \quad (\text{A.19})$$

and its derivative:

$$\frac{\delta}{\delta x} \underline{p}(x) = U[\lambda_i P_L(x) \quad \lambda_i P_R(x)] \begin{bmatrix} c_1 \\ c_2 \end{bmatrix} \quad (\text{A.20})$$

The parameter x varies from zero to the segment length $x = L_i$. For the pressure of segment i for all channels at $x = 0$ and $x = L_i$ now can be written:

$$\begin{bmatrix} p(x=0) \\ p(x=L_i) \end{bmatrix} = \begin{bmatrix} U_i & 0 \\ 0 & U_i \end{bmatrix} \begin{bmatrix} P_{Li}(0) & P_{Ri}(0) \\ P_{Li}(L_i) & P_{Ri}(L_i) \end{bmatrix} \begin{bmatrix} c_{1i} \\ c_{2i} \end{bmatrix} - Burighth_i \quad (\text{A.21})$$

and its derivative:

$$\begin{bmatrix} \frac{\delta}{\delta x} p(x=0) \\ \frac{\delta}{\delta x} p(x=L_i) \end{bmatrix} = \begin{bmatrix} U_i & 0 \\ 0 & U_i \end{bmatrix} \begin{bmatrix} \lambda_i P_{Li}(0) & \lambda_i P_{Ri}(0) \\ \lambda_i P_{Li}(L_i) & \lambda_i P_{Ri}(L_i) \end{bmatrix} \begin{bmatrix} c_{1i} \\ c_{2i} \end{bmatrix} \quad (\text{A.22})$$

With these four equations and two known variables ($p(0)$ and $p(L_i)$ resulting from the boundary conditions), one can calculate the four unknown variables ($\frac{\delta}{\delta x} p(0)$, $\frac{\delta}{\delta x} p(L_i)$, c_1 and c_2).

The general solution is now known for all the segments for $x = 0$ and $x = L_i$. With use of (A.19) the pressure within the segments can be calculated. The way the boundary conditions are determined is explained in the next paragraph. The mean speed of the ink is calculated with:

$$\bar{v}(x) = \frac{1}{A_0} \frac{\delta}{\delta x} \int_{A_{0i}} H dA = \frac{jB_K}{\omega \rho_0} \frac{\delta p}{\delta x} \quad (\text{A.23})$$

with H the velocity distribution in the cross-section. By doing so, it is assumed that there is a linear pressure distribution inside the nozzle. Finally, the flow can be calculated with:

$$f_i(x) = A_{0i}\bar{v}(x) \quad (\text{A.24})$$

Combining the segments to one channel

In order to derive the boundary conditions for each individual segment, the segments are first of all combined to one channel. After all, for the begin and end of the channel the pressure equals zero and the boundary condition for each segment end, equals the boundary condition for the next segment. The coupling between the individual segments is defined by the following two equations:

$$p_i(L_i) = p_{i+1}(0) \quad (\text{A.25})$$

$$f_i(L_i) = f_{i+1}(0) \quad (\text{A.26})$$

Resuming one can say that in the Matlab model, the channel, the connection and the nozzle are taking into account. These parts are divided in several segments, which all have their own cross-section. The flexibility of the segment walls and the change in cross-section due to actuation or pressure may differ per segment. The narrow-gap equation (A.1) is solved for per segment, for each user-defined frequency.

In Fig. A.2, the magnitude of the frequency response from actuation voltage to pressure inside the channel is shown. In the figure, the first, second and the fourth resonance mode located at 62, 130 and 296 kHz are clearly visible. As explained in Chapter 3, the third resonance mode located at 214 kHz is barely excited as a result of the occurring destructive interference at 190 kHz. It can be seen that around this frequency no pressure built up in front of the nozzle ($x = L$) occurs.

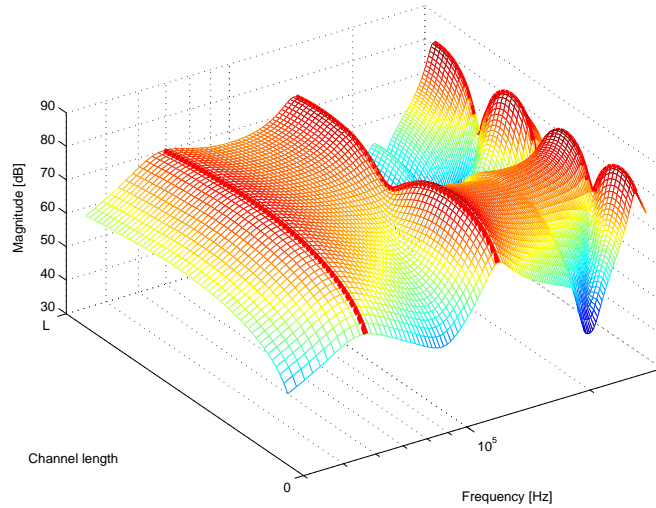


Figure A.2: *Surface plot of the theoretical pressure inside the ink channel as function of the longitudinal direction and frequency; $x = 0$ represents the channel-reservoir interface and $x = L$ the connection-nozzle interface.*

Appendix B

Dijksman Model

The Dijksman model [Dij84] is based on an energy balance and predicts whether a droplet is created and, if one is created, it provides an estimate of the ejected droplet speed and size. With the Dijksman model, several assumptions are made:

- Droplet formation is basically the transformation of kinetic energy into surface energy.
- Droplet formation starts as soon as the fluid in the nozzle passes the front of the nozzle.
- The influence of damping may be neglected during droplet formation.
- The curvature of the meniscus is not taken into account. Instead the mean position of the meniscus in time is used.
- The influence of the ambient air is neglected. It can be proven that drag is not relevant on the short distance the droplet has to travel.

Derivation

The fluid flow in the nozzle is assumed to be a pure viscous Poiseuille flow as a result of the pressure gradient over the nozzle. Consequently, the velocity $v(r, t)$ shows a parabolic distribution over the cross-sectional area with radius r . For such flow, the maximum velocity is reached at $r = 0$ and is twice the amount of the mean velocity:

$$v(t)|_{r=0} = 2\bar{v}(t) \quad (\text{B.1})$$

Suppose that the droplet formation process starts at time t_1 . At that instance, the mean velocity changes sign from negative to positive and has an outward direction. At this instant, a control volume is defined just in front of the meniscus, see Fig. B.1.

Subsequently, for $t > t_1$ a certain amount of kinetic energy will be transferred through the control surface. The volume of ink which is transported into the control volume equals:

$$V(t) = A_n \int_{t_1}^t \bar{v}_n dt \quad (\text{B.2})$$

with A_n denoting the cross-sectional area of the nozzle opening and $\bar{v}_n(t)$ the mean velocity. The amount of kinetic energy ($T = \frac{1}{2}mv^2$) transported through the control surface equals:

$$T(t) = \frac{1}{2}\rho_0 V(t) \int_{t_1}^t \bar{v}_n v_n|_{r=0} dt = \rho_0 A_n \int_{t_1}^t \bar{v}_n^3 dt \quad (\text{B.3})$$

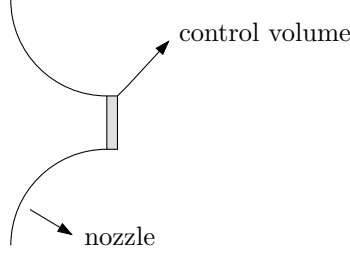


Figure B.1: *Schematic representation of the nozzle and the control volume.*

with ρ_0 the average density of the ink. (B.3) is an approximation and is based on the fact that a viscous fluid transports twice the amount of kinetic energy as a nonviscous fluid does, provided that the mean velocity in both cases is identical. This delivered kinetic energy is converted into surface energy, which is basically the drop formation process. The enlargement of the free surface can be computed provided that the shape of the fluid of the control volume is known. Therefore, it is assumed that the ink initially moves almost like a solid cylinder outside the nozzle opening and that the shape of the expanding control volume can be modeled as an expanding telescope, see Fig. B.2.

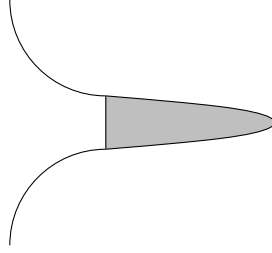


Figure B.2: *Enlargement of the free surface, modeled as an expanding telescope.*

The height of the free surface is defined by:

$$h(r, t) = \int_{t_1}^t v_n(r, t) dt \quad (\text{B.4})$$

The enlargement of the free surface can be found by evaluation of:

$$\vartheta(t) = 2\pi \int_0^{R_n} \sqrt{1 + \left(\frac{\delta h(r, t)}{\delta t} \right)^2} r dr - A_n \quad (\text{B.5})$$

with R_n the radius of the nozzle's end [Dij84]. The energy needed to enlarge the free surface is proportional to the surface tension σ of the ink and equals:

$$T_s(t) = \sigma \vartheta(t) \quad (\text{B.6})$$

The extra delivered kinetic energy is used to give a possible created droplet a certain velocity. The amount of kinetic energy inside the control volume equals:

$$T_{inst}(t) = \frac{1}{2} \rho_0 V(t) \bar{v}_n^2(t) \quad (\text{B.7})$$

and can be seen as the instantaneous amount of energy. As far as the exchange of energy is concerned, the condition for the formation of a droplet is reached as soon as this instantaneous energy inside the control volume is smaller than the delivered kinetic energy minus the energy needed to enlarge the free surface. The conditions for this time instant t_2 is given by (B.8) and determines when a droplet is created:

$$T(t_2) - T_s = T_{inst} \quad (\text{B.8})$$

with

- $T(t_2)$ the amount of supplied energy into the control volume, i.e. the outflowed kinetic energy
- T_s the energy needed to overcome the surface tension, i.e. the free surface energy
- T_{inst} the instantaneous energy inside the control volume, i.e. the kinetic energy inside the control volume.

An example of the different energies involved in the droplet formation is given in Fig. B.3. Here, the kinetic energy transported into in the control volume, the energy needed to enlarge the free surface, the net available energy and the instantaneous kinetic energy in the control volume are shown as function of time. At the time instant at which the net available energy ($T - T_{surface}$) equals the instantaneous kinetic energy, a droplet is formed. In Fig. B.4 the same variables are shown, but now for a non-jetting situation. No equilibrium point is reached whereas the supplied energy is too low to enforce a droplet. Such situation can occur when for example a actuation pulse is induced with a low amplitude.

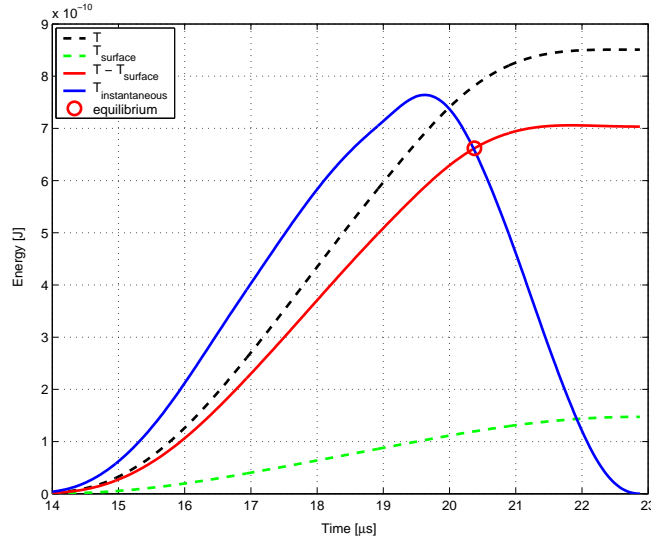


Figure B.3: *Energies involved in the droplet formation model of Dijkman resulting in a droplet.*

The volumes and surfaces on time instant t_2 determine the size and speed of the created droplet. At time instant t_2 the volume of the created droplet is known:

$$V_d = V(t_2) = A_n \int_{t_1}^{t_2} \bar{v}_n dt \quad (\text{B.9})$$

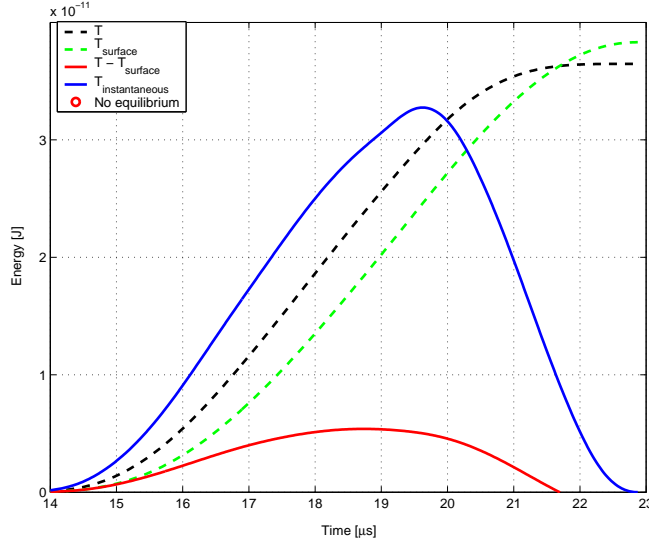


Figure B.4: *Energies involved in the droplet formation model of Dijkman not resulting in a droplet.*

In order to calculate the droplet speed, (B.8) is written as:

$$\rho_0 A_n \int_{t_1}^t \bar{v}_n^3 dt - \sigma \vartheta(t) = \frac{1}{2} \rho_0 V(t) \bar{v}_n^2(t) \quad (\text{B.10})$$

Reformulation of (B.10) yields:

$$\int_{t_1}^{t_2} [\bar{v}_n^2(t) - \bar{v}_n^2(t_2)] dt = \underbrace{\frac{2\sigma\vartheta(t_2)}{\rho_0 V(t_2)}}_{>0} \quad (\text{B.11})$$

The right-hand term of (B.11) is always positive, thus also the left-hand term must be positive. This implies that a droplet can only be formed if the velocity in the nozzle has gone through a maximum. In Fig. B.3, one can see that indeed a droplet is formed after the instantaneous kinetic energy, which is a function of the velocity, has gone through a maximum.

At time t_2 , the droplet under formation is still connected to the fluid in the nozzle by a stretching thread. For separation of the droplet, enlargement of the free surface is needed and for a Poiseuille flow it is assumed to be $\frac{1}{2}A_n$. In (B.8), the right-handed term represents the kinetic energy of the droplet which is still connected to the main fluid. So correction for the energy needed to form the extra free surface gives the kinetic energy of the resulting droplet:

$$T_d(t) = \frac{1}{2} \rho_0 V_d(t) \hat{v}_d^2 = \frac{1}{2} \rho_0 V(t_2) \bar{v}_n(t_2) v_n(t_2)|_{r=0} - \frac{\sigma A_n}{2} \quad (\text{B.12})$$

Now, the speed of the resulting droplet, \hat{v}_d , can be calculated with:

$$\hat{v}_d = \sqrt{\bar{v}_n(t_2) v_n(t_2)|_{r=0} - \frac{\sigma A_n}{\rho_0 V_d}} \quad (\text{B.13})$$

During the stretching of the tail of the droplet, the droplet is being slowed down by viscous dissipation. In [Dij84], a correction factor is defined to compensate for this effect and to eventually obtain the final droplet speed. This correction factor equals:

$$\Delta v_d = \frac{3\mu}{2\rho_0} \frac{1}{\int_{t_1}^{t_2} \bar{v}_n(t) dt} \quad (\text{B.14})$$

and the final droplet speed is given by:

$$v_d = \hat{v}_d - \Delta v_d = \sqrt{\bar{v}_n(t_2)v_n(t_2)|_{r=0} - \frac{\sigma A_n}{\rho_0 V_d}} - \frac{3\mu}{2\rho_0} \frac{1}{\int_{t_1}^{t_2} \bar{v}_n(t) dt} \quad (\text{B.15})$$

Appendix C

Wave Model

This appendix will shortly discuss the theory behind the wave model. For a more detailed description one is referred to [dZ05].

C.1 Channel Acoustics

Pressure waves in a flexibel channel filled with compressible fluid

In the first place, the deformation of the channel is calculated. On the one hand, piezo actuation results in a cross-sectional change of the channel. On the other hand, the pressure waves induced by the piezo actuation causing the flexibel channel to deform. The relation (α) between piezo actuation and channel deformation under the condition of $p = 0$ is calculated with use of the FEM package **ANSYS**. Besides, the relation (β) between channel pressure and channel deformation is also calculated with **ANSYS** under the condition of $V = 0$. Consequently:

$$\frac{\Delta A}{A} = \alpha V + \beta p \quad (\text{C.1})$$

with V denoting actuation voltage, p the channel pressure, A the cross-sectional area of the channel and α and β the calculated **ANSYS** parameters. Note that the same approach is used in appendix A.

With the derivation of the wave equation, Newton's second law is used. This is schematically shown in Fig. C.1.

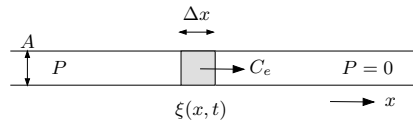


Figure C.1: *finite small volume element representing the wavefront*

The wavefront is represented as a finite small volume element with length Δx . The position of the fluid particles inside the volume element is given by the coordinate $\xi(x, t)$. The pressure

at the left hand side of the volume element is larger than the pressure at the right hand side and the wavefront is traveling with the effective speed of sound in ink C_e rightwards. The force acting on the volume element is given by pressure gradient in x-direction:

$$F = -A\Delta x \frac{\delta P}{\delta x} \quad (\text{C.2})$$

Consequently, the volume element will be compressed. Substituting C.2 in $F = m \frac{\delta^2 \xi}{\delta t^2}$ gives:

$$\frac{\delta^2 \xi}{\delta t^2} = -\frac{1}{\rho} \frac{\delta P}{\delta x} \quad (\text{C.3})$$

with using $m = A\Delta x \rho$ for the mass of the volume element. The relation between pressure P and compression $\frac{\delta \xi}{\delta x}$ of the volume element is given by the compression modulus K [Kro66]:

$$P = -K \frac{\delta \xi}{\delta x} \quad \Rightarrow \quad \frac{\delta P}{\delta x} = -K \frac{\delta^2 \xi}{\delta x^2} \quad (\text{C.4})$$

with C_e the speed of the traveling wave and $K = \rho C_i^2$. Then:

$$\frac{\delta^2 \xi}{\delta t^2} = \frac{K}{\rho} \frac{\delta^2 \xi}{\delta x^2} = C_i^2 \frac{\delta^2 \xi}{\delta x^2} \quad (\text{C.5})$$

resulting in a DE for a traveling wave with speed C_i .

Since the ink inside the channel is a compressible medium, pressure waves will induce an ink-flow inside the channel. With making use of Fig. C.2, it is explained how the velocity of the ink can be calculated. At $t = 0$ the position $\xi(0)$ of a fluid particle equals the position

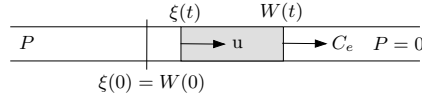


Figure C.2: *Compression of the ink.*

of the wavefront $W(0)$. The wavefront is traveling to the right with speed C_e . After time t , the wavefront has reached position $W(t)$. In case of an incompressible medium, the position of the fluid particle should still be $\xi(0)$. However, the fluid inside the area $W(t) - W(0)$ is compressed by pressure P according to:

$$\xi(t) - \xi(0) = \frac{\delta \xi}{\delta x} (W(t) - W(0)) \quad (\text{C.6})$$

and the fluid particle is transported from $\xi(0)$ to $\xi(t)$. The speed u of the ink transportation yields:

$$\frac{\delta W}{\delta t} = C_e \quad (\text{C.7})$$

$$\frac{\delta \xi}{\delta W} = -\frac{\delta \xi}{\delta x} = P/K \quad (\text{C.8})$$

$$u = \frac{\delta \xi}{\delta t} = \frac{\delta \xi}{\delta W} \frac{\delta W}{\delta t} = P/\rho/C_e \quad (\text{C.9})$$

So with a positive pressure, the ink flow travels in the same direction as the pressure wave. With a negative pressure, the ink will flow in opposite direction.

Reflection and Transmissions of Traveling Waves at a Cross-Sectional Area Change

A change in cross-sectional area of the channel will reflect a part of the incoming pressure wave and will transmit the other part.

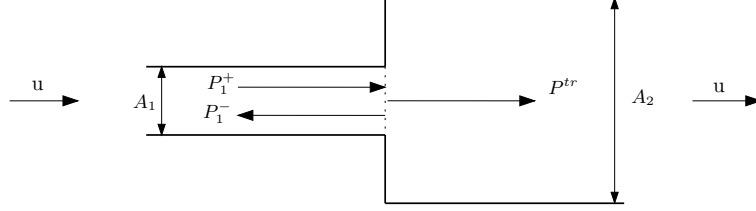


Figure C.3: *Reflection and Transmission at an area change.*

The volume velocity u at the left side of the interface must equal the volume velocity at the right side of the interface. Moreover, continuity of pressure leads to $P_1^+ + P_1^- = P^{tr}$ and $1+R = T$ with R and T denoting the transmission and reflection coefficient respectively. Using the characteristic impedance this leads to the reflection and transmission coefficient R and T :

$$R = \frac{A_1 - A_2}{A_1 + A_2} \quad (\text{C.10})$$

$$T = \frac{2A_1}{A_1 + A_2} \quad (\text{C.11})$$

Note that in the limit $A_2 \rightarrow 0$, the interface becomes a closed end and the incoming wave P_1^+ is completely reflected with the same sign and pressure doubling occurs ($R = 1$, $T = 2$). Conversely, for $A_2 \rightarrow \infty$, the condition of an open pipe is obtained ($R = -1$, $T = 0$).

Damping

The energy loss in a pressure wave as a result of the ink flow in the wave can be calculated with:

$$Q = \frac{\pi \cdot \Delta P \cdot r^4}{8 \cdot \eta \cdot \Delta L} \quad (\text{C.12})$$

which relates the volume flow Q and pressure drop ΔP for a cylindric channel with length ΔL assuming a Poiseuille flow. When the velocity of ink is known (and thus the volume flow), the resulting pressure drop ΔP can be calculated. With an additional tuning parameter is compensated for the fact that the real channel is square. It also compensates for the fact that due to the velocity variations in the channel, the velocity profile is better described by a Womersley profile instead of a Poiseuille profile. Since for a Womersley profile the fluid velocity near the channel wall is larger than for a Poiseuille profile, the channel resistance will be larger.

C.2 Fluid Dynamics in the Nozzle

First of all, it is assumed the ink inside the nozzle is incompressible. This is justified when the occurring phenomena are sufficiently low frequent. For a typical nozzle, the resonance

frequency is about 750 kHz. Since the dominating frequencies are significantly lower, the assumption is indeed justified.

Since the volume flux for the nozzle is constant, the velocity of the ink is dependent of the cross-sectional area:

$$u(t, x) = \frac{Q(t)}{A(t, x)} \quad (\text{C.13})$$

Subsequently, the relation between pressure drop over a nozzle segment Δx and the acceleration of the flow is calculated:

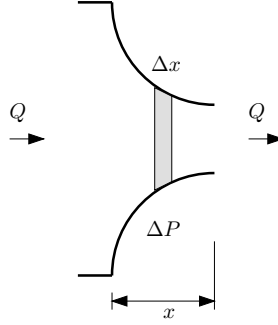


Figure C.4: Calculation of the flow in the nozzle.

$$\begin{aligned} F &= A(x) \cdot \Delta P = \rho \cdot \Delta x \cdot A(x) \cdot \frac{\delta u}{\delta t} = m \cdot a \\ \Delta P &= \rho \cdot \Delta x \cdot \frac{\delta u}{\delta t} = \frac{\rho \cdot \Delta x}{A(x)} \cdot \frac{\delta Q}{\delta t} \\ \Delta P &= \underbrace{\rho \cdot \int_0^{X(t)} \frac{dx}{A(x)}}_{M_Q(t)} \cdot \frac{\delta Q}{\delta t} \end{aligned} \quad (\text{C.14})$$

The pressure drop over the nozzle is calculated as follows. From the channel acoustics, the pressure in front of the nozzle is known (P_n). Besides, the pressure outside the nozzle equals zero. Additionally, the following effects are taken into account:

- According to Bernoulli a flow through a nozzle will experience resistance according to:

$$P_b(t) = \frac{\beta}{2} \cdot \rho \cdot Q(t)^2 \cdot [1/A(X(t))^2 - 1/(A(0))^2] \quad (\text{C.15})$$

- By a reversing nozzle flow, additional resistance occur due to vorticities:

$$P_w(t) = \frac{\xi}{2} \frac{Q(t)^2}{A(X(t))^2} \quad (\text{C.16})$$

for $Q(t) < 0$

- The pressure drop as a result of a viscous resistance is based on a Poiseuille flow:

$$P_v(t) = \gamma \cdot Q(t) \cdot 8\pi\eta \cdot \int_0^{X(t)} \frac{dx}{A(x)^2} \quad (\text{C.17})$$

The correction factor γ is used to compensate for the fact that the occurring flow is not a Poiseuille flow and is larger than 1.

- The pressure drop P_s as a result of the surface tension at the interface ink-air yields:

$$P_s(t) = \frac{4\sigma}{D_{nozzle}} \frac{y(t)}{\sqrt{1 + y(t)^2}} \quad (\text{C.18})$$

Then, the resulting pressure drop over the nozzle yields:

$$\Delta P = P_n - P_b + P_w - P_v - P_s \quad (\text{C.19})$$

According to (C.14), this pressure drop causes the ink mass in the nozzle to accelerate:

$$\frac{dQ(t)}{dt} = \frac{\Delta P}{M_Q(t)} \quad (\text{C.20})$$

Based on the calculated ink flow, the speed of the meniscus is calculated. Since the flux in the nozzle is constant, the meniscus velocity depends on the ink flow and on the cross-sectional area of the nozzle at the current meniscus position. It is assumed that the droplet formation starts when the meniscus moves outside the nozzle and stops when the ink flow changes sign. For calculation of the droplet properties, a modified Dijkman model is used. For more information about the droplet formation calculation, one is referred to [dZ05].

Appendix D

Destructive Interference

This appendix explains the phenomenon destructive interference. As shortly addressed in Section 3.2, the anti-resonances in the frequency response from piezo input to meniscus velocity (H_{P2MV} in Fig. 3.4) can be explained by this phenomenon. Destructive interference is a type of interference which occurs when two interfering waves have a displacement in opposite direction.¹ In the situation that the interfering waves have the same wavelength and amplitude, but in opposite direction, there is no resulting disturbance in the medium.

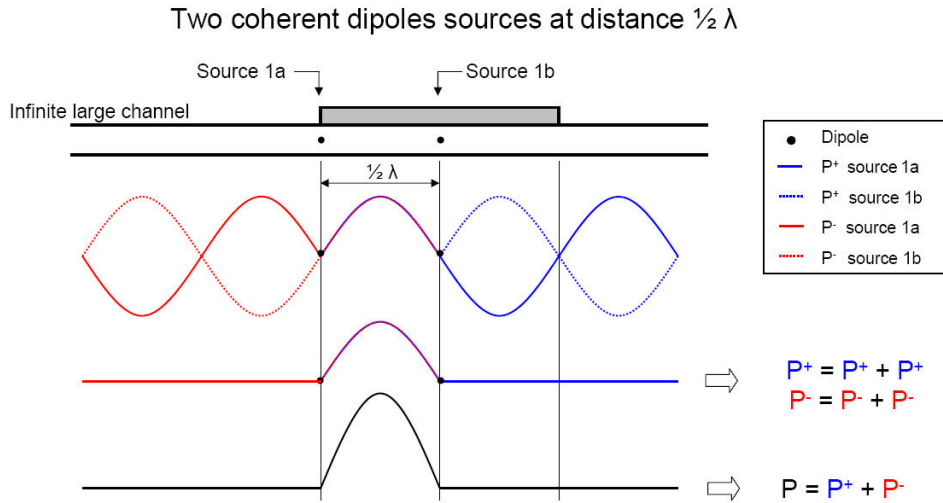


Figure D.1: *Generated pressure waves by two dipole sources.*

Under certain conditions, destructive interference can occur in the printhead channel during actuation. This is explained by means of Fig. D.1. In this figure, an infinitely large fluid line applied with a piezo actuator with length $L = \lambda$ is depicted. For now, the piezo actuator is replaced by two coherent dipole sources with a relative distance of $\frac{1}{2}\lambda$. Each dipole source oscillates with frequency f and generates pressure waves to both sides in longitudinal direction.

¹When two interfering waves have a displacement in the same direction, this type of interference is known as constructive interference.

Waves that propagate to the right are denoted with P^+ and waves that propagate to the left with P^- . In case the oscillation frequency of the dipole source generates pressure waves with wavelength λ ($f = \frac{c}{\lambda}$), the situation occurs as depicted in the figure. In the upper part of the plot, the generated pressure waves are depicted for an arbitrary time instant. The blue solid line presents the pressure waves caused by source 1a (P^+) and are traveling to the right. The same holds for the blue dashed line, but then generated by source 1b (P^+). In a similar way, the pressure waves traveling to the left are depicted in red (P^-). Since the two dipole sources are placed at a relative distance of $\frac{1}{2}\lambda$, the traveling waves (P^+) and (P^+) completely cancel each other out in the region where they overlap. Obviously, this also holds for the waves traveling to left and the compensated situation is plotted underneath. The resulting pressure in the channel yields $P = P^+ + P^-$ and is depicted in the lower part of the figure. Consequently, only pressure is present between the two sources and no energy is coupled into the channel.

When the piezo actuator is represented by for example 4 dipoles sources, the same situation occurs. This is depicted in Fig. D.2. Again, the relative distance between the two pairs of sources is $\frac{1}{2}\lambda$ and no pressure waves are transmitted into the channel.

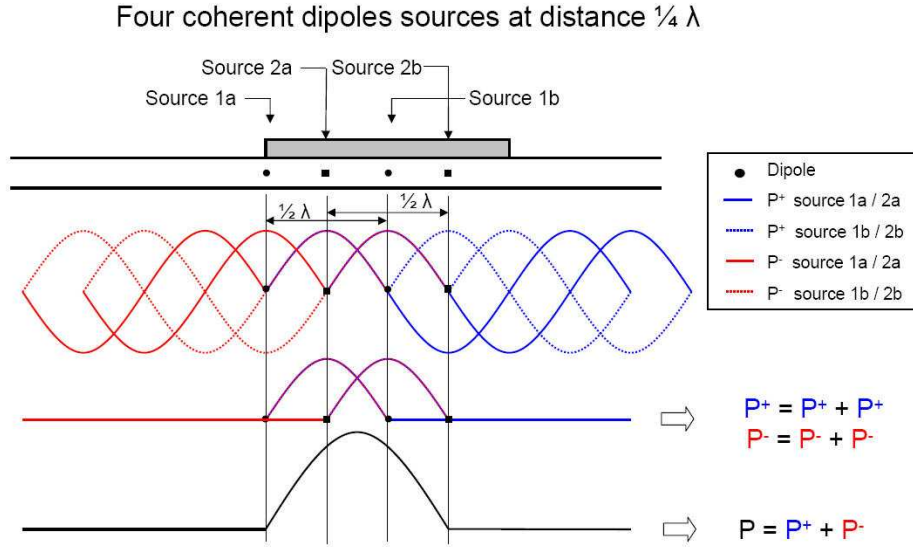


Figure D.2: *Generated pressures wave by four dipole sources.*

In case the piezo actuator is presented as a finite set of dipole sources, destructive interference occurs when the oscillation frequency of the dipole sources (and thus of the actuator) equals $f = \frac{c}{n\lambda} = n \frac{c}{L_{act}}$ with n denoting a positive integer.

Fig. D.3 shows a simulation performed with the Narrow-Gap model. The infinitely large channel as described above is modeled as a large square tube with in the mid-section a piezo actuator with length $L_{act} = 3.5$ mm. The actuation signal is chosen as a sinusoid with frequency $f = \frac{c}{L_{act}} = 286$ kHz using an effective speed of sound in ink of 1000 m/s. In the figure, the

resulting pressure inside the channel is depicted as function of time and place. Indeed, after some transient behavior, no pressure waves are transmitted into the not-actuated part of the channel. Under the piezo surface ($x = 3.5 \dots 7$ mm), the pressure varies with a frequency equal to the actuation frequency.

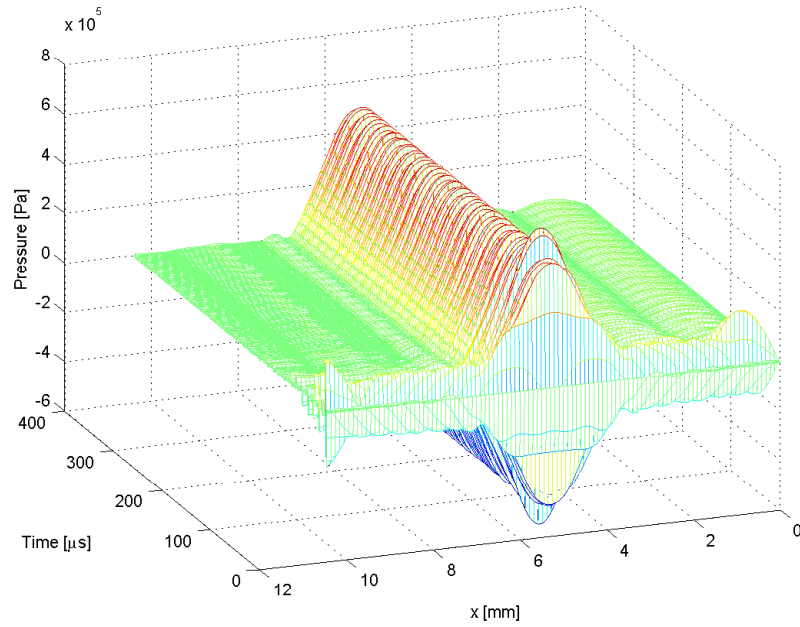


Figure D.3: *Calculated channel pressure as function of time and place showing the phenomena destructive interference.*

Appendix E

Simplification and Robustness of the ILC Actuation

In normal operation of the printhead, the separate ink channels are actuated by a trapezoidal pulse which is implemented on a so-called Application Specific Integrated Circuit (ASIC). The learned ILC actuation signals are, unfortunately, too complex to store on an ASIC. Only relative simple signals consisting of a very limited number of points can be implemented. For this reason, the ILC experiment as addressed in Section 5.4 is repeated, but now with using a modified ILC algorithm, see [WBSK06]. With the work presented in [WBSK06], ILC pulses can be designed with a predefined complexity. The experimental results are addressed in Section E.1. In Section E.2, the sensitivity of the simplified ILC actuation for production tolerance will be discussed.

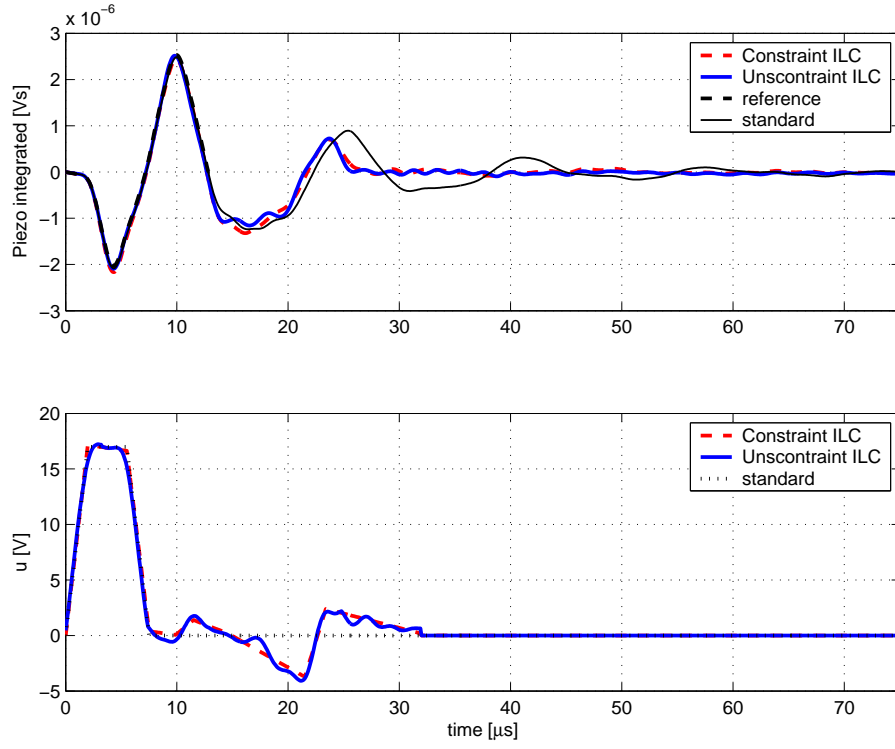
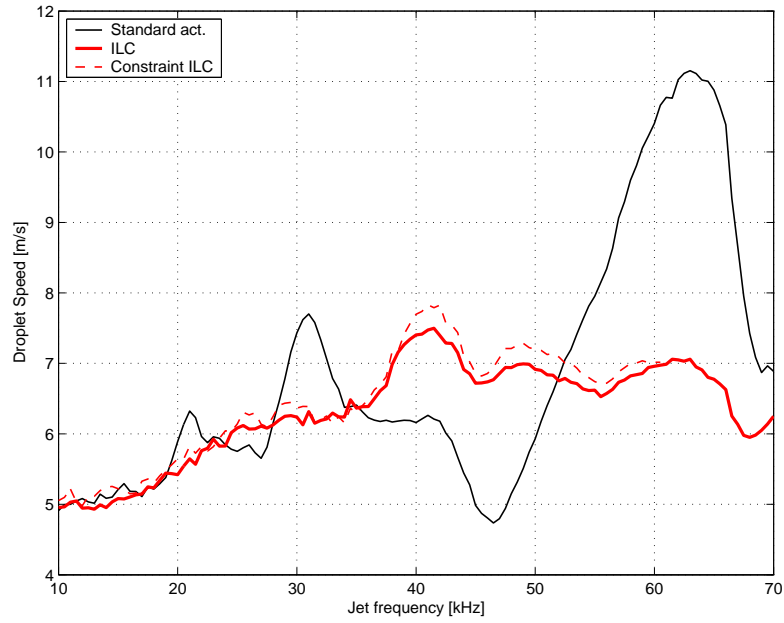
E.1 Constraint ILC

Exact the same experiment is performed as discussed in Section 5.4. The only difference is that now constraints are imposed on the actuation signal by means of constraint ILC. It is chosen to let the resulting ILC pulse consist of only 10 points. Note that a standard actuation already comprises 4 point. The experimental results are shown in Fig. E.1.

It can be seen that the learned constraint ILC pulse resembles the learned ILC pulse from Chapter 5. Moreover, despite the simplification of the actuation pulse, a comparable performance is obtained with respect to damping of the residual vibrations. This is confirmed in Fig. E.2, where the measured drop speed is depicted for both situations.

E.2 Robustness for Production Tolerances

This section will address the robustness of the learned simplified ILC pulse. All the ILC experiments discussed in this thesis are performed on the same channel. Due to production tolerances, the dynamics of different channels might differ. For this reason, it is interesting to investigate the sensitivity of the learned simplified ILC pulse for these production tolerances.

Figure E.1: *ILC experimental results for constraint and unconstraint ILC.*Figure E.2: *Measured DOD-speed for constraint ILC versus unconstraint ILC.*

This sensitivity issue will be investigated by measuring the drop speed as function of the jet frequency for the learned simplified actuation pulse. The concerning ILC pulse is learned

using channel 64. The drop speed measurements are performed for this channel and for channel 20, 40 and 60. The results are shown in Fig. E.2.

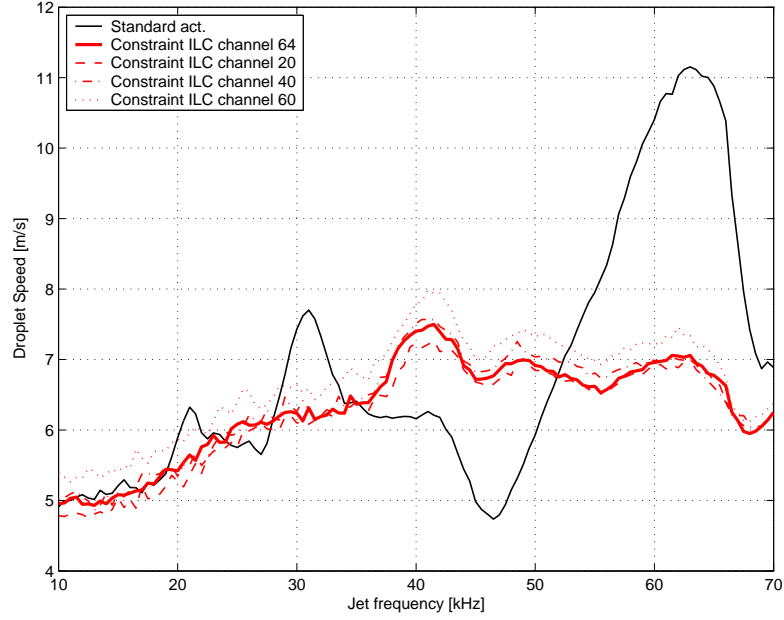


Figure E.3: *Measured DOD-speed for constraint ILC for different channels.*

Based from this figure it can be concluded that the ILC actuation is robustly designed in order to suppress residual vibrations for different channels, despite the presence of production tolerance and the fact that the actuation is simplified.

Bibliography

- [Bel97] W. Beltman, *Forces on a rigid plate oscillating normal to a fixed surface*, Journal of Sound and Vibration 206, pp 217-241, 1997.
- [Bos03] O.H. Bosgra, *Lifted iterative learning control*, Eindhoven University of Technology, 4K140 Capita Selecta in Control, 2003.
- [Dij84] J. Dijkman, *Hydrodynamics of small tubular pumps*, Journal of Fluid Mechanics, vol. 139, pp 173-191, 1984.
- [Dij03] B. Dijkstra, *Iterative learning control, with application to a waferstage*, PhD Thesis. Delft University of Technology, The Netherlands, 2003.
- [dZ05] W. de Zeeuw, *Akoestisch inkjet model met refill*, R&D Research Report, Océ Technologies B.V., 2005.
- [Kro66] R. Kronig, *Leerboek der natuurkunde*, Scheltema & Holtema NV Amsterdam, pp 207, 1966.
- [Lei94] T.G. Leighton, *The acoustic bubble*, Academic press ISBN 0-12-441920-8, 1994.
- [Lon00] R.W. Longman, *Iterative learning control and repetitive control for engineering practice*, International Journal of Control 73, pp 930-954, 2000.
- [Moo99] K.L. Moore, *Iterative learning control; an expository overview*, Applied and Computational Controls, Signal Processing and Circuits, pp 151-214, 1999.
- [Nag06] P.M. Nagelmaeker, *MIMO iterative learning control on an inkjet printhead*, Literature Study, 2006.
- [Pat] European Patent, 1 378 360 A1.
- [RDS04] I. Rotariu, B. Dijkstra, and M. Steinbuch, *Comparison of standard and lifted ILC on a motion system*, 3rd IFAC Symposium on Mechatronic Systems, Sydney, 2004.
- [Spr01] R. Sprague, *Acoustic ink printing*, International Conference on Digital Printing Technologies NIP, pp 660-663, 2001.
- [TAP97] J.C. Tannehill, D.A. Anderson, and R.H. Pletcher, *Computational fluid mechanics and heat transfer*, Taylor francis (UK), ISBN 156032046X, 1997.

- [TvdMB01] R. Tousain, E. van der Mech  , and O.H. Bosgra, *Design strategies for iterative learning control based on optimal control*, Proc. 40th IEEE Conf. on Decision and Control, pp 4463-4468, Orlanda, 2001.
- [vdWB06] J. van de Wijdeven and O.H. Bosgra, *Residual vibration suppression using hankel iterative learning control*, Proceedings of the American Control Conference, Minneapolis, USA, 2006.
- [WBBK05] M.B. Groot Wassink, N. Bosch, O.H. Bosgra, and S.H. Koekebakker, *Enabling higher jet frequencies for an inkjet printhead using iterative learning control*, Proc. IEEE Conf. on Contr. Applications, pp 791-796, Toronto, Canada, 2005.
- [WBK06] M.B. Groot Wassink, O.H. Bosgra, and S.H. Koekebakker, *Minimization cross-talk for an inkjet printhead using MIMO ILC*, American Control Conference, pp 964-969, Minneapolis, USA, 2006.
- [WBSK06] M.B. Groot Wassink, O.H. Bosgra, M. Slot, and S.H. Koekebakker, *Minimizing residual vibrations and cross-talk for inkjet printheads using ilc designed simplified actuation pulses*, IS&T NIP 22, Denver, US, 2006.
- [WZBK06] M.B. Groot Wassink, F. Zollner, O.H. Bosgra, and S.H. Koekebakker, *Improving the drop-consistency of an inkjet printhead using meniscus-based iterative learning control*, Conference on Control Applications, Munich, Germany, 2006.
- [Zol05] F. Zollner, *Iterative learning control of an inkjet printhead*, MSc Thesis, Delft University of Technology, The Netherlands, 2005.